Metal-organic frameworks for gas- and vapour-sensing applications

Von der Naturwissenschaftlichen Fakultät der

Gottfried Wilhelm Leibniz Universität Hannover

zur Erlangung des Grades

Doktorin der Naturwissenschaften

(Dr. rer. nat.)

genehmigte Dissertation

von

Ina Carina Strauß, M. Sc.

2020

Referent: Prof. Dr. Jürgen Caro

Korreferent: Prof. Dr. Natalija Guschanski

Weiterer Korreferent: Prof. Dr. Leonid M. Kustov

Tag der Promotion: 16.06.2020

Acknowledgements

Kurzzusammenfassung

Die Verwendung von Materialien mit gezielt einstellbaren Eigenschaften ist eine elegante und ressourcenschonende Lösung, um bestmögliche Ergebnisse für spezifische Anwendungen in unterschiedlichsten akademischen sowie industriellen Bereichen zu erzielen. Hierbei könnten metallorganische Gerüstverbindungen (engl: Metal-organic frameworks, MOFs), aufgrund ihres modularen Aufbaus auf Molekülebene und der Möglichkeit postsynthetischer Modifikationen, einen lang ersehnten Hoffnungsschimmer darstellen. Individuell anpassbare Eigenschaften, wie hohe Oberflächen oder kontrollierbare Porengrößen, sind ein Grund dafür, warum MOFs Anwendungen in unterschiedlichsten Bereichen, unter anderem der Katalyse, Gasspeicherung und Sensorik, finden können.

Die Dissertation behandelt den potentiellen Einsatz von MOF-basierten Materialien als chemische Sensoreinheiten. Es wurden zwei unterschiedliche MOFs und ein MOF-basierendes Wirt-Gast-Verbundmaterial hergestellt, charakterisiert und auf ihr jeweiliges Potential hinsichtlich der Adsorption industriell relevanter Gase untersucht. Hierbei lag der Fokus nicht nur darin, unterschiedliche experimentelle Ansätze zur Detektion der Gasspezies zu prüfen, sondern auch auf der Vereinfachung des Messaufbaus im Hinblick auf die Herstellung eines potentiellen, kommerziellen Sensors.

Der erste Teil dieser Arbeit befasst sich mit dem Kobalt-basierten MOF-74. Zuerst wurde die adsorptive Interaktion zwischen Co-MOF-74 mit unterschiedlichen Gas- und Dampfmolekülen wie Kohlendioxid, Propan, Propen, Argon, Methanol und Wasser mithilfe spektroskopischer Methoden untersucht. Außerdem konnte das anisotrope optische Absorptionsverhalten des Materials durch Polarisationsmikroskopie nachgewiesen werden. Anschließend wurde ein Co-MOF-74 basiertes Wirt-Gast Verbundmaterial konzipiert und synthetisiert. Hierzu wurde das organische Halbleitermolekül Tetrathiafulvalen postsynthetisch in die MOF-74 Kanäle infiltriert. Dies führte zu einer Erhöhung der elektrischen Leitfähigkeit des Materials. Elektrische Leitfähigkeitsmessungen zeigten, dass Co-MOF-74-TTF eine durch Gasmoleküle induzierte Widerstandsänderung aufweist und somit als möglicher Sensor eingesetzt werden kann.

Im zweiten Teil der Dissertation wird die Gasadsorption des Zr-MOFs UiO-66 sowie dessen Amino-funktionalisierten Pendants UiO-66-NH$_2$ untersucht. FTIR Spektroskopie zeigte, dass UiO-66 und UiO-66-NH$_2$ entsprechend ihrer Azidität und Basizität unterschiedlich mit Kohlenmonoxid, Stickstoff und Acetonitril wechselwirken. Sowohl die Sensitivität gegenüber geringen Kohlendioxidkonzentrationen (Kontrolle der Raumluftqualität), als auch die Sensitivität gegenüber höheren Kohlendioxid-Konzentrationen (in Bereichen der Lebensmittelverpackungsindustrie), konnte mithilfe von Kapazitätsmessungen und FTIR Messungen gezeigt werden.

Diese Dissertation beinhaltet vier Artikel, welche in national und international renommierten chemischen Journalen publiziert wurden, und innerhalb dieser Arbeit in logischer Reihenfolge, unterteilt in zwei Hauptkapitel, vorgestellt werden.

<u>Keywords:</u> Metallorganische Gerüstverbindungen, Gassensoren, MOF-Gast-Interaktionen, Infiltrierung von MOFs, leitfähige MOFs, Gasadsorption

Abstract

In order to achieve optimal results for various specific applications, intentionally tailored materials with adjustable properties are a smart and sustainable solution for many research challenges. Here, metal-organic frameworks (MOFs) might be a glimmer of hope reasoned in their modular design at a molecular level and the possibility of post-synthetic modifications, which leads to a large number of materials with tailorable structural characteristics such as high surface areas and controllable pore sizes. These properties make them to promising materials in various research fields like catalysis, gas storage and sensing.

This thesis discusses the potential deployment of MOFs into chemical sensing devices. Two different MOFs and one MOF-based host-guest composite were synthesized, characterized and tested upon their capability to adsorb various gases. Various experimental approaches were followed to detect and differentiate between the gas- and vapour-species and to identify the most feasible one for the incorporation into a possible sensor.

The first part of this thesis is focused on cobalt-based MOF-74. Initially, the adsorptive interaction of Co-MOF-74 with different gas and vapour molecules, such as carbon dioxide, propene, propane, argon, methanol and water has been evaluated by diverse spectroscopic techniques.

In addition to that, spectral measurements emphasize the anisotropic optical adsorption behaviour of the material when illuminated with polarized light. Afterwards a Co-MOF-74-based host-guest composite was designed and synthesized. The organic semiconductor tetrathiafulvalene was post-synthetically infiltrated into the channels of MOF-74, leading to an increased electrical conductivity of the compound compared to the non-infiltrated MOF. The following electrical measurements under various gas- and vapour-atmospheres showed a modification of resistivity when these guest molecules are adsorbed into the composite and therefore proved, that Co-MOF-74-TTF is a suitable candidate for gas sensing devices.

Within the second part of this thesis, the performance of the zirconium-based UiO-66 framework and the amino-functionalized equivalent UiO-66-NH$_2$ regarding their gas adsorption capability was evaluated. FTIR spectroscopy showed, that according to their acid and basic properties, UiO-66 and UiO-66-NH$_2$ interact differently with carbon monoxide, nitrogen and acetonitrile. The sensing capability towards low carbon dioxide concentrations, which could be applied for controlling indoor air concentrations and the capability towards high carbon dioxide concentrations, important for industrial applications, such as food packaging, were proven by capacity and FTIR measurements.

This thesis includes four articles published in national and international renowned chemical journals, which are presented in a logical order, divided into two main chapters.

Keywords: Metal-Organic Frameworks, Gas sensors, MOF-guest-interaction, Infiltration of MOFs, Conductive MOFs, Gas adsorption

Table of contents

List of abbreviations

1-MCP	1-Methylcyclopropene
Atz	3-Amino-1,2,4-triazole
BDC	Benzene-1,4-dicarboxylic acid
BHT	Benzenehexathiol
BPDC	Biphenyl-4,4´-dicarboxylic ac
BPy	4,4'-Bipyridine
BTB	4,4′,4″-Benzene-1,3,5-triyl-tribenzoate
BTC	Benzene-tricarboxylate
Cp	η^5-Cyclopentadienyl
DABCO	1,4-diazabicyclo[2.2.2]octane
DOBDC	2,5-Dioxido-1,4-benzenedicarboxylate
DSBDC	2,5-Disufidobenzene-1,4-dicarbocylate
HKUST	Hong Kong University of Science and Technology
HITP	2,3,6,7,10,11-Hexaminotriphenylene
HMDA	Hexametylene-1,6-diamine
HTTP	2,3,6,7,10,11-Hexathiotriphenylene
MIL	Materials Institute Lavoisier
MMM	Mixed matrix membrane
MOF	Metal-organic framework
NDC	2,6-Napthalenedicarboxylic acid
PCA	4-Pyridinecarboxylic acid
PCN	Porous coordination network
PDT	2,3-pyrazinedithiolate
PSM	Post-synthetic modification
PVP	Polyvinylpyrrolidone
QCMB	Quartz crystal microbalance
SBU	Secondary building unit
TATB	4,4′,4″-s-Triazine-2,4,6-triyl-tribenzoic acid
TCNQ	Tetracyaoquinodimethane
TPDC	p-Terphenyl-4,4''-dicarboxylic acid
tBuONO	Tert-butyl nitrite
TFBDC	Tetrafluorobenzene-1,4-dicarbocylate
TMBDC	Tetramethylterephthalate
TMS	Tetramethylsilane
TTF	Tetrathiafulvalene

1 Motivation

In 2019 9742 articles featured the term metal-organic frameworks (MOFs) in their topics. When looking back at the tendencies of the last decades (see Figure 1), one can assume, that in the following years the number of articles dealing with MOFs will rise even further. Since Yaghi published the structure of the archetypical porous framework known as MOF-5[1] in 1999, MOFs have become the most investigated and discussed class of crystalline materials, covering topics from fundamental research to industrial and commercial applications. The increasing interest in this material class is based on their modular construction, which enables nearly limitless possible combinations within the synthesis route, resulting in highly versatile materials.
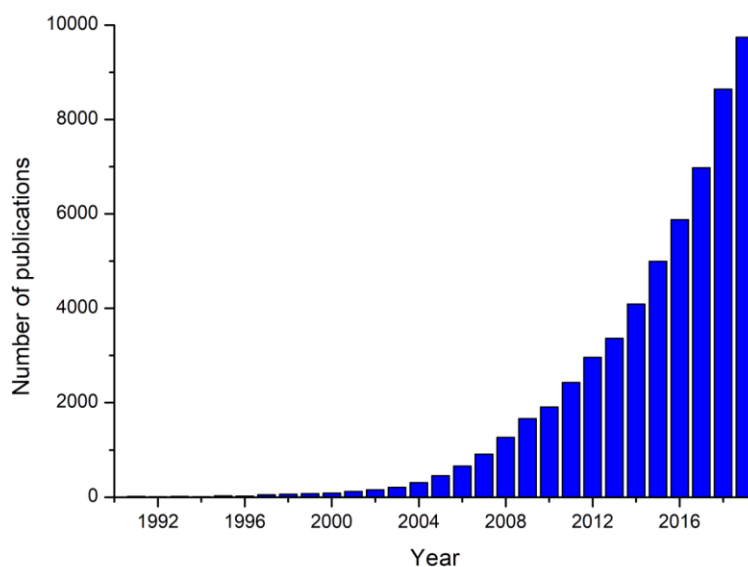
Figure 1. Number of publications including "metal organic framework" in their topics (Source: ISI Web of Science, retrieved 10.01.2020)

Constructed of metal ions or metal clusters, which are coordinated to organic linker molecules, two or three dimensional frameworks can be build up. These often highly flexible and highly porous structures can be modified on an atomic level, allowing the adjustment of properties such as pore dimensions and shape as well as the introduction of functionalities, just to mention a few. The properties of MOFs can be created via pre-synthetic design methods such as choosing suitable metal ions/clusters and organic linkers containing one or several functionalities as well as via post-synthetic modification methods.[2] These various possibilities to tailor the

properties of the framework, are the secrets behind their superiority compared to other porous materials (e.g. zeolites, active carbon, mesoporous materials)[3], with regard to the utilization for heterogeneous catalysis, energy storage, gas separation, sensing and biological applications.[4–7] Many classes of materials, which are implemented into these fields possess limited customization abilities resulting in a restricted use for specific applications. Even though MOFs suffer of relatively low thermal and chemical stabilities, their unique properties make them suitable materials for the aforesaid operational areas, when their major drawbacks can be overcome.

This work focuses on the deployment of MOFs in gas sensing applications. New and innovative chemical sensors are, among other things, needed for environment and safety control systems, devices including smart network connected medical devices or industrial process monitoring systems.[8,9] Therefore, within this work two MOF types , MOF-74 and UiO-66, are examined for their possible integration into sensing applications. The interaction of several gases, such as carbon dioxide, propene, propane and argon, as well as the interaction of several vapours such as methanol and water, with the cobalt-based MOF-74 was studied. In addition to that, the conductivity of Co-MOF-74 was enhanced by introducing tetrathiafulvalene into its one dimensional pores. The conductivity of this new composite changes according to the surrounding atmosphere, which predestines Co-MOF-74 as a suitable material to be incorporated into gas sensing devices. Concerning the use of UiO-66 type MOFs for those, the detectability concerning various carbon dioxide concentrations was verified. Furthermore, the acidic and basic properties of UiO-66 type MOFs were studied by applying carbon monoxide, nitrogen and acetonitrile.

2 Coordination chemistry: From 0D to 3D

Metal-organic Frameworks (MOFs) are hybrid inorganic-organic materials and can be considered as a subclass of coordination networks.[10] Therefore, MOFs eventually emerged from coordination chemistry, which beginnings date back to 1706 when the first coordination compound was reported. The pigment "Prussian blue" $Fe^{3+}_4[Fe^{2+}(CN)_6]_3 \cdot H_2O$ (Figure 2) was serendipitously synthesized by Johann J. Diesbach.[11,12] More than two centuries later, in 1913, the chemist Alfred Werner was awarded for the Nobel Prize in chemistry based on his work on the octahedral configuration of the transition metal complex $[Co(NH_3)_6]Cl_3$ (Figure 2), which is considered to be the basis of modern coordination chemistry.[13,14] Various publications by chemists, inspired by Werner's work, substantiated that coordination chemistry was no longer limited to a molecular (0D) level. Hofmann et al. published his findings of a 2D crystalline material with the general formula $[Ni(NH_3)Ni(CN)_2](C_6H_6)$ in 1897, known as Hofmann clathrate (Figure 2).[15]

Prussian blue

Werner complex

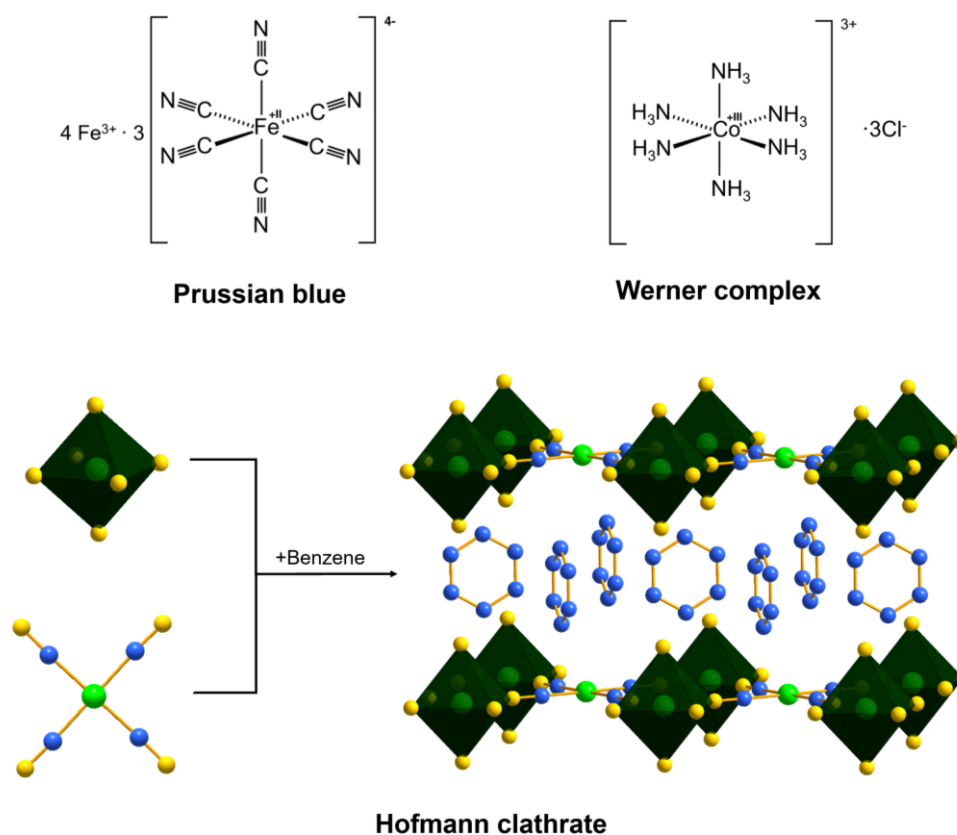+Benzene

Hofmann clathrate

Figure 2. Structures of the pigment Prussian blue and Werner complex (upper left and right). The lower image shows the structure of the Hofmann clathrate, consisting of alternating octahedral and square planar Ni^{2+} ions (green) linked by CN^- ions (C: blue, N: yellow). In between these layers, benzene molecules are situated.

In 1952 Powell and coworkers were able to solve its crystal structure via single crystal X-ray diffraction.[16] The original Hofmann clathrate consists of 2D layers of alternating octahedral and square planar Ni^{2+} ions, which are linked by CN^- ions.[16] When Iwamoto and coworkers replaced the terminal ammonia ligands with an bifunctional amino-linker called hexametylene-1,6-diamine (HMDA) they were able to link the adjacent layers together, resulting in a 3D network structure.[17] Since Iwamoto et al. were able to demonstrate the influence of the incorporation of organic linkers into Hofmann clathrates on their properties, the next logical step was, to link only metal ions through organic linker molecules.[2] This approach resulted in what is nowadays known as coordination networks. While the first coordination networks were published by Saito et al.[18–20] in 1959, it took 30 more years until Hoskins and Robson[21] outlined the potential of constructed porous coordination polymers in 1989. In 1995 the term "metal-organic framework" was first used by Yaghi et al.[22] for the porous structure of $Co(BTC)(Py)_2$ (BTC = benzene-tricarboxylate, Py = pyridine). This MOF consists of Co-BTC layers separated by pyridine molecules, which are also coordinated to the metal centers.[2,22] The Co-BTC layers are built up of Co^{3+} ions, which are linked to three carboxylate groups of different BTC molecules.[2,22] One of the BTC molecules is coordinated to the metal centers in a bidentate fashion and the others are coordinated in a monodentade fashion.[2,22] The two major advantages in the use of charged linkers, as in the described example, are the increased bond strength and the resulting higher thermal and chemical stability, as well as the fact that charged linkers are able to compensate the charge of the metal centers, enabling the existence of ionic networks.[2]
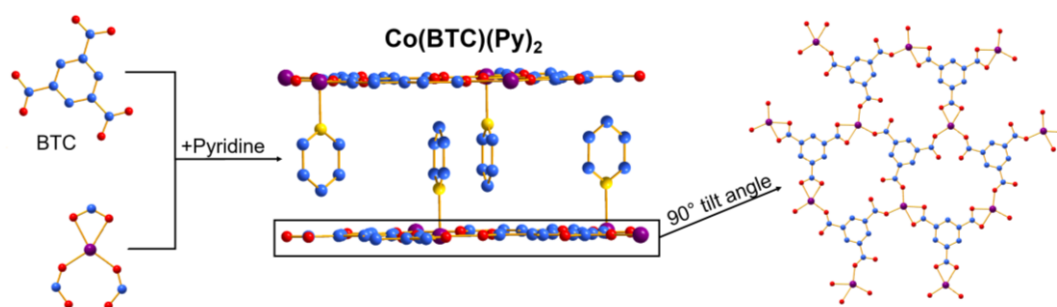
Figure 3. Structure of Co(BTC)(Py)₂ consisting of Co-BTC layers separated by pyridine molecules, which are coordinated to the Co³⁺ centers. (Co: purple, C: blue, N: yellow, O: red)

In the following years, a number of publications regarding porous frameworks were released, as for example, in 1997 Kitagawa et al.[23] reported a three-dimensional framework with the capability to reversibly adsorb CH_4, N_2 and O_2. In 1999, when Yaghi[1] recorded his findings of a porous network called MOF-5, its surface area of

2900 m^2g^{-1} surpassed even the ones of zeolites (note that in later contributions, the surface area of MOF-5 is determined even higher, with a value of 3800 m^2g^{-1})[24]. From there on, the interest in MOFs exponentially increased.[25] Nowadays, the Cambridge Crystallographic Data Centre possesses 84185 MOF structures, and thousands of new structures are published each year.[26]

3 The chemistry of MOFs

3.1 Building units

The chemistry of linking molecules or clusters to obtain ordered structures such as MOFs is referred to as reticular chemistry.[27,28] Within the reticular chemistry of MOFs, inorganic and organic units are connected via strong bonds, such as coordinative bonds.[27,28] The designation secondary building units (SBUs) was originally used for the structural chemistry of zeolites, describing complex structures by simplifying an arrangement of molecules into one building unit.[29] Within the field of MOFs, SBUs describe the inorganic building units consisting of metal clusters or discrete coordinated metal ions. These are linked via organic molecules with at least two groups, which can connect at least two SBUs together, resulting in one-, two- or three-dimensional frameworks. In order to explain the general buildup, Figure 4 shows the organic linkers, the SBUs and the resulting crystal structures of the two exemplary frameworks MOF-5 and HKUST-1 (HKUST = Hong Kong University of Science and Technology).

The SBU of MOF-5 consists of a central oxygen atom which is coordinated to four zinc atoms, resulting in a Zn-tetrahedron. This is then capped by 6 carboxylate groups (from linker) forming a cluster of $Zn_4(O)(CO_2)_6$.[1] This tetranuclear octahedrons are linked via linear, ditopic benzene-1,4-dicarboxylic acid (BDC) molecules, leading to a three-dimensional framework structure with a primitive cubic topology (pcu).[2] MOF-5 possesses two different, alternating and interconnected pores with diameters of 15.1 Å and 11.0 Å.[2] The second exemplary MOF, HKUST-1, is build up from a four-connected SBU: A dinuclear $Cu_2(CO_2)_4$ paddlewheel, where the copper atoms are each coordinated by four oxygen atoms of the carboxylate groups of different linker molecules. In the presence of water, one additional oxygen is bound to the paddlewheel, forming a square pyramid.[30] It should be noted that the water molecules are bound axially to the copper-paddlewheel and thermal activation of HKUST-1 results in highly active open metal sites.[30] The 4-connected SBU is bridged by tritopic benzenetricarboxylate (BTC) linkers forming a 3,4-connected cubic network (tbo topology)[31] with three different pores, possessing diameters of 5 Å, 11 Å and 13.4 Å.[32]
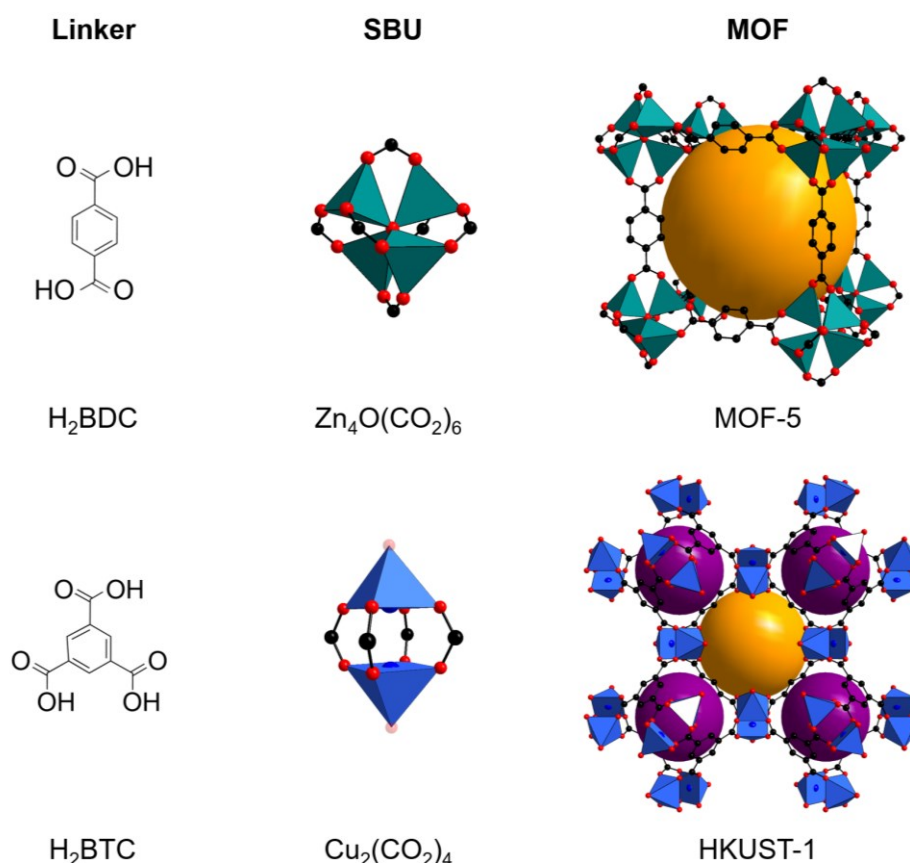
Figure 4: Schematic representation of Linker, SBU and structure of MOF-5 and HKUST-1. MOF-5 consists of BDC linkers which bridge the $Zn_4O(CO_2)_6$ metal nodes. HKUST-1 is build up of $Cu_2(CO_2)_4$. In the presence of water, one additional oxygen interacts with the copper, resulting in a square pyramid. The additional oxygen of this water molecule within the HKUST-1 metal-node is depicted in a transparent way. The cavities of both MOFs are indicated by orange and purple spheres. (Zn, green, Cu:blue, C: black, O: red)

3.2 Isoreticular MOFs

While completely different MOFs can be obtained by changing the linker connectivity or by retaining the same linker and simply changing the geometry of the SBU, a series of isoreticular MOFs (IRMOFs) can be characterized by the same topology, when the organic linker is elongated or functionalized.[33,34] The advantage of having a series of MOFs with the same topology but different linkers lies in the easy tailorability of the specific properties.[34,35] The most prominent example for an isoreticular MOF series is based on the previously presented MOF-5. Yaghi and coworkers presented a series of 16 highly crystalline IRMOFs based on MOF-5 but with different functional groups (-Br, -NH_2, -OC_3H_7, -OC_5H_{11}, -C_2H_4, -C_4H_4) or organic linkers with different length (biphenyl, tetrahydropyrene, pyrene, terphenyl).[34] Figure 5 shows IRMOF-1 (also known as MOF-5) and IRMOF-16, as well as a selection of the incorporated organic linkers. Within this series, the pore diameters can be varied from 3.8 Å (IRMOF-5) up

to 19.1 Å (IRMOF-16).[34] A closer look to the individual properties of the MOFs outlines the influence of the inserted linkers: While IRMOF-6 exhibits a high methane storage capacity (based on its high surface area, high pore volume and advantageous designed pore aperture), IRMOF-8, -10, -12, -14, -15 and -16 possess the lowest reported densities of a crystalline material known up until the publication of this IRMOF series.[34]
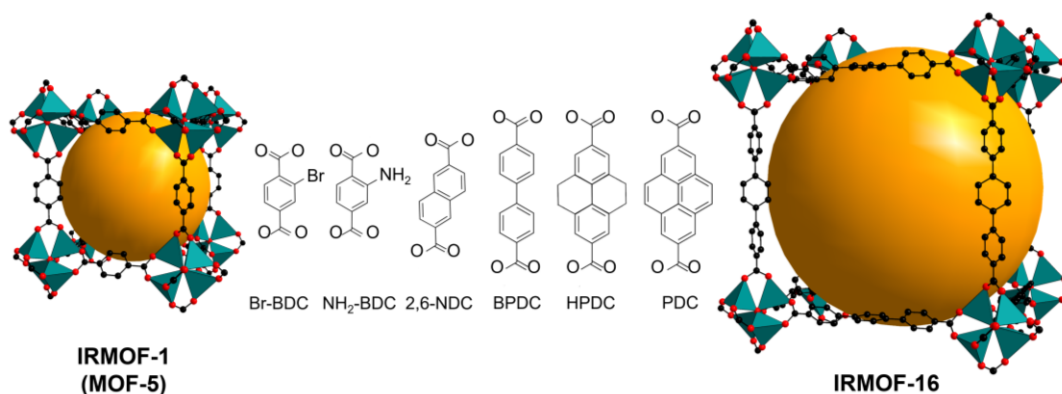
Figure 5. Isoreticular series of MOF-5 analogues and the associated linker molecules of IRMOF-1 (BDC) IRMOF-2 (Br-BDC), IRMOF-3 (NH₂-BDC), IRMOF-8 (2,6-NDC), IRMOF-14 (BPDC), IRMOF-12 (HPDC), IRMOF-10 (PDC), IRMOF-16 (TPDC). The cavities of IRMOF-1 and 16 are indicated via orange spheres.

The concept of isoreticular design was not only applied to MOF-5, but also to several other MOFs possessing isoreticular structures such as UiO-66, MOF-74 and the aforementioned copper based MOF HKUST-1.[36–38] Figure 6 depicts the structures of the latter two MOFs and for each one, an isoreticular counterpart is given. The design of isoreticular MOFs often implicates larger synthetic challenges: For the synthesis of IRMOF-74 with etb topology also the design of the linker molecules as well as the crystallization process of the structure exhibited challenges to overcome.[38] Nevertheless, the IRMOF-74 series includes linkers varying from 7 Å up to 50 Å, resulting in frameworks with pore apertures up to 98 Å, where within the pores of the wider representatives larger molecules like vitamin B12 (with a dimension of 27 Å) and even proteins can be infiltrated.[38,39]
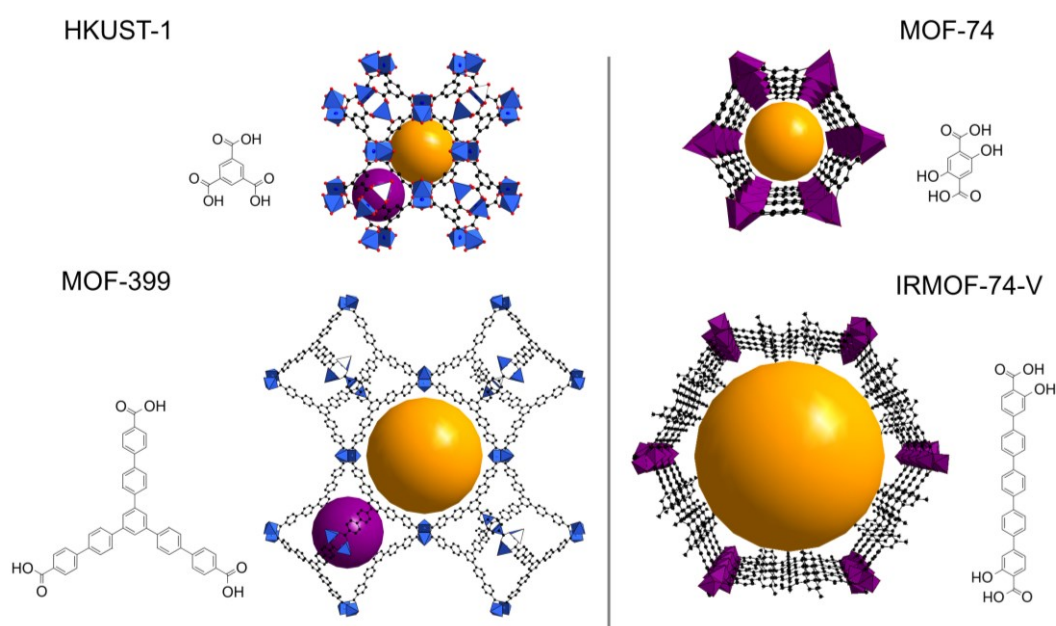
Figure 6. Schematic representation of two exemplary isoreticular MOF systems: HKUST-1 and its isoreticular counterpart MOF-399 and MOF-74 and the isoreticular analogue IRMOF-74.

As an example for a MOF build of a tritopic organic linker, HKUST-1 is depicted in Figure 6. The most prominent isoreticular frameworks of HKUST-1 are PCN-6 and MOF-399 (the latter one is shown in Figure 6).[40] In PCN-6 the organic linker 4,4′,4″-s-triazine-2,4,6-triyl-tribenzoic acid (TATB) connects the copper paddlewheels instead of BTC in HKUST-1, while MOF-399 possesses 4,4′,4″-benzene-1,3,5-triyl-tribenzoate (BTB) linkers.[35,41] Up to now, MOF-399 has the lowest known density in regard to metal-organic frameworks with 0.126 g/cm^{-3}.[40]

A major drawback during the synthesis of isoreticular MOFs is the interpenetration of the networks. Those interwoven frameworks are formed when the size of the linker molecule exceeds a critical length. The pores of the framework exhibit enough space for a second framework filling these voids, thus resulting in two frameworks being located in each other's pore system. Thereby the resulting pore volume is reduced.[42,43] In fact, the IRMOF series of MOF-5 possesses only two structures which do not form interpenetrated frameworks (H_2BDC and 2,6-H_2NDC), while the remaining structures tend to form twofold, entangled interpenetrated structures.[34] The somewhat simple solution in the case of the MOF-5 series is the use of more diluted educt solutions. This leads in most of the structures to non-interpenetrated isostructural frameworks.[34] Another approach to prevent the interpenetration of a framework, is presented by Wöll and coworkers.[44] They used a step-by-step method called liquid-phase epitaxy to suppress the formation of an interpenetrated framework.[44]

3.3 Modulation of properties

The previous subchapters imparted a first impression of the immense variety of MOFs. This subchapter covers the opportunities of pre-synthetic design and in situ functionalization as well as the approach of post-synthetic modifications (PSMs) as a possibility to overcome the limitations of the former with regard to tailorability.

3.3.1 Pre-synthethic design

Introductions of functional groups

The pre-synthetic design of MOFs offers the opportunity of chemical and structural control and, therefore, is a crucial part in order to realize highly tailored materials with unique properties like porosity, stability and even conductivity, which predestines them for unique applications.[45] By the prior design of the linker molecules, a variety of functionalities can be introduced into the final material.[46–49] Bipyridine-based or amino-substituted linkers are often used to specialize the properties of the MOFs even further. For the latter one, two intensively studied MOFs are UiO-66 (University of Oslo) and its derivate UiO-66-NH_2 as well as MIL-125 (Materials Institute Lavoisier) and MIL-125-NH_2. The Zr-based MOF UiO-66 consists of a 12-fold connecting zirconia based SBU and terephthalic acid as linking molecule. By changing the organic linker into 2-aminoterephthalic acid, the CO_2/N_2 and CO_2/CH_4 adsorption selectivities can be drastically improved, while the surface area and pore volume show no significant change.[48] In case of the titanium based MIL-125, which is linked by BDC molecules, the introduction of the amine group leads to a ligand-to-metal charge transfer, based on the electron donating feature of the introduced group, which results in the capability to reduce CO_2 photocatalytically even under visible light irradiation.[50]

Intrinsic electrical conduction

Via the pre-design of organic linkers and the well-considered insertion of metal centers, the synthesis of electrical conducting MOFs is feasible. The main difficulties in the preparation of conductive MOFs are the relatively low concentrations and the low mobility of free charge carriers such as electrons and holes, due to the porous character of the frameworks.[51,52] To enhance the amount of freely moving charge carriers within the material metal ions with easily accessible electrons or holes and redox-active linkers which possess stable radical anions or cations, are desirable building blocks.[51] And even then, long range charge transport remains a problem to overcome, due to highly localized and isolated energy levels, reasoned in the poor

overlap between the linker and metal ion orbitals, which prevents a high electrical conductivity of more than 100 S/cm.[51–53]

In order to design conductive MOFs, two possible main charge-transport mechanisms should be taken into account: hopping transport and band transport.[54] Within the hopping transport, the charge carriers (electrons and/or holes) are localized at specific sites with discrete energy levels and are able to hop between neighbouring sites, while according to the band transport mechanism, the charge carrier's wavenfunctions are delocalized over the molecule.[52,55] The long-range charge transport can either be achieved by through-bond or by through-space approaches.[51–53,56] The through-bond approach is promoted by the covalent bondings between metals and ligands, based on an adequate overlap of the orbitals and leading to the delocalization of π-electrons of the conjugated organic linker over the whole framework.[51–53,56] In contrast, the through-space approach relies on non-covalent interactions such as π-π stackings between the organic components.[51–53,56]

The first conducting 3D MOF, Cu[Cu(PDT)$_2$] (PDT=2,3-pyrazinedithiolate), was published in 2009 by Kitagawa et al. and exhibits an electrical conductivity of $6 \cdot 10^{-4}$ S/cm at room temperature.[57] A through-bond mechanism is suggested for this material, where electrons from the mixed-valent Cu centers can move through the conjugated pdt linker molecules.[51,57] In 2015 Dincă et al. published a design principle of conductive MOF-74 analogues which exhibit an efficient overlap between the d-orbitals of the metals and the p-orbitals of the ligands, resulting in long-range charge movements.[58] The highest conductivity within this structural series of MOF-74 showed Fe$_2$(DSBDC) with a value of $3.9 \cdot 10^{-6}$ S/cm. Due to the overlapping iron-d and sulfur-p orbitals, charge carriers (holes) are able to hop through the valence band.[58]

A closer look at the highest, recently published, conducting frameworks reveals that, among these, a number of planar MOFs with extended 2D π-conjugation and graphene-like structures are situated.[53,56] These two dimensional MOFs, whose charge transport takes place via the through-bond approach, possess Cu(II), Ni(II), Co(II) or Pt(II) ions in a square planar arrangement and are linked by trigonal hexamino-, hexahydroxy-, hexathio-substiuted benzene or triphenylene molecules.[51,56,59–63] Some of these MOFs exhibit electrical conductivity values comparable with the previously described 3D frameworks, as for example the Ni$_3$(HTTP)$_2$[64] ($3.6 \cdot 10^{-4}$ S/cm), consisting of 2,3,6,7,10,11-hexathiotriphenylene (HTTP) linkers combined with divalent nickel ions. Whereas others exhibit reasonable high conductivity values, for example the Ni$_3$(HITP)$_2$[65,66] (40 S/cm), which is build up

with the organic linker 2,3,6,7,10,11-hexaminotriphenylene (HITP), as well as Cu-BHT[67] (280 S/cm for compressed nanocrystal pellets and 1580 S/cm for thin films), consisting of copper(II) and benzenehexathiol units.

3.3.2 Post-synthetic design

While the discussed pre-design offers various opportunities to tailor MOFs perfectly suited for the incorporation into industrial applications, this method is limited to a number of adequate substituents and linkers. A smart solution to overcome this lack of synthetic capabilities and to enable the incorporation of functional groups or appropriate metal species which are not accessible by conventional methods is the post-synthetic modulation (PSM). In the following part, some feasible approaches of PSM will be presented.

Linker and metal ion exchange

A variety of frequently used approaches of PSM, such as the installation, modification or exchange of linker molecules or the exchange of metal ions, will be discussed in the following sections.

The conversion of ZIF-8 into ZIF8-A can be named as an adequate example for a post-synthetic linker exchange.[68] While ZIF8-A cannot be achieved via a direct synthesis, the post-synthetic modification offers a possibility to incorporate functional amine groups just by soaking the pristine ZIF-8 in a solution containing 3-amino-1,2,4-triazole (Atz).[68] By varying the reaction time, Atz conversion rates from 15 % up to 74 % can be reached, leading to enhanced CO_2 adsorption selectivity and offering the opportunity for further chemical modification and crosslinking.[68]

Via PSM, linkers can not only be exchanged with existing ones but also be inserted, which could even lead, for example, to the construction of 3D frameworks out of 2D ones. Kitaura et al. presented the formation of a 3D copper-based MOF by linking the two-dimensional layered framework [Cu(TFBDC)-(MeOH)] (TFBDC = tetrafluoro-benzene-1,4-dicarbocylate), which possesses Cu^{II} ions with axial MeOH ligands that are bridged by the TFBDC ligands, with a pillar ligand called DABCO (1,4-diazabicyclo[2.2.2]octane).[69] An identical approach was presented by Chen et al. by linking a two-dimensional Zn-based MOF with the same pillar molecule.[70] The obtained 3D framework is even able to undergo a retransformation into the 2D starting material.[70]

Besides the exchange and insertion of linker molecules, the already incorporated linker can undergo further chemical reactions resulting in the formation of new

covalent bonds. The often introduced amino-functionalized linker is able to undergo a wide range of reactions as shown in Figure 7. IRMOF-3, the amino-containing isoreticular analog of MOF-5, as well as MIL-125(NH$_2$) and UiO-66-NH$_2$ can undergo a formation into the corresponding amide-functionalized framework by coupling with an acid anhydride.[71,72] Furthermore the incorporation of alkyl-, imine-, amine-, sulfonic acid-, azide- or carboxylic acid-functional groups is possible via post-synthetic approaches which can be formed by modifying the NH$_2$-functionalized MOFs.[72–80] By introducing the previously mentioned functionalities, drawbacks as stability issues and the general purification of the resulting MOFs can occur and need to be compensated.[2] The conversion rate is also a critical point to be named, since the incorporation highly depends in the relative size of the functional molecule to be incorporated and therefore needs to be taken into account.[71]
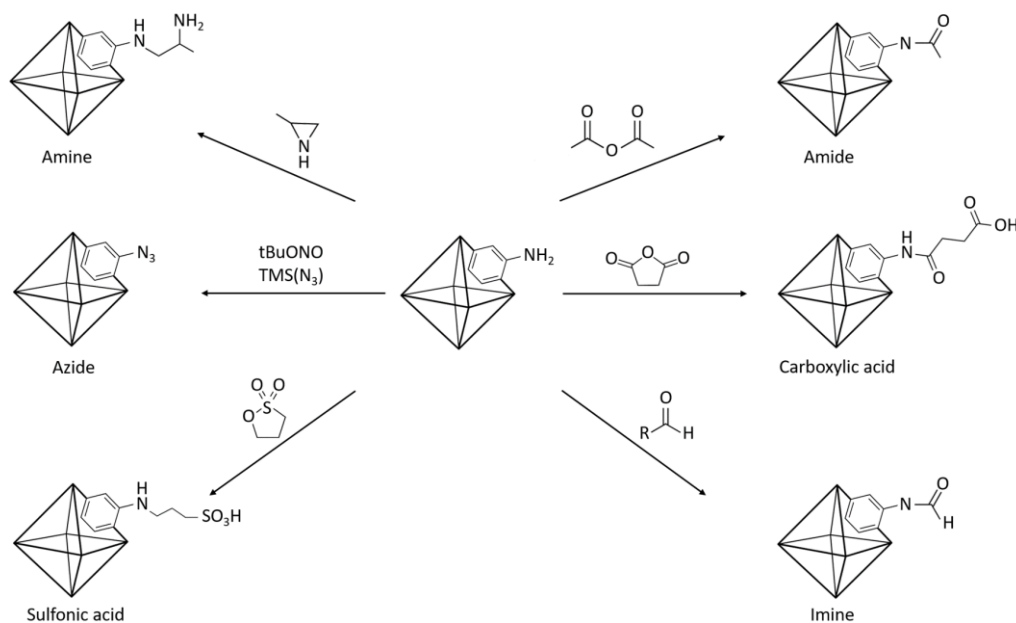
Figure 7. Scheme of an exemplary amino-functionalized MOF and post-synthetic approaches to incorporate amine-, azide-, sulfonic acid-, amide-, carboxylic acid- and imine-functionalizations into the framework.

Similar to the limited choice of linker molecules, some SBUs can only be formed with one specific type of metal ions. To overcome this limitation, metal ion exchange reactions can be performed, a prominent example being the Zr-based UiO-66. By exposing UiO-66(Zr) to titanium- or hafnium-containing DMF solutions, Ti(IV) and Hf(IV) cations can be introduced into the framework.[81,82] Especially titanium is not able to form the SBU clusters needed of UiO-66.[81,82] Depending on the titanium-salt, different amounts can be incorporated, based on the reactivity and instability of the metal salts.[81,82] TiBr$_4$ showed the lowest exchange rate compared to TiCp$_2$Cl$_2$ or TiCl$_4$(THF)$_2$ (Cp = η^5-cyclopentadienyl, THF = tetrahydrofuran).[81,82] By using

$TiCl_4(THF)_2$ over 90 % of the starting particles can be converted into Ti^{4+} (~38 wt% of the metal ions in the sample).[81,82] In the case of hafnium incorporation into the framework only in 20 % of the particles the zirconia ions were exchanged by using $HfCl_4$.[81,82] Another example of a successful transition metal exchange is SUMOF-1.[83] The SBUs are build up of paddle-wheel metal clusters which are linked by the tritopic BTB (1,3,5-triyl-benzoic acid) and the ditopic BPy (4,4'-bipyridine) molecules.[83] Here, Zn^{2+} can be reversibly exchanged by Co^{2+}, Ni^{2+} or Cu^{2+}.[83] The exchange rate of the metal ion within the framework depends on the stabilities of the forming metal clusters and is in good accordance with the Irving-Williams series.[83] While 50 % of the Zn^{2+} ions are replaced by Cu^{2+} within one hour, a 95 % conversion rate can be achieved within three days and an almost complete exchange of 99 % is accomplished within three months.[83] By soaking the SUMOF-1(Cu) in a Zn-containing DMF solution, 38 % of the Cu^{2+} ions could be re-exchanged by Zn^{2+} ions within three months.[83]

The exchange of metal ions or linker molecules possesses a high potential for introducing novel functionalities into already formed and otherwise unachievable MOFs. Both approaches, the post-synthetic modification of metal ions and linker molecules, can also be combined, as for example Farha and coworkers reported for the already known $Zn_2(TMBDC)_2(BPy)$ (tmbdc = tetramethylterephthalate), resulting in an even more specific functionalized framework $Ni_2(NDC)_2(DABCO)$ (NDC = 2,6-naphthalenedicarboxylate) with completely replaced components.[84]

PSM polymerization and crosslinking

The incorporation of separation-active MOFs into polymers could potentially lead to the deployment in separation applications, providing a simplified hybrid system design for continuous processes.[85] Therefore, the physical interaction between the polymer and MOF needs to be improved by post-synthetic modification or crosslinking mechanisms, resulting in decreased voids or defects and an improved mechanical stability.[85] Post-synthetic polymerization of MOF/polymer membranes might be the bridging point between MOF membranes possessing ideal selectivities/high fluxes and mixed matrix membranes which possess the advantages of easy processability, flexibility and durability due to the use of polymers.[85] In this context, Venna et al. presented a post-synthetic modification approach featuring UiO-66-NH$_2$ which improved the interaction with the polymer Matrimid.[86] By introducing a phenyl acetyl group, hydrogen bondings and π-π stacking interactions are developed between

polymer and MOF (see Figure 8).[86] These interactions result in an increase of the CO_2 permeability by 200 % and the selectivity by 25 % in CO_2/N_2 systems.[86]

Another approach to enhance the polymer/MOF interaction is the indirect and direct crosslinking. Here, the MOF is covalently bound to the polymer.[87] An indirect crosslinked mixed matrix membrane (MMM) can be achieved with ZIF-90 particles and Matrimid, leading to an improved H_2/CO_2 separation factor.[87] The sodalite structure of ZIF-90 consists of Zn(II) ions and 2-carboxaldehyde imidazolate linkers.[87] By introducing ethylenediamine as bridging agent into the system, imine condensation reactions take place between ethylenediamine and ZIF-90, as well as between ethylenediamine and Matrimid (see Figure 8).[87]
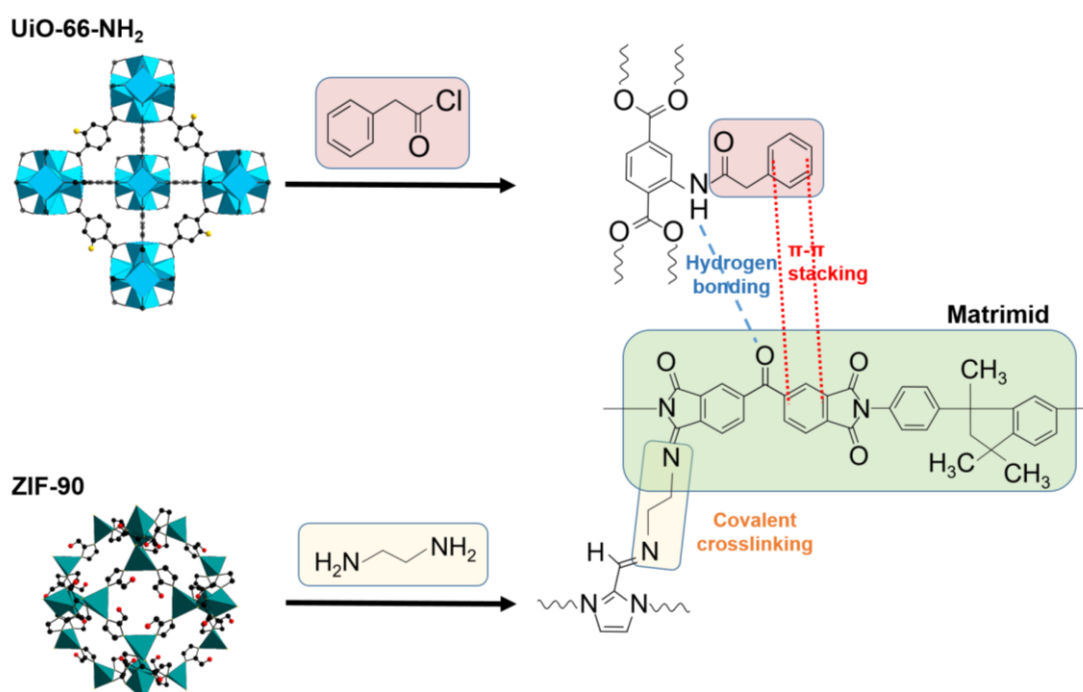
Figure 8. Scheme demonstrating the interactions between the Matrimid polymer and the post-synthetically modified MOFs UiO-66-NH₂ and ZIF-90. The phenyl acetyl functionalized UiO-66-NH₂ interacts with the polymer via hydrogen bonding and π-π stacking. The ethylenediamine modified ZIF-90 is covalently bound to Matrimid.

Guest encapsulation and guest induced electrical conductivity

Besides the already introduced approaches of PSM, guest molecules can be encapsulated within the pores of MOFs, leading to functional properties like catalytically active sites or electrical conductivity.[88–94]

While the pre-synthetic design of conducting MOFs focuses on the incorporation of conductive ligands in order to achieve a good overlap between the linker and metal ion orbitals, non-conductive MOFs can be infiltrated with guest molecules to obtain a certain conductivity. A wide variety of guest molecules can lead to the development

of conductivity, as for example polymers[93,95–97], metal species[74,94,98] or redox-active dyes.[89–91,99]

The post-synthetic introduction of monomer units of polymers, such as polypyrrole or polyaniline, and the subsequent polymerization of these, can result in a significant increase in conductivity, as Dhara and coworkers[93] were recently able to demonstrate. They presented a 3D fluorescent MOF [Cd(NDC)$_{0.5}$(PCA)] (NDC = 2,6-napthalenedicarboxylic acid, PCA = 4-pyridinecarboxylic acid) whose conductivity was enhanced from 10^{-12} S/cm up to ~10^{-3} S/cm.[93] A second possibility to derive a conducting material is the infiltration with metal species, like for examples nanoclusters[94] or nanoparticles[74]. Han et al.[94] presented a general strategy for achieving electrical conductivity in MOFs while preserving largely opened and accessible pores by introducing Ag-nanoclusters. The third option, which was already mentioned before, is the infiltration with redox-active molecules like ferrocene, iodine[92,100,101], TCNQ[90,91] (tetracyanoquinodimethane) or TTF[89] (tetrathiafulvalene). In the case of doping MOFs with iodine, it is assumed, that those are most probably situated in the MOF pores in a highly ordered way.[100] Allendorf and coworkers were able to enhance the conductivity of Cu[Ni(pyrazine2,3-dithiolate)$_2$] up to 4 orders of magnitude ($1 \cdot 10^{-8}$ S/cm) by introducing iodine, due to a partial oxidation of the nickel centers.[92] It was also Allendorf and coworkers, who infiltrated TCNQ into HKUST-1 in 2014.[91] Here, they were able to tune the electrical conductivity up to a value of 0.07 S/cm just by soaking the MOF in a saturated solution of TCNQ in dichloromethane. Due to the coordination of TCNQ at the unsaturated Cu-paddlewheel nodes, these were crosslinked and paved the way for through-bond charge transport.[91] A comparable concept was presented by Shiozawa et al., who infiltrated TCNQ into Co-MOF-74. Unfortunately, this MOF was not as conductive as the TCNQ-HKUST-1 compound, which indicates, that the honeycomb structure of MOF-74 does not support the same continuous conducting path as it was suggested for HKUST-1.[90]

3.3.3 In situ functionalization

After reviewing the pre- and post-synthetic design strategies, the following part will cover the approach of in situ functionalization, discussing the incorporation of a second material during the synthesis of a MOF.[102] In situ functionalization can be advantageous in the area of trapping large molecules, which could not be incorporated by PSM because they do not fit through the pore openings of the

MOFs.[102] Furthermore, when nanoparticles are embedded into MOFs, the Ostwald ripening process of these particles or their aggregation can be prevented.[2,102]

An appropriate example for in situ functionalization is the encapsulation of an enzyme within the structures of a MOF.[103] Therefore, it is important to choose a MOF which is synthesized under ambient conditions, to preserve the activity and stability of the enzyme.[103] A pioneering work within this area is published by Lyu et al., who synthesized ZIF-8 with encapsulated Cyt c enzyme molecules.[104] In order to prevent the aggregation of the enzyme, polyvinylpyrrolidone (PVP) was added.[104] Other studies encapsulated catalase (CAT) enzymes in ZIF-90 and were able to show that even though the catalytic activity of the enzyme was lowered by the encapsulation process, the MOF, acting as a shell, enhanced the systems stability.

The encapsulation of nanoparticles into MOFs can lead, for example, to an improvement of their catalytically activity as well as their selectivity, as it was investigated for copper nanoparticles embedded into UiO-66.[105] The Cu⊂UiO-66 composite was obtained by adding pre-synthesized Cu nanoparticles into the precursor solution of the MOF.[105] This approach resulted in higher selectivities and yields regarding the production of methanol from CO_2.[105]

3.4 Co-MOF-74

In the following chapter, the structure and properties of MOF-74 will be clarified. The crystal structure of the three dimensional MOF-74 with honeycomb topology is comprised of one-dimensional channels, with a diameter of 11 Å, build up of metal atoms and the linker 2,5-dihydroxyterephthalic acid (see Figure 9).[106] The SBU of Co-MOF-74 is based on cobalt ions which are coordinated in a distorted octahedral fashion by six oxygen atoms.[106] The organic linker contributes all six of its oxygen atoms to the structure, building coordinative bonds with the cobalt center.[106]

Each cobalt center is coordinated to five oxygen atoms of different organic linkers and to one oxygen atom of a water molecule.[106] One oxygen of the carboxylate group and the oxygen of the hydroxide group are each coordinated to two cobalt atoms and the second oxygen atom of the carboxylate group is only coordinated to one cobalt atom.[106] This construction leads to cobalt-oxygen octahedra which are linked on the edges in a cis orientation, resulting in a helix which is situated parallel to the c axis.[106] By the removal of water, the structure changes from octahedral coordination to square-pyramidal coordination and features open metal sites which are aligned insight of the hexagonal channels.[107]

octahedrally
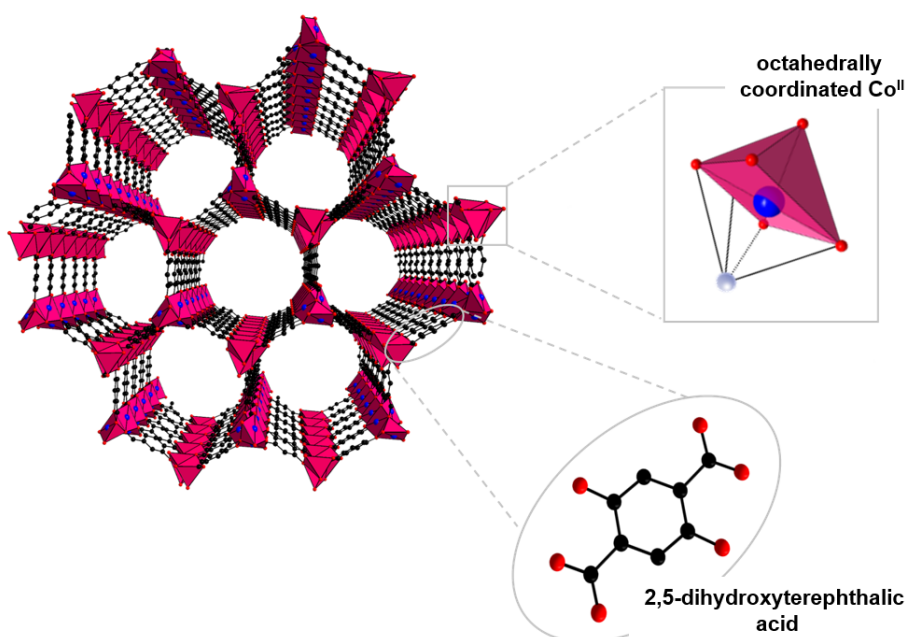coordinated Co^{II}

2,5-dihydroxyterephthalic
acid

Figure 9. Crystal structure of Co-MOF-74 with zoom-in to the octahedrally coordinated Co-sites, which are lining the insides of the pore and bridged by the organic linker 2,5-dihydroxyterephtalic acid. The open metal site is indicated by a white sphere.

MOF-74, which is also called CPO-27, M_2(DOBDC) or M_2(DHTP), can be synthesized using various transition metal ions (M), such as Zn^{2+}, Mg^{2+}, Co^{2+}, Mn^{2+}, Fe^{2+} or Ni^{2+}.[108] Yaghi et al. even presented a study, where up to 10 different divalent metal ions were incorporated into one stable structure via a solvothermal approach.[109] Besides the already named metal ions, also metal species which cannot be employed into the structure via the solvothermal route such as Ca^{2+}, Sr^{2+}, Ba^{2+} and Cd^{2+} can be incorporated via the multi-metal one-pot reaction.[109] The main synthesis route of MOF-74 is build upon solvothermal conditions, but also more economically and greener methods like milling or room temperature synthesis routes can lead to the formation of MOF-74.[110–113]

Although the pore size of MOF-74 would in general be too large for gas separation purposes, its open metal sites enable it for separations of binary mixtures like ethane/ethane, propene/propane and selective CO_2 adsorption.[114–117] The double bonds of alkenes enable them to develop π-backbonding interactions, while alkanes are not able to interact with the open metal sites.[118] Further responses due to interactions with the open metal sites were observed for the guest molecules NO, CO, C_2H_4 or H_2.[119–121] Despite the possible application within the field of separation, its large specific surface area and good stability predestines MOF-74 for the field of catalysis, like when it is employed in the cycloaddition reaction between styrene oxide and CO_2.[122]

3.5 UiO-66

The structures of the zirconium-based UiO-MOFs (UiO = University of Oslo) were first published in 2008 and have gained increasing interest since then due to their extremely high chemical and thermal stability.[37,123] UiO-66 is composed of $Zr_6O_4(OH)_4$ clusters which are linked with 1,4-benzenedicarboxylic acid (BDC) molecules (Figure 10).[37,123] The clusters are constructed of Zr_6-octahedrons which are alternatingly capped by μ_3-O and μ_3-OH groups.[37,123] The edges of the polyhedra are connected to the carboxylate groups of the linker molecules, forming a $Zr_6O_4(OH)_4(CO_2)_{12}$ cluster.[37,123] Consequential to the described structure, UiO-66 possesses a pore system which is composed of octahedral pores with a free diameter of 11 Å, surrounded by tetrahedral pores with a free diameter of 8 Å.[124] The pores are interconnected by triangular windows with a diameter of 5-7 Å.[124] The overall structure of the 12-fold connected MOF can be described by the fcu (face-centered cubic) topology.[26,75,123] By replacing of BDC with biphenyl-4,4´-dicarboxylic acid (BPDC) the isoreticular MOF UiO-67 can be obtained, which possesses larger pores due to the larger incorporated linker molecules. Furthermore, UiO-66 is an often used example with regard to linker design strategies either via in situ functionalization or PSM approaches.
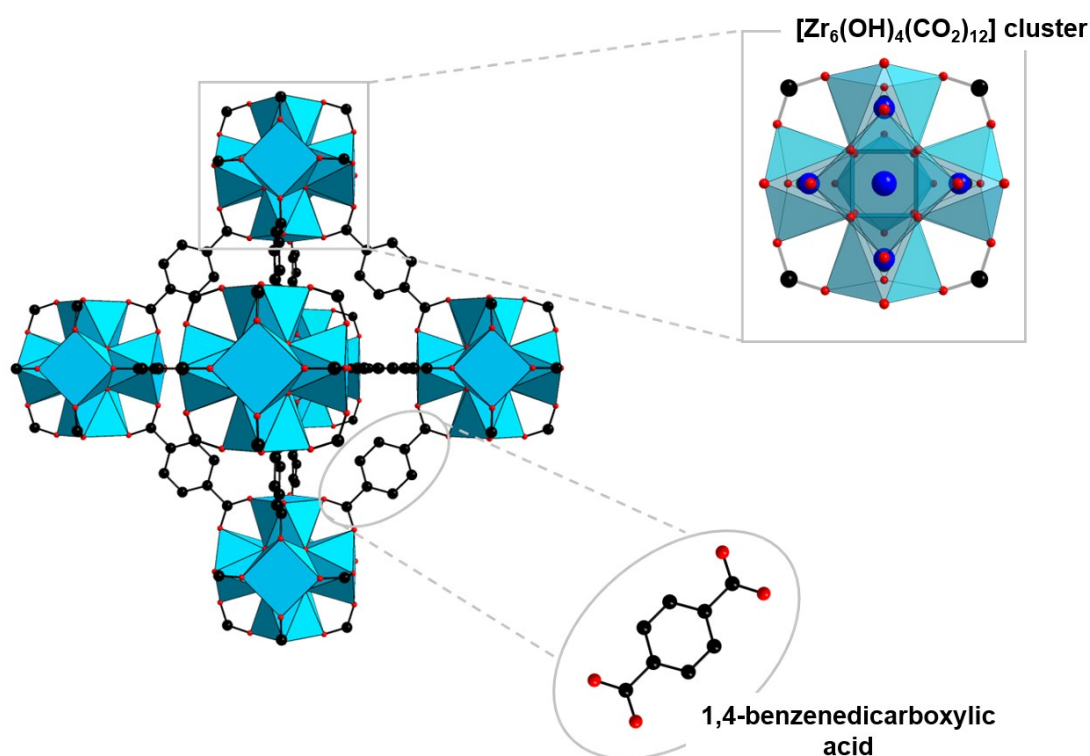
Figure 10. Crystal structure of UiO-66 with zoom-in to the [Zr$_6$(OH)$_4$(CO$_2$)$_{12}$] cluster and the organic linker 1,4-benzenedicarboxylic acid.

In situ strategies, for example, lead to isoreticular structures exhibiting functional groups like –NH$_2$, -Br, –NO$_2$ or naphthalene, while PSM of UiO-66-NH$_2$ can result in a variation of amide modified frameworks when alkyl anhydrides such as acetic-octanoic or maleic anhydride are employed into the PSM route.[75,76,78] Luan et al. reported the development of a SO$_3$H-functionalized UiO-66 framework by using 1,3-propanesultone in a PSM step.[79] Compared to other MOFs, like MOF-74 which begins to collapse at 220-240 °C and is decomposed at 300-360 °C, Zr-based frameworks exhibit an extraordinary thermal stability up to 450 °C and can also be soaked in organic solvents and acidic solutions without being damaged.[37,125–130]

As also stated before for MOF-74, UiO-66 can be synthesized via a multitude of synthetic routes. Despite the first documented synthesis of UiO-66 being a solvothermal method in N,N-dimethylformamide (DMF), approaches including alternative solvents like water-, acetone or cyrene, as well as microwave assisted synthesis, mechanochemical synthesis and chemical vapour deposition were developed, to name only a few.[123] As diverse as the synthesis are the possible applications, which can be found in various fields, such as catalysis, drug delivery, sensing or separation.[48,131–135]

4 Application of MOFs

The previous chapters demonstrated the manifold characteristics of MOFs and their modular design opportunities, which accentuates their raw potential for various applications. Unfortunately, MOFs lack real industrial applications due to various reasons like chemical and thermal stability. This chapter will outline some of the possible application fields, where MOFs could be incorporated and point out the drawbacks within the specific fields. Furthermore, the couple of MOFs, which are already incorporated into commercial or industrial processes will be showcased.

4.1 Heterogeneous catalysis

Nowadays, at least 90 % of the chemical processes utilize catalysts, making it one of the key elements of industrialized processes.[136,137] By the improvement of existing catalysts or the development of new catalytic technologies, production cycles could be simplified and general costs could be significantly lowered.[136] It is needless to say, that MOFs often lack the required chemical and thermal stability, what prevents them from being introduced into (catalytic) reactions under harsh conditions. Nevertheless, MOFs can be advantageous heterogeneous catalysts due to their accessible volume and high surface areas, resulting in a high density of accessible active sites, which in turn result in an enhanced activity and therefore in a more effective catalytic material.[4,137] In order to use MOFs as catalysts, some key characteristics of their structure are desirable, such as accessible open metal sites and functionalized organic linkers, which are able to activate the reactions.[138] Within the catalytic reaction, the MOF can be either used as a support for the actual catalyst or function as a carrier of the active site like the linker, SBU or an introduced compound, such as encapsulated nanoparticles.[137,138] Several publications deal with MOFs as catalysts for versatile purposes, such as within organic reactions (C-C coupling, ring-opening reactions of epoxides), CO oxidation, CO_2 conversion or hydrogen production reactions and many more.[139–144] Two organic reactions, catalyzed by UiO-66-NH$_2$ and Cu-MOF-74 will be discussed in the following section.

Yang et al. demonstrated, that the amino-functionalized UiO-66 can be used as a catalyst for Knoevenagel condensation reactions, a coupling reaction, which is often used for the synthesis of chemicals and pharmaceuticals.[145] It was shown, that UiO-66-NH$_2$ is able to catalyze the reaction between benzaldehyde and ethyl cyanoactate in polar solvents (DMF, DMSO, EtOH), leading to ethyl trans-α-

cyanocinnamate with conversion rates of more than 90 % under mild conditions.[145] The mechanism of the UiO-66-NH$_2$ catalyzed Knoevenagel condensation is shown in Figure 11.[145] Compared to UiO-66, UiO-66-NH$_2$ shows a higher conversion rate due to the Zr site close to the –NH$_2$ group favouring the formation of an active species (aldimine intermediates) which then react with the methylene compounds.[145] The integrity of the framework and the catalytic activity was maintained even after three recycling steps.[145]
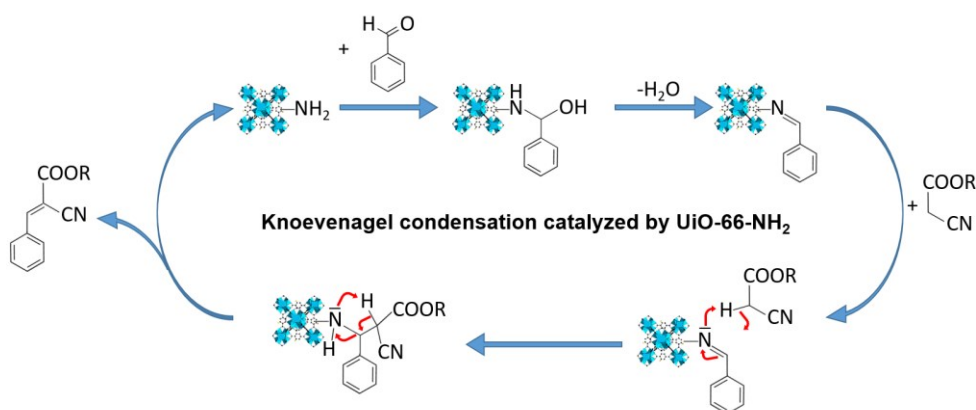
Figure 11. UiO-66-NH$_2$-catalyzed Knoevenagel condensation between benzaldehyde and ethyl cyanoactate.

Figure 12 shows the Friedel-crafts acylation of anisole, using Cu-MOF-74 as an acid catalyst.[146] Calleja et al. demonstrated, that Cu-MOF-74 possesses a high catalytic performance regarding the anisole conversion and the yield of the para-substituted product.[146] They even stated, that Cu-MOF-74 possesses a higher catalytical activity than other copper MOFs like HKUST-1 and conventional inorganic catalysts such as Al-containing zeolites (BETA or H-ZSM-5).[146]

Briefly summarized, MOFs are attractive heterogeneous catalysts, and by overcoming their lack of structural stability (for example by using water stable MOFs), the merits of the frameworks can undeniably enable them to succeed as catalysts within industrial processes and not only in proof of principle studies.
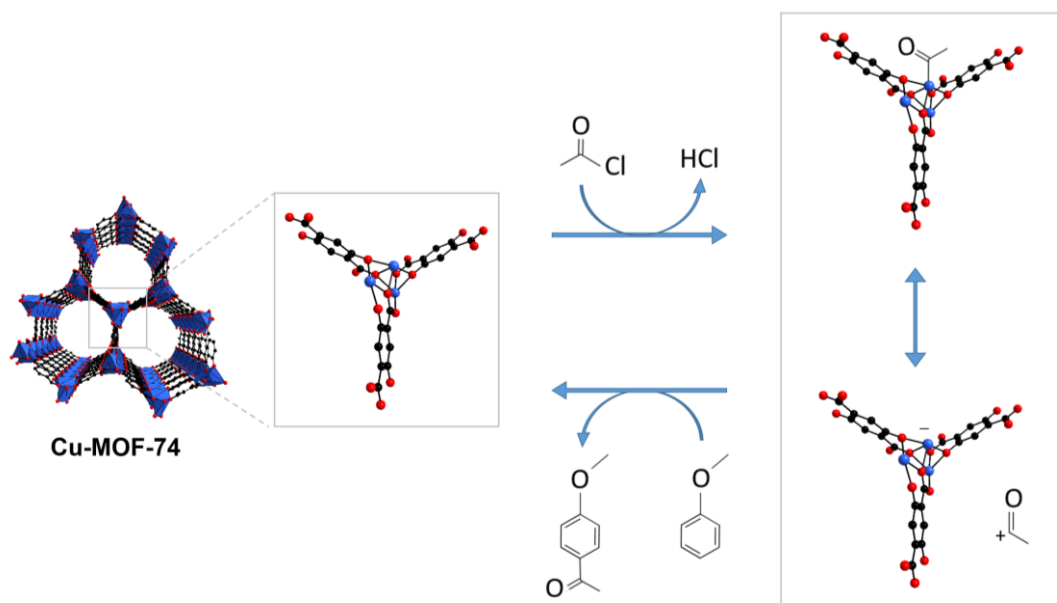
Figure 12. Mechanism of Friedel-crafts acylation of anisole, using Cu-MOF-74 as an acid catalyst.

4.2 Energy storage

Energy storage is a fundamental requirement for effectively enhancing the amount of environmentally friendly energy carriers and the production of clean energy fuels, which both are paramount to decreasing air pollution and greenhouse gas emissions. Therefore, the storage of hydrogen (H_2), which can be used as both of the previously named, and of methane (CH_4), as a component of natural gas and an alternative to fossil fuels, are often investigated research areas. For the storage of both, H_2 and CH_4, lots of publications explore the use of MOFs in order to enhance the capacity of storage reservoirs.[5,147]

For example, the coating of Pd nanocube crystals with HKUST-1 led to a 74 % higher H_2 storage capacity compared to the uncoated crystals, due to a change of the reactivity of the nanocrystals.[148] By incorporating UiO-66 into MIL-101, Ren et al. increased the H_2 uptake by 26 % or even 60 % compared to the pure MIL-101 and UiO-66.[149] They stated that the formation of structural defects within the core-shell MIL-101(Cr)@UiO-66(Zr) enhances the diffusion of H_2 into the material.[149]

Concerning the storage of CH_4, Peng et al. presented a study examining six promising MOFs, among others, HKUST-1 and Ni-MOF-74. HKUST-1 showed a volumetric methane uptake of 230 cc(STP)/cc at 35 bar and 270 cc(STP)/cc at 65 bar at room-temperature.[147] These values fulfil the volumetric target set by the Department of Energy and outperforms any values reported until then.[147] Unfortunately, the major drawback here is the collapsing of the framework, which results in a decreasing

uptake of CH_4, when HKUST-1 is compacted in order to maximize the storage capability even further.[147] This shows, that a general challenge concerning the storage of gases with MOFs, is to pack them without damaging the framework.[147] A possibility to avoid this drawback might be the design and synthesis of more rigid MOFs, e.g. by means of crosslinking, resulting in an increased resistance to mechanical pressures.[147]

4.3 Gas separation

Gas separation processes, which are widely involved in the production of chemical components for fuels, plastics or polymers, can be a crucial contributor to fields like environmental protection or the improvement of the dependent industrial processes.[6] The separation and capture of CO_2 can help with the alleviation of greenhouse effects and the separation of toxic gases like CO or ammonia from industrial processes can lead to both, the reduction of pollution and an increase in efficiency, just to name two of the advantages of gas separation approaches.[6] The separation efficiency is highly dependent on the internal porosity and surface properties of the selective material.[150] Therefore, MOFs, which can be systematically tuned in aspects of pore size and functionality by varying organic linkers or by their open metal sites, are promising materials within this field.[150] Gas separation can be classified by the involved mechanism: Thermodynamic separation, which mainly takes place in MOFs with larger pores and is based on the binding affinities between the adsorbates and the MOF, kinetic separation, which is based on the diffusivity of the gases along the pores and molecular sieving, where larger species are excluded and smaller species can diffuse through the pores.[150] By tuning the pores and adsorption sites, gas mixtures can be separated by their characteristics such as size, shape, polarity, coordination ability, polarizabilities or conformation.[150] An appropriate example for the systematical tuning of MOFs regarding separation properties was published by Wang et al.[151] They present an ethylenediamine-functionalized Mg-MOF-74 membrane which exhibits an enhanced separation performance regarding H_2/CO_2.[151] The increase was attributed to the incorporated amino groups which are bound on one side to the open metal site and therefore the molecule protrude into the channel, narrowing the effective size of the latter and retarding the carbon dioxide stronger than the hydrogen molecule.[151] In addition to that, the second amino group of the incorporated ethylenediamine is able to interact with CO_2 and to further reduce its mobility.[151]

Besides their promising tailorable features, MOFs lack several characteristics which are required for the application in separation processes, such as good mechanical and chemical stability, durability and easy upscalability. One possibility to improve these disadvantages is to introduce them into polymers to form mixed matrix membranes (MMMs). Friebe et al. presented a MMM composed of the water stable MOF UiO-66 and the polyimide Matrimid, which combines the porosity and functionalities of MOFs with the easy handleability of polymers.[152,153] The enhancement of the separation factor for H_2/CH_4 of the MMM compared to a UiO-66 membrane was attributed to a reduced pore size due to a slight infiltration of the polymer into the framework, the reduction of the frameworks flexibility and the sealing of present defect within the MOF layer.[152,153]

Another topic which needs to be considered within the field of gas separation is the capture of CO_2, which is one of the major gases responsible for the greenhouse effect.[154] The concentration of CO_2 increased from 310 ppm to over 380 ppm during the last fifty years and is expected to further rise up to 550 ppm until 2050.[138] Since a large part of the CO_2 is released from industries and the combustion of fossil fuels, one way to decrease its release is to use porous structures with high affinities toward CO_2 to capture it.[155] Here, thermal stable MOFs possessing either nitrogen-containing heterocyclic organic linkers, functional groups such as $-NH_2$ and $-OH$, inserted metal ions or open metal sites, which are able to interact with the CO_2 molecule, can be used to capture CO_2.[138] As an example for MMMs with MOF fillers for CO_2 capture, the indirect crosslinked Matrimid/ZIF-90 membrane published by Diestel et al., which was already discussed further in Chapter 2.3.2 Post-synthetic design (PSM polymerization and crosslinking), can be named.[87]

Concluding, MOFs are also a promising material within the field of gas separation, but again, the major drawbacks are their lack of stability and regenerability. Besides that, the cost effective production of MOFs, which, among other things, requires high energy efficiencies, needs to be largely improved.[150,156] Once these drawbacks are eliminated, MOFs could be utilized within the tasks of carbon capture, storage and utilization (CCSU).[157]

4.4 Gas and vapour sensors

In the 19th century, one of the first methods to detect potentially dangerous substances was used by coal miners: The canary.[158] These birds were taken along into the mine tunnels and used as a visible and audible gas detection.[158] Miners checked regularly

whether the canary stopped shaking the cage or stopped singing. These were both signs of the canary being unconscious or dead due to methane gas and in consequence they needed to evacuate their working area.[158]

Nowadays, more sophisticated sensors are used in all kinds of applications such as for various industrial processes, chemical threat detection including toxic gas monitoring, medical diagnostics, food quality control or environmental monitoring.[7,159] Most of the utilized sensors are based on films of either organic-polymers or inorganic semiconductors which either absorb or react with the analyte species in a certain way.[7] An ideal sensor requires characteristics such as high sensitivities and selectivities, a short response time, a good reliability, long-time stability including a high reusability, easy handling and low production costs.[160,161] It is unnecessary to say, that implementing these characteristics in one small device comes close to creating a farmers darling and is therefore virtually impossible. Nevertheless, MOFs have been investigated for chemical sensing applications to detect analytes such as gases, organic molecules, explosives, humidity and pH due to their unique properties like tunable structures and functionalities.[132,161] The analytes can be sensed by changes in luminescence, interferometry, localized surface plasmon resonance, impedance, electromechanical characteristics or solvatochromism.[7] Furthermore and presented hereinafter, examples of MOF and MOF/composite-based gas and vapour sensors are presented, detecting the changes in response via interferometry, conductivity, impedance, quartz crystal microbalance (QCMB) and IR spectroscopy.

An often cited MOF-based sensor for chemical vapours and gases was published by Lu and Hupp in 2010, namely a ZIF-8 based Fabry-Pérot device.[162] They used 1 μm thin films of ZIF-8 and exposed them to propane gas concentrations varying from 0 % up to 100 %.[162] It was shown via UV-Vis transmission spectra that the interference peaks were redshifted up to 49 nm due to an increase in the refractive index.[162] In addition to that, ZIF-8 possesses hydrophobic pores, which enable it to sense hydrophilic molecules such as ethanol in the presence of water.[162]

Several groups reported the capability of MOFs to give responses to water vapour. Achmann et al., for instance, presented a Fe-BTC sensor which is able to sense humidity concentrations below 10 % at low temperatures via changes of the complex impedance.[9] Ameloot et al. electrochemically grew HKUST-1 on top of a QCMB.[163] Due to the change in vibration frequency of the piezoelectrically driven quartz crystal, adsorbed masses can be detected. In this case, the HKUST-1 films showed a water sorption capacity between 25-30 wt%.[163]

In 2015, Campbell et al. presented the first MOF-based sensor, which was able to distinguish between 16 different volatile organic compounds such as alcohols, aromatics, ketones/ethers and amines.[164] This study is based on the 2D conducting MOFs $Cu_3(HHTP)_2$, $Cu_3(HITP)_2$ and $Ni_3(HITP)_2$ (HHTP = 2,3,6,7,10,11-hexahydroxytriphenylene; HITP = 2,3,6,7,10,11-hexaiminotriphenylene). They postulated charge transfer mechanisms and hydrogen bondings to be the contributors of the responsive changes.[164] Although this example shows a high selectivity regarding different vapours, the relationship between the MOFs structure and the sensing responses are not fully understood.[164,165]

Besides pure MOF-based sensors, also composite materials including MOFs have been investigated further within the field of sensorics. As stated before, embedding MOFs into polymers can improve their processability as well as their handleability. Sachdeva et al. presented a study concerning NH_2-MIL-53(Al) nanoparticles dispersed in Matrimid and drop-casted on capacitive transducer devices.[164] These showed sensitive and reversible capacitive responses even in the presence of water and possesses the ability to distinguish between methanol, ethanol, 2-propanol and water.[164] By incorporating 40 wt% of NH_2-MIL-53(Al) nanoparticles as fillers, the response for 1000 ppm methanol has increased 5-fold compared to devices coated with neat Matrimid.[164]

Schulz et al. synthesized the calixarene-based MOF $[Zr_6O_4(OH)_4(FA)_6]_2(cal)_3$ (FA = formate, cal = 1,3-alt-25,26,27,28-tetrakis[(carboxy)methoxy]calixarene)]), which can be used as a selective NO_2 detector.[166] When the MOF is exposed to the toxic gas, the accessible calixarene cavities form charge-transfer complexes with it, which results in a color change from white to dark blue.[166] The complexation of NO^+ inside the calixarene cavity, as well as the existence of NO_3^- ions which are coordinated to the Zr^{4+} metal sites could be verified via IR spectroscopy.[166] These observations were reversible, since the corresponding bands in the IR spectra disappeared over time.[166]

The aim to include MOFs into sensing devices could have great advantages regarding their selectivities and sensitivities as well as the miniaturization, however, to transfer them into commercializable applications, further research and development tasks such as functionalization, synthesis and cost optimization need to be addressed. Also, lots of studies cover the topic of vapour sensors, while only a handful research groups present MOF-based sensor approaches in which functional MOFs are used to selectively sense gases or even multi-component gas mixtures.[167]

4.5 Industrial applications of MOFs

After discussing the theoretical and purely academic applications of MOFs, the following chapter will focus on MOF-containing products for industrial applications already reached market maturity.[168-170] Researchers often acknowledge the huge commercial potential of MOFs for various fields of applications, but now, after nearly 20 years of research, only a handful of MOFs have been incorporated into commercial products.[168,169] NuMAT Technologies are selling MOF-containing gas cylinders, which store toxic gases like arsine, phosphine and boron trifluoride.[168-170] Normally, these gases are stored at high pressures in order to maximize them. However, this storage medium brings along the drawback that, in case of a leak, the gas will flow from the gas cylinder into the atmosphere.[168,169] By using MOFs, the toxic gases can be stored below atmospheric pressure and in case of a leak, gas molecules from the outside will diffuse into the cylinder and prevent a contamination of the lab.[168,169] NuMAT Technologies also collaborates with the Linde Group to develop separation and storage technologies based on MOFs.[168,169]

The company MOF Technologies launched a product called TruPick, where a MOF is used to hold the gas 1-methylcyclopropene (1-MCP), which binds on fruit enzymes and therefore blocks the binding of ethylene, preventing the ripening process of fruits.[168] By using a MOF, 1-MCP gas cylinders, which have been used for over a decade in warehouse storage containers at this time, can thus be eliminated.[168] Mosaic Materials, a chemicals and engineering company focused on the reduction of greenhouse gases by carbon capturing and gas separations, produce a MOF which, when the first CO_2 molecule is absorbed, triggers the absorption of more CO_2.[168] The mechanism behind this chain reaction is based on the insertion of CO_2 between the metal site and a bound diamine molecule. This triggers a proton transfer to the next metal diamine site, which is then activated continuing this chain reaction, resulting in 1D chains of ammonium carbonate within the channels of the MOF.[168] Furthermore, large industrial companies, such as BASF, are interested in the commercialization of MOFs: BASF invented MOF-containing tanks for methane-powered vehicles, which store double or triple the amount of gas compared to a tank without MOFs.[168] They even successfully tested this approach in methane fuel tanks of cars and trucks as a proof of principle.[168] Unfortunately, this project was suspended because the economic incentive vanished due to a drop of the oil price.[168]

The presented commercial applications are good examples for overcoming the drawbacks of MOFs, such as instability and handleability, but the main criteria for a

successful implementation into the real world is financial profit.[168] Therefore, even when a MOF provides good characteristics to be used for a certain application, cheap, scalable and green ways to synthesize them need to be developed before they can eventually compete with the state of the art materials on the market.[168]

5 References

[1] H. Li, M. Eddaoudi, M. O'Keeffe, O. M. Yaghi, *Nature* **1999**, *402*, 276–279.

[2] O. M. Yaghi, M. J. Kalmutzki, C. S. Diercks, *Introduction to Reticular Chemistry*, Wiley, **2019**.

[3] Ü. Anik, S. Timur, Z. Dursun, *Microchim. Acta* **2019**, *186*, 18–24.

[4] V. R. Remya, M. Kurian, *Int. Nano Lett.* **2019**, *9*, 17–29.

[5] A. Ahmed, S. Seth, J. Purewal, A. G. Wong-Foy, M. Veenstra, A. J. Matzger, D. J. Siegel, *Nat. Commun.* **2019**, *10*, 1568.

[6] H. Li, K. Wang, Y. Sun, C. T. Lollar, J. Li, H. C. Zhou, *Mater. Today* **2018**, *21*, 108–121.

[7] L. E. Kreno, K. Leong, O. K. Farha, M. Allendorf, R. P. Van Duyne, J. T. Hupp, *Chem. Rev.* **2012**, *112*, 1105–1125.

[8] G. Gerlach, U. Guth, W. Oelßner, *Carbon Dioxide Sensing*, Wiley-VCH, Berlin, **2019**.

[9] S. Achmann, G. Hagen, J. Kita, I. M. Malkowsky, C. Kiener, R. Moos, *Sensors* **2009**, *9*, 1574–1589.

[10] S. Seth, A. J. Matzger, *Cryst. Growth Des.* **2017**, *17*, 4043–4048.

[11] G. E. Stahl, *Georgii Ernesti Stahlii, Experimenta, Observationes, Animadversiones, CCC Numero, Chymicae Et Physicae*, Ambrosius Haude, Berlin, **1731**.

[12] J. Bartoll, *9th Int. Conf. NDT Art* **2008**, 25–30.

[13] G. B. Kauffman, *Alfred Werner: Founder of Coordination Chemistry*, Springer-Verlag Berlin Heidelberg, **1966**.

[14] E. C. Constable, C. E. Housecroft, *Chem. Soc. Rev.* **2013**, *42*, 1429–1439.

[15] K. A. Hofmann, F. Küspert, *Zeitschrift für Anorg. Chemie* **1897**, *15*, 204–207.

[16] J. H. Rayner, H. M. Powell, *J. Chem. Soc.* **1952**, 319–328.

[17] S. Nishikiori, T. Iwamoto, *J. Incl. Phenom.* **1984**, *2*, 341–349.

[18] Y. Kinoshita, I. Matsubara, Y. Saito, *Bull. Chem. Soc. Jpn.* **1959**, *32*, 1216–1221.

[19] Y. Kinoshita, I. Matsubara, T. Higuchi, Y. Saito, *Bull. Chem. Soc. Jpn.* **1959**, *32*, 1221–1226.

[20] Y. Kinoshita, I. Matsubara, Y. Saito, *Bull. Chem. Soc. Jpn.* **1959**, *32*, 741–747.

[21] B. F. Hoskins, R. Robson, *J. Am. Chem. Soc.* **1989**, *111*, 5962–5964.

[22] O. M. Yaghi, G. Li, H. Li, *Nature* **1995**, *378*, 703–706.

[23] M. Kondo, T. Yoshitomi, K. Seki, H. Matsuzaka, S. Kitagawa, *Angew. Chem. Int. Ed.* **1997**, *36*, 1725–1727.

[24] S. S. Kaye, A. Dailly, O. M. Yaghi, J. R. Long, *J. Am. Chem. Soc.* **2007**, *129*, 14176–14177.

[25] H. Furukawa, K. E. Cordova, M. O'Keeffe, O. M. Yaghi, *Science* **2013**, *341*, 1230444.

[26] M. J. Kalmutzki, N. Hanikel, O. M. Yaghi, *Sci. Adv.* **2018**, *4*, eaat9180.

[27] O. M. Yaghi, *ACS Cent. Sci.* **2019**, *5*, 1295–1300.

[28] O. M. Yaghi, M. O'Keeffe, N. W. Ockwig, H. K. Chae, M. Eddaoudi, J. Kim, *Nature* **2003**, *423*, 705–714.

[29] D. J. Tranchemontagne, J. L. Mendoza-Cortés, M. O'Keeffe, O. M. Yaghi, *Chem. Soc. Rev.* **2009**, *38*, 1257.

[30] S. S. Y. Chui, S. M. F. Lo, J. P. H. Charmant, A. G. Orpen, I. D. Williams, *Science* **1999**, *283*, 1148–1150.

[31] D. Kim, X. Liu, M. S. Lah, *Inorg. Chem. Front.* **2015**, *2*, 336–360.

[32] J. A. Mason, M. Veenstra, J. R. Long, *Chem. Sci.* **2014**, *5*, 32–51.

[33] E. Borfecchia, L. Braglia, F. Bonino, S. Bordiga, S. Øien, U. Olsbye, K. P. Lillerud, J. A. Van Bokhoven, C. Lamberti, *XAFS Techniques for Catalysts, Nanomaterials, and Surfaces*, **2017**.

[34] M. Eddaoudi, J. Kim, N. Rosi, D. Vodak, J. Wachter, M. O'Keeffe, O. M. Yaghi, *Science* **2002**, *295*, 469–472.

[35] H. Furukawa, Y. B. Go, N. Ko, Y. K. Park, F. J. Uribe-Romo, J. Kim, M. O'Keeffe, O. M. Yaghi, *Inorg. Chem.* **2011**, *50*, 9147–9152.

[36] A. Schaate, P. Roy, A. Godt, J. Lippke, F. Waltz, M. Wiebcke, P. Behrens, *Chem. Eur. J.* **2011**, *17*, 6643–6651.

[37] J. H. Cavka, S. Jakobsen, U. Olsbye, N. Guillou, C. Lamberti, S. Bordiga, K. P. Lillerud, *J. Am. Chem. Soc.* **2008**, *130*, 13850–13851.

[38] H. Deng, S. Grunder, K. E. Cordova, C. Valente, H. Furukawa, M. Hmadeh, F. Gandara, A. C. Whalley, Z. Liu, S. Asahina, et al., *Science* **2012**, *336*, 1018–1023.

[39] P. Guo, *Defect-Engeneered Metal-Organic Framework HKUST-1 and Ist Composites: Synthesis, Characterization and Application in Alcohol Oxidation*, Dissertation Ruhr-Universität Bochum, **2019**.

[40] S. Kaskel, *The Chemistry of Metal-Organic Frameworks: Synthesis, Characterization, and Applications*, Wiley-VCH, Weinheim, **2016**.

[41] D. Sun, S. Ma, Y. Ke, D. J. Collins, H. C. Zhou, *J. Am. Chem. Soc.* **2006**, *128*, 3896–3897.

[42] D. Bara, C. Wilson, M. Mörtel, M. M. Khusniyarov, S. Ling, B. Slater, S. Sproules, R. S. Forgan, *J. Am. Chem. Soc.* **2019,** *141,* 8346-8357.

[43] S. S. Han, D. H. Jung, J. Heo, *J. Phys. Chem. C* **2013**, *117*, 71–77.

[44] O. Shekhah, H. Wang, M. Paradinas, C. Ocal, B. Schüpbach, A. Terfort, D. Zacher, R. A. Fischer, C. Wöll, *Nat. Mater.* **2009**, *8*, 481–484.

[45] A. E. Baumann, D. A. Burns, B. Liu, V. S. Thoi, *Commun. Chem.* **2019**, *2*, 1–14.

[46] C. Zlotea, D. Phanon, M. Mazaj, D. Heurtaux, V. Guillerm, C. Serre, P. Horcajada, T. Devic, E. Magnier, F. Cuevas, et al., *J. Chem. Soc. Dalt. Trans.* **2011**, *40*, 4879–4881.

[47] W. Lu, Z. Wei, Z. Y. Gu, T. F. Liu, J. Park, J. Park, J. Tian, M. Zhang, Q. Zhang, T. Gentle, et al., *Chem. Soc. Rev.* **2014**, *43*, 5561–5593.

[48] G. E. Cmarik, M. Kim, S. M. Cohen, K. S. Walton, *Langmuir* **2012**, *28*, 15606–15613.

[49] S. Yuan, L. Feng, K. Wang, J. Pang, M. Bosch, C. Lollar, Y. Sun, J. Qin, X. Yang, P. Zhang, et al., *Adv. Mater.* **2018**, *30*, 1704303.

[50] Y. Fu, D. Sun, Y. Chen, R. Huang, Z. Ding, X. Fu, Z. Li, *Angew. Chem. Int. Ed.* **2012**, *51*, 3364–3367.

[51] N. Nagapradeep, K. Maity, *Electrically Conductive Metal-Organic Frameworks*, Elaboration and Applications of Metal-Organic Frameworks **2018**, 655-686.

[52] L. Sun, M. G. Campbell, M. Dincə, *Angew. Chem. Int. Ed.* **2016**, *55*, 3566–3579.

[53] C. F. Leong, P. M. Usov, D. M. D'Alessandro, *MRS Bull.* **2016**, *41*, 858–864.

[54] R. Dong, P. Han, H. Arora, M. Ballabio, M. Karakus, Z. Zhang, C. Shekhar, P. Adler, P. S. Petkov, A. Erbe, et al., *Nat. Mater.* **2018**, *17*, 1027–1032.

[55] J. Calbo, M. J. Golomb, A. Walsh, *J. Mater. Chem. A* **2019**, *7*, 16571–16597.

[56] M. Ko, L. Mendecki, K. A. Mirica, *Chem. Commun.* **2018**, *54*, 7873–7891.

[57] S. Takaishi, M. Hosoda, T. Kajiwara, H. Miyasaka, M. Yamashita, Y. Nakanishi, Y. Kitagawa, K. Yamaguchi, A. Kobayashi, H. Kitagawa, *Inorg. Chem.* **2009**, *48*, 9048–9050.

[58] L. Sun, C. H. Hendon, M. A. Minier, A. Walsh, M. Dincă, *J. Am. Chem. Soc.* **2015**, *137*, 6164–6167.

[59] M. G. Campbell, S. F. Liu, T. M. Swager, M. Dincă, *J. Am. Chem. Soc.* **2015**, *137*, 13780–13783.

[60] D. Sheberla, J. C. Bachman, J. S. Elias, C. J. Sun, Y. Shao-Horn, M. Dincă, *Nat. Mater.* **2017**, *16*, 220–224.

[61] D. Sheberla, L. Sun, M. A. Blood-Forsythe, S. Er, C. R. Wade, C. K. Brozek, A. Aspuru-Guzik, M. Dincă, *J. Am. Chem. Soc.* **2014**, *136*, 8859–8862.

[62] M. Hmadeh, Z. Lu, Z. Liu, F. Gándara, H. Furukawa, S. Wan, V. Augustyn, R. Chang, L. Liao, F. Zhou, et al., *Chem. Mater.* **2012**, *24*, 3511–3513.

[63] X. Huang, P. Sheng, Z. Tu, F. Zhang, J. Wang, H. Geng, Y. Zou, C. A. Di, Y. Yi, Y. Sun, et al., *Nat. Commun.* **2015**, *6*, 6–13.

[64] L. Mendecki, M. Ko, X. Zhang, Z. Meng, K. A. Mirica, *J. Am. Chem. Soc.* **2017**, *139*, 17229–17232.

[65] E. M. Miner, T. Fukushima, D. Sheberla, L. Sun, Y. Surendranath, M. Dincă, *Nat. Commun.* **2016**, *7*, 1–7.

[66] G. Wu, J. Huang, Y. Zang, J. He, G. Xu, *J. Am. Chem. Soc.* **2017**, *139*, 1360–1363.

[67] X. Huang, H. Yao, Y. Cui, W. Hao, J. Zhu, W. Xu, D. Zhu, *ACS Appl. Mater. Interfaces* **2017**, *9*, 40752–40759.

[68] K. Y. Cho, H. An, X. H. Do, K. Choi, H. G. Yoon, H. K. Jeong, J. S. Lee, K. Y. Baek, *J. Mater. Chem. A* **2018**, *6*, 18912–18919.

[69] R. Kitaura, F. Iwahori, R. Matsuda, S. Kitagawa, Y. Kubota, M. Takata, T. C. Kobayashi, *Inorg. Chem.* **2004**, *43*, 6522–6524.

[70] Z. Chen, S. Xiang, D. Zhao, B. Chen, *Cryst. Growth Des.* **2009**, *9*, 5293–5296.

[71] K. K. Tanabe, Z. Wang, S. M. Cohen, *J. Am. Chem. Soc.* **2008**, *130*, 8508–8517.

[72] Y. Isaka, Y. Kawase, Y. Kuwahara, K. Mori, H. Yamashita, *Angew. Chem. Int. Ed.* **2019**, *131*, 5456–5460.

[73] R. M. Abdelhameed, M. M. Q. Simões, A. M. S. Silva, J. Rocha, *Chem. Eur. J.* **2015**, *21*, 11072–11081.

[74] H. Ma, X. Li, T. Yan, Y. Li, Y. Zhang, D. Wu, Q. Wei, B. Du, *Biosens. Bioelectron.* **2016**, *79*, 379–385.

[75] R. J. Marshall, R. S. Forgan, *Eur. J. Inorg. Chem.* **2016**, *2016*, 4310–4331.

[76] K. M. Zwoliński, P. Nowak, M. J. Chmielewski, *Chem. Commun.* **2015**, *51*, 10030–10033.

[77] M. Kim, S. M. Cohen, *CrystEngComm* **2012**, *14*, 4096–4104.

[78] S. J. Garibay, S. M. Cohen, *Chem. Commun.* **2010**, *46*, 7700–7702.

[79] Y. Luan, N. Zheng, Y. Qi, J. Yu, G. Wang, *Eur. J. Inorg. Chem.* **2014**, *2014*, 4268–4272.

[80] L. L. Keenan, H. A. Hamzah, M. F. Mahon, M. R. Warren, A. D. Burrows, *CrystEngComm* **2016**, *18*, 5710–5717.

[81] Z. Yin, S. Wan, J. Yang, M. Kurmoo, M. H. Zeng, *Coord. Chem. Rev.* **2019**, *378*, 500–512.

[82] M. Kim, J. F. Cahill, H. Fei, K. A. Prather, S. M. Cohen, *J. Am. Chem. Soc.* **2012**, *134*, 18082–18088.

[83] Q. Yao, J. Sun, K. Li, J. Su, M. V. Peskov, X. Zou, *Dalt. Trans.* **2012**, *41*, 3953–3955.

[84] Y. Xu, N. A. Vermeulen, Y. Liu, J. T. Hupp, O. K. Farha, *Eur. J. Inorg. Chem.* **2016**, 4345–4348.

[85] M. S. Denny, J. C. Moreton, L. Benz, S. M. Cohen, *Nat. Rev. Mater.* **2016**, 16078

[86] S. R. Venna, M. Lartey, T. Li, A. Spore, S. Kumar, H. B. Nulwala, D. R. Luebke, N. L. Rosi, E. Albenze, *J. Mater. Chem. A* **2015**, *3*, 5014–5022.

[87] L. Diestel, N. Wang, A. Schulz, F. Steinbach, J. Caro, *Ind. Eng. Chem. Res.* **2015**, *54*, 1103–1112.

[88] W. Xiang, Y. Zhang, H. Lin, C. J. Liu, *Molecules* **2017**, *22*, 2103.

[89] I. Strauss, A. Mundstock, M. Treger, K. Lange, S. Hwang, C. Chmelik, P. Rusch, N. C. Bigall, T. Pichler, H. Shiozawa, et al., *ACS Appl. Mater. Interfaces* **2019**, *11*, 14175–14181.

[90] H. Shiozawa, B. C. Bayer, H. Peterlik, J. C. Meyer, W. Lang, T. Pichler, *Sci. Rep.* **2017**, *7*, 1–8.

[91] A. A. Talin, A. Centrone, A. C. Ford, M. E. Foster, V. Stavila, P. Haney, R. A. Kinney, V. Szalai, F. El Gabaly, H. P. Yoon, et al., *Science* **2014**, *343*, 66–69.

[92] Y. Kobayashi, B. Jacobs, M. D. Allendorf, J. R. Long, *Chem. Mater.* **2010**, *22*, 4120–4122.

[93] B. Dhara, S. S. Nagarkar, J. Kumar, V. Kumar, P. K. Jha, S. K. Ghosh, S. Nair, N. Ballav, *J. Phys. Chem. Lett.* **2016**, *7*, 2945–2950.

[94] S. Han, S. C. Warren, S. M. Yoon, C. D. Malliakas, X. Hou, Y. Wei, M. G. Kanatzidis, B. A. Grzybowski, *J. Am. Chem. Soc.* **2015**, *137*, 8169–8175.

[95] B. Le Ouay, M. Boudot, T. Kitao, T. Yanagida, S. Kitagawa, T. Uemura, *J. Am. Chem. Soc.* **2016**, *138*, 10088–10091.

[96] L. Wang, X. Feng, L. Ren, Q. Piao, J. Zhong, Y. Wang, H. Li, Y. Chen, B. Wang, *J. Am. Chem. Soc.* **2015**, *137*, 4920–4923.

[97] T. C. Wang, I. Hod, C. O. Audu, N. A. Vermeulen, S. T. Nguyen, O. K. Farha, J. T. Hupp, *ACS Appl. Mater. Interfaces* **2017**, *9*, 12584–12591.

[98] Z. Guo, D. K. Panda, K. Maity, D. Lindsey, T. G. Parker, T. E. Albrecht-Schmitt, J. L. Barreda-Esparza, P. Xiong, W. Zhou, S. Saha, *J. Mater. Chem. C* **2016**, *4*, 894–899.

[99] S. K. Bhardwaj, N. Bhardwaj, R. Kaur, J. Mehta, A. L. Sharma, K. H. Kim, A. Deep, *J. Mater. Chem. A* **2018**, *6*, 14992–15009.

[100] M. H. Zeng, Q. X. Wang, Y. X. Tan, S. Hu, H. X. Zhao, L. S. Long, M. Kurmoo, *J. Am. Chem. Soc.* **2010**, *132*, 2561–2563.

[101] X. Zhang, I. Da Silva, R. Fazzi, A. M. Sheveleva, X. Han, B. F. Spencer, S. A. Sapchenko, F. Tuna, E. J. L. McInnes, M. Li, et al., *Inorg. Chem.* **2019**, *58*, 14145–14150.

[102] J. D. Sosa, T. F. Bennett, K. J. Nelms, B. M. Liu, R. C. Tovar, Y. Liu, *Crystals* **2018**, *8*, 325.

[103] J. Mehta, N. Bhardwaj, S. K. Bhardwaj, K. Kim, *Coord. Chem. Rev.* **2016**, *322*, 30–40.

[104] F. Lyu, Y. Zhang, R. N. Zare, J. Ge, Z. Liu, *Nano Lett.* **2014**, *14*, 5761–5765.

[105] B. Rungtaweevoranit, J. Baek, J. R. Araujo, B. S. Archanjo, K. M. Choi, O. M. Yaghi, G. A. Somorjai, *Nano Lett.* **2016**, *16*, 7645–7649.

[106] P. D. C. Dietzel, Y. Morita, R. Blom, H. Fjellvåg, *Angew. Chem. Int. Ed.* **2005**, *44*, 6354–6358.

[107] Q. Zhang, B. Li, L. Chen, *Inorg. Chem.* **2013**, *52*, 9356–9362.

[108] T. Xiao, D. Liu, *Microporous Mesoporous Mater.* **2019**, *283*, 88–103.

[109] L. J. Wang, H. Deng, H. Furukawa, F. Gándara, K. E. Cordova, D. Peri, O. M. Yaghi, *Inorg. Chem.* **2014**, *53*, 5881–5883.

[110] N. L. Rosi, J. Kim, M. Eddaoudi, B. Chen, M. O'Keeffe, O. M. Yaghi, *J. Am. Chem. Soc.* **2005**, *127*, 1504–1518.

[111] C. Chmelik, A. Mundstock, P. D. C. Dietzel, J. Caro, *Microporous Mesoporous Mater.* **2014**, *183*, 117–123.

[112] P. A. Julien, K. Užarević, A. D. Katsenis, S. A. J. Kimber, T. Wang, O. K. Farha, Y. Zhang, J. Casaban, L. S. Germann, M. Etter, et al., *J. Am. Chem. Soc.* **2016**, *138*, 2929–2932.

[113] Y. Yue, Z. A. Qiao, P. F. Fulvio, A. J. Binder, C. Tian, J. Chen, K. M. Nelson, X. Zhu, S. Dai, *J. Am. Chem. Soc.* **2013**, *135*, 9572–9575.

[114] U. Böhme, B. Barth, C. Paula, A. Kuhnt, W. Schwieger, A. Mundstock, J. Caro, M. Hartmann, *Langmuir* **2013**, *29*, 8592–8600.

[115] A. Luna-Triguero, J. M. Vicent-Luna, T. M. Becker, T. J. H. Vlugt, D. Dubbeldam, P. Gómez-Álvarez, S. Calero, *ChemistrySelect* **2017**, *2*, 665–672.

[116] Y. S. Bae, C. Y. Lee, K. C. Kim, O. K. Farha, P. Nickias, J. T. Hupp, S. T. Nguyen, R. Q. Snurr, *Angew. Chem. Int. Ed.* **2012**, *51*, 1857–1860.

[117] H. Y. Cho, D. A. Yang, J. Kim, S. Y. Jeong, W. S. Ahn, *Catal. Today* **2012**, *185*, 35–40.

[118] I. Strauss, A. Mundstock, D. Hinrichs, R. Himstedt, A. Knebel, C. Reinhardt, D. Dorfs, J. Caro, *Angew. Chem. Int. Ed.* **2018**, *57*, 7434–7439.

[119] F. Bonino, S. Chavan, J. G. Vitillo, E. Groppo, G. Agostini, C. Lamberti, P. D. C. Dietzel, C. Prestipino, S. Bordiga, *Chem. Mater.* **2008**, *20*, 4957–4968.

[120] S. Chavan, F. Bonino, J. G. Vitillo, E. Groppo, C. Lamberti, P. D. C. Dietzel, A. Zecchina, S. Bordiga, *Phys. Chem. Chem. Phys.* **2009**, *11*, 9811–9822.

[121] T. Pham, K. A. Forrest, R. Banerjee, G. Orcajo, J. Eckert, B. Space, *J. Phys. Chem. C* **2015**, *119*, 1078–1090.

[122] K. Xu, A. M. P. Moeljadi, B. K. Mai, H. Hirao, *J. Phys. Chem. C* **2018**, *122*, 503–514.

[123] M. Taddei, *Coord. Chem. Rev.* **2017**, *343*, 1–24.

[124] D. I. Kolokolov, A. G. Stepanov, V. Guillerm, C. Serre, B. Frick, H. Jobic, *J. Phys. Chem. C* **2012**, *116*, 12131–12136.

[125] H. Jiang, Q. Wang, H. Wang, Y. Chen, M. Zhang, *ACS Appl. Mater. Interfaces* **2016**, *8*, 26817–26826.

[126] M. Mukoyoshi, H. Kobayashi, K. Kusada, M. Hayashi, T. Yamada, M. Maesato, J. M. Taylor, Y. Kubota, K. Kato, M. Takata, et al., *Chem. Commun.* **2015**, *51*, 12463–12466.

[127] N. C. Burtch, H. Jasuja, K. S. Walton, *Chem. Rev.* **2014**, *114*, 10575–10612.

[128] J. E. Mondloch, W. Bury, D. Fairen-Jimenez, S. Kwon, E. J. Demarco, M. H. Weston, A. A. Sarjeant, S. T. Nguyen, P. C. Stair, R. Q. Snurr, et al., *J. Am. Chem. Soc.* **2013**, *135*, 10294–10297.

[129] D. Feng, Z. Y. Gu, J. R. Li, H. L. Jiang, Z. Wei, H. C. Zhou, *Angew. Chem. Int. Ed.* **2012**, *51*, 10307–10310.

[130] J. B. Decoste, G. W. Peterson, H. Jasuja, T. G. Glover, Y. G. Huang, K. S. Walton, *J. Mater. Chem. A* **2013**, *1*, 5642–5650.

[131] A. D. Wiersum, E. Soubeyrand-Lenoir, Q. Yang, B. Moulin, V. Guillerm, M. Ben Yahia, S. Bourrelly, A. Vimont, S. Miller, C. Vagner, et al., *Chem. - An Asian J.* **2011**, *6*, 3270–3280.

[132] F. Y. Yi, D. Chen, M. K. Wu, L. Han, H. L. Jiang, *ChemPlusChem* **2016**, *81*, 675–690.

[133] I. Stassen, B. Bueken, H. Reinsch, J. F. M. Oudenhoven, D. Wouters, J. Hajek, V. Van Speybroeck, N. Stock, P. M. Vereecken, R. Van Schaijk, et al., *Chem. Sci.* **2016**, *7*, 5827–5832.

[134] J. Hou, Y. Luan, J. Tang, A. M. Wensley, M. Yang, Y. Lu, *J. Mol. Catal. A Chem.* **2015**, *407*, 53–59.

[135] S. Tai, W. Zhang, J. Zhang, G. Luo, Y. Jia, M. Deng, Y. Ling, *Microporous Mesoporous Mater.* **2016**, *220*, 148–154.

[136] N. R. Council, *Catalysis Looks to the Future*, National Academies Press, Washington, D.C., **1992**.

[137] A. U. Czaja, N. Trukhan, U. Müller, *Chem. Soc. Rev.* **2009**, *38*, 1284–1293.

[138] P. Silva, S. M. F. Vilela, J. P. C. Tomé, F. A. Almeida Paz, *Chem. Soc. Rev.* **2015**, *44*, 6774–6803.

[139] S. Hasegawa, S. Horike, R. Matsuda, S. Furukawa, K. Mochizuki, Y. Kinoshita, S. Kitagawa, *J. Am. Chem. Soc.* **2007**, *129*, 2607–2614.

[140] B. Yuan, Y. Pan, Y. Li, B. Yin, H. Jiang, *Angew. Chem. Int. Ed.* **2010**, *49*, 4054–4058.

[141] S. M. F. Vilela, A. D. G. Firmino, R. F. Mendes, J. A. Fernandes, D. Ananias, A. A. Valente, H. Ott, L. D. Carlos, J. Rocha, J. P. C. Tomé, et al., *Chem. Commun.* **2013**, *49*, 6400–6402.

[142] A. Aijaz, A. Karkamkar, Y. J. Choi, N. Tsumori, E. Rönnebro, T. Autrey, H. Shioyama, Q. Xu, *J. Am. Chem. Soc.* **2012**, *134*, 13926–13929.

[143] S. Lin, C. S. Diercks, Y. B. Zhang, N. Kornienko, E. M. Nichols, Y. Zhao, A. R. Paris, D. Kim, P. Yang, O. M. Yaghi, et al., *Science* **2015**, *349*, 1208–1213.

[144] M. A. Nasalevich, R. Becker, E. V. Ramos-Fernandez, S. Castellanos, S. L. Veber, M. V. Fedin, F. Kapteijn, J. N. H. Reek, J. I. Van Der Vlugt, J. Gascon, *Energy Environ. Sci.* **2015**, *8*, 364–375.

[145] Y. Yang, H. F. Yao, F. G. Xi, E. Q. Gao, *J. Mol. Catal. A Chem.* **2014**, *390*, 198–205.

[146] G. Calleja, R. Sanz, G. Orcajo, D. Briones, P. Leo, F. Martínez, *Catal. Today* **2014**, *227*, 130–137.

[147] Y. Peng, V. Krungleviciute, I. Eryazici, J. T. Hupp, O. K. Farha, T. Yildirim, *J. Am. Chem. Soc.* **2013**, *135*, 11887–11894.

[148] G. Li, H. Kobayashi, J. M. Taylor, R. Ikeda, Y. Kubota, K. Kato, M. Takata, T. Yamamoto, S. Toh, S. Matsumura, et al., *Nat. Mater.* **2014**, *13*, 802–806.

[149] J. Ren, H. W. Langmi, N. M. Musyoka, M. Mathe, X. Kang, S. Liao, *Mater. Today Proc.* **2015**, *2*, 3964–3972.

[150] R. B. Lin, S. Xiang, H. Xing, W. Zhou, B. Chen, *Coord. Chem. Rev.* **2019**, *378*, 87–103.

[151] N. Wang, A. Mundstock, Y. Liu, A. Huang, J. Caro, *Chem. Eng. Sci.* **2015**, *124*, 27–36.

[152] S. Friebe, A. Mundstock, K. Volgmann, J. Caro, *ACS Appl. Mater. Interfaces* **2017**, *9*, 41553–41558.

[153] S. Friebe, B. Geppert, F. Steinbach, J. Caro, *ACS Appl. Mater. Interfaces* **2017**, *9*, 12878–12885.

[154] Y. Lin, C. Kong, L. Chen, *RSC Adv.* **2016**, *6*, 32598–32614.

[155] X. Zhao, Y. Wang, D. S. Li, X. Bu, P. Feng, *Adv. Mater.* **2018**, *30*, 1–34.

[156] C. Wang, X. Liu, N. Keser Demir, J. P. Chen, K. Li, *Chem. Soc. Rev.* **2016**, *45*, 5107–5134.

[157] R. M. Cuéllar-Franca, A. Azapagic, *J. CO_2 Util.* **2015**, *9*, 82–102.

[158] C. Pollock, *J. Avian Med. Surg.* **2016**, *30*, 386–391.

[159] W.-T. Koo, J.-S. Jang, I.-D. Kim, *Chem* **2019**, *5*, 1938–1963.

[160] X. Fang, B. Zong, S. Mao, *Nano-Micro Lett.* **2018**, *10*, 64.

[161] A. Amini, S. Kazemi, V. Safarifard, *Polyhedron* **2019**, 114260.

[162] G. Lu, J. T. Hupp, *J. Am. Chem. Soc.* **2010**, *132*, 7832–7833.

[163] R. Ameloot, L. Stappers, J. Fransaer, L. Alaerts, B. F. Sels, D. E. De Vos, *Chem. Mater.* **2009**, *21*, 2580–2582.

[164] S. Sachdeva, S. J. H. Koper, A. Sabetghadam, D. Soccol, D. J. Gravesteijn, F. Kapteijn, E. J. R. Sudhölter, J. Gascon, L. C. P. M. De Smet, *ACS Appl. Mater. Interfaces* **2017**, *9*, 24926–24935.

[165] A. Chidambaram, K. C. Stylianou, *Inorg. Chem. Front.* **2018**, *5*, 979–998.

[166] M. Schulz, A. Gehl, J. Schlenkrich, H. A. Schulze, S. Zimmermann, A. Schaate, *Angew. Chem. Int. Ed.* **2018**, *57*, 12961–12965.

[167] P. Kumar, A. Deep, K. H. Kim, *TrAC - Trends Anal. Chem.* **2015**, *73*, 39–53.

[168] N. Notman, *Chem. World* **2017**, *14*, 44–47.

[169] T. Faust, *Nat. Chem.* **2016**, *8*, 990–991.

[170] J. Caro, *Chem. Ing. Tech.* **2018**, *90*, 1759–1768.

[171] A. M. Diskin, P. Španěl, D. Smith, *Physiol. Meas.* **2003**, *24*, 107–119.

[172] W.-T. Koo, J.-S. Jang, S.-J. Choi, H.-J. Cho, I.-D. Kim, *ACS Appl. Mater. Interfaces* **2017**, *9*, 18069–18077.

[173] M. K. Smith, K. E. Jensen, P. A. Pivak, *Chem. Mater.* **2016**, *28*, 5264–5268.

6 MOF-74

6.1 Preface

Within the following chapters two publications, evaluating Co-MOF-74 as a potential candidate for gas-sensing applications, are presented. Various open metal-site-MOF sensors have been successfully used to sense solvent vapours, but were unable to sense pure gaseous analytes.

The first publication (Chapter 6.2) presented is concerned with the general investigations of the adsorption of guest molecules within the 1D anisotropic pores of Co-MOF-74. Therefore, the gases CO_2, propene, propane and argon, as well as methanol and H_2O vapours were used as surrounding test atmospheres. Via Vis/NIR measurements, which were performed with the supporting help of Dominik Hinrichs and Rasmus Himstedt, the interactions of Co-MOF-74 with the applied atmospheres could be proved by shifts of the absorption bands, displayed by a colour change of the MOF. Here, the help of Dirk Dorfs during the interpretation process of the data is appreciated. Furthermore, Raman investigations of Co-MOF-74 under vacuum, argon and H_2O confirmed the interactions of guest molecules with the open metal-sites, indicated by guest molecule dependent peak shifts. Alexander Knebel took a supportive role during the interpretation of the Raman results. In addition to that, the first publication features optical microscopy measurements, which were performed with the supporting help of Carsten Reinhardt, who also wrote the concerning part of the manuscript. These measurements show a clear colour change of the crystal from yellow to red when the polarization plane is rotated, generated by the d-d transition of the Co^{II} ions.

Based on these general investigations of the interactions of Co-MOF-74 and guest species, the second publication (Chapter 6.3) presents the implementation of a Co-MOF-74 composite into a home-build capacitor. Therefore, Co-MOF-74 was doped with different organic semiconducting materials, which resulted in composites with enhanced conductivity compared to the pure MOF. Marvin Treger infiltrated powder samples with different organic semiconductors and evaluated the resulting materials regarding their conductivity enhancements. It was shown, via electrical conductivity measurements, that Co-MOF-74 infiltrated with tetrathiafulvalene (TTF) possesses a higher conductivity, compared to the 7,7,8,8-tetracyanoquinodimethane (TCNQ) containing Co-MOF-74 composite material. Here, the supporting help of Karsten Lange during the analysis of the data is appreciated. In order to prove the successful infiltration of TTF into the pores of Co-MOF-74, Pascal Rush performed and interpreted thermogravimetric analysis measurements, while Hidetsugu Shiozawa performed and interpreted XPS measurements as well as played a supportive role during the Raman measurements. IR microscopic images and spectra of

the CO_2 adsorption on an empty Co-MOF-74 compared to a TTF infiltrated Co-MOF-74, also confirming the successful infiltration of the crystal with TTF, were performed with the help of Seungtaik Hwang. Christian Chmelik, Nadja C. Bigall and Thomas Pichler refined the manuscript. Alexander Mundstock took a supportive role during the conceptualization process of both manuscripts by supporting the measurements with his expertise of Co-MOF-74, helping with the construction of various suitable measurement cells as well as first proofreading the drafts and supporting the design of the cover pictures. Jürgen Caro ensured the high quality of the publications by guiding the whole process with his extensive expertise concerning the field of MOFs, as well as the refining the manuscripts.

All not-mentioned tasks within the development of the manuscripts, such as the synthesis, characterization, interpretation and investigation of the materials as well as the construction of measurement cells and the authoring of the manuscripts were performed by the author of this thesis.

6.2 The Interaction of guest molecules with Co-MOF-74: A Vis/NIR and Raman approach

I. Strauss, A. Mundstock, D. Hinrichs, R. Himstedt, A. Knebel, C. Reinhardt, D. Dorfs,
J. Caro

The Interaction of Guest Molecules with Co-MOF-74: A Vis/NIR and Raman Approach

Ina Strauss,* Alexander Mundstock, Dominik Hinrichs, Rasmus Himstedt, Alexander Knebel, Carsten Reinhardt, Dirk Dorfs, and Jürgen Caro*

Angewandte Chemie
International Edition

GDCh

Communications

Angewandte
International Edition Chemie
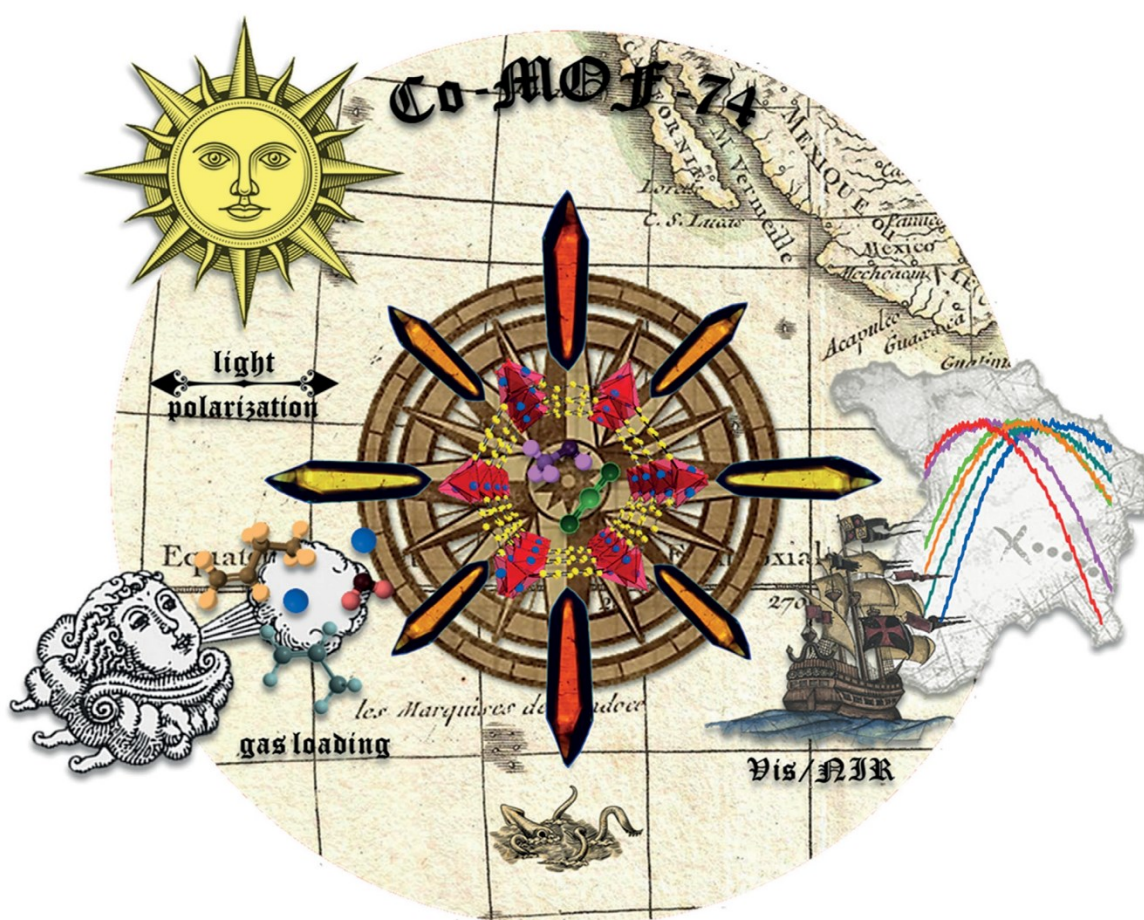
Abstract: *Co-MOF-74 rod like crystals with a length of several hundred micrometers are synthesized by a solvothermal procedure and their interaction with different gases is evaluated for selective gas sensing. We show strongly anisotropic absorption behavior of the Co-MOF-74 crystals when illuminated with polarized light. The interactions of guests (CO_2, propane, propene, Ar, MeOH, H_2O) with Co-MOF-74, is studied by various spectroscopic techniques. Vis/NIR shows peak shifts of Co-MOF-74 depending on the interaction with the guest. In the visible and the NIR the maximum absorbance is shifted selectively corresponding to the intensity of the Co^{II}–guest interaction. Even propene and propane could be distinguished at room temperature by their different interactions with Co-MOF-74. Raman spectroscopy was used to detect a modified vibrational behavior of Co-MOF-74 upon gas adsorption. We show that the adsorption of H_2O leads to a characteristic shift of the peak maxima in the Raman spectra.*

Metal–organic frameworks (MOFs)[1] are inorganic–organic hybrid materials and a class of soft porous, functional materials.[2] They appeal through their wide variety and modularity of suitable metal centers and organic linker molecules, which are combined to a crystalline nanoporous material with tunable pore sizes and functional groups.[3] MOFs have one-, two-, or three-dimensional, uniform pores and the two- and three-dimensional structures can even form a network of channels. Due to their high inner surface area they are perfectly suited for gas storage or separation,[4] CO_2 capture,[5] catalysis,[6] or drug delivery systems.[7] A relatively new approach is their utilization in sensing,[8] which is made possible by their permanent porosity after the removal of solvent molecules and their reversible and specific adsorption of guest molecules.[9] Several groups even explored the use of MOFs for sensing of aromatic and aliphatic high-explosives, such as 2,4,6-trinitrotoluene (TNT) and 1,3,5-trinitroperhydro-1,3,5-triazine (RDX).[10] Furthermore, MOFs can display specific changes in specific characteristics (e.g. in unit cell and pore size,[11] absorption and emission of certain wavelengths,[12] or conductivity[13]) due to external stimuli.

Open-metal-site-MOF sensors have been a field of interest in the past, for example Achmann et al. presented a Fe-BTC (BTC = benzene-1,3,5-tricarboxylic acid)MOF-based sensor which is able to sense H_2O, EtOH, and MeOH vapors, but is unable to detect pure gas-phase analytes, such as CO_2, O_2, NO.[14] Additionally, Long et al. investigated the

influence of various vapors (e.g. acetone, DMF, MeOH) on a Co^{II}-MOF and showed a shift of the optical absorption in the visible region.[15] In our work we are able to show these absorption shifts in the visible region not only for vapors but for gases, such as CO_2 and propane/propene.

We synthesized Co-MOF-74,[16] also known as CPO-27-Co[17] or Co_2(dobdc), which is composed of 2,5-dioxido-1,4-benzenedicarboxylate and Co^{II} as bridging metal ion. Co-MOF-74 possesses a one-dimensional pore structure with a pore size of about 1.1–1.2 nm and a hexagonal honeycomb-like shape.[18] In the past, various groups obtained promising results for M-MOF-74/CPO-27-M (M = Fe, Ni, Mg, Mn, Co, Cu, Zn) in the fields of adsorptive separation, for example, for ethene/ethane[19], propene/propane[19,20] and selective CO_2 adsorption.[6a]

MOF-74 provides responses to NO,[21] CO,[22] C_2H_4,[22] and H_2.[23] Chmelik et al. investigated the effect of humid air on Co-MOF-74 and found a pore blocking in a surface-near shell which can be annealed under MeOH.[24] Following up on this, we study herein the adsorption of various guest molecules into the pores of Co-MOF-74 at room temperature. Via Vis/NIR and Raman spectroscopy, a peak shift depending on the adsorbed gas under study (CO_2, propene, propane, Ar, MeOH, H_2O) could be detected.

The Co-MOF-74 crystals were characterized by X-ray diffraction (data in accordance with literature, see Supporting Information) and SEM. Figure 1 shows the Co-MOF-74 crystal structure.
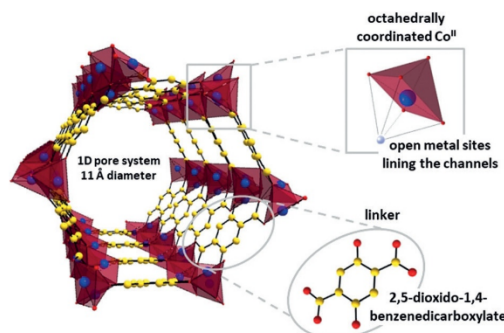
Figure 1. Crystal structure of Co-MOF-74, octahedrally coordinated Co^{II} with open metal sites lining the interior of the pore, and the organic linker 2,5-dioxido-1,4-benzenedicarboxylate.

[*] I. Strauss, A. Mundstock, D. Hinrichs, R. Himstedt, A. Knebel, Dr. D. Dorfs, Prof. J. Caro
 Institute for Physical Chemistry and Electrochemistry
 Leibniz University Hannover
 Callinstrasse 3A, 30167 Hannover (Germany)
 E-mail: ina.strauss@pci.uni-hannover.de
  juergen.caro@pci.uni-hannover.de
 Prof. C. Reinhardt
 Laserzentrum Hannover
 Hollerithallee 8, 30419 Hannover (Germany)

 Supporting information and the ORCID identification number(s) for the author(s) of this article can be found under:
 https://doi.org/10.1002/anie.201801966.

The octahedrally coordinated Co^{II} has open metal sites, lining the channels, which are interconnected by the organic linker 2,5-dioxido-1,4-benzenedicarboxylate. The 1D pore system is built up of parallel hexagonal channels with 11 Å diameter.[25]
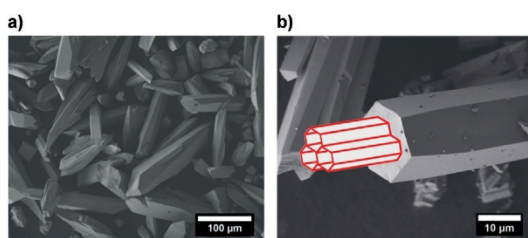
Figure 2 shows SEM images of the Co-MOF-74 crystals. In Figure 2a various Co-MOF-74 rod-like crystals with a length of several hundred micrometers are shown. The crystals have a hexagonal shape with a long axis from 100 μm up to 200 μm and a shorter axis from 20 μm up to 50 μm. As Figure 2b shows, the 1D pores run parallel to the long crystal

Communications

Figure 2. a),b) SEM images of Co-MOF-74 crystals with schematically indicated pores.

axis, as found in transient IR microscopy studies of methanol sorption uptake.[24] For further characterization of the Co-MOF-74 crystals, optical microscopy measurements were performed. Typical absorption spectra (measured with a differently polarized probe beam) of a single Co-MOF-74 crystal are shown in Figure 3.
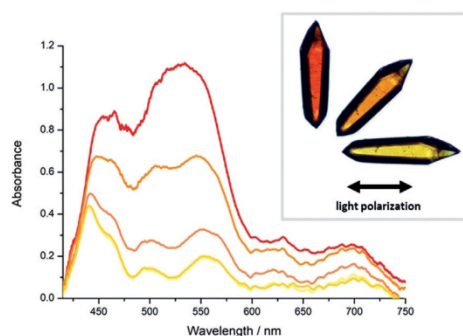
Figure 3. Spectral measurements of Co-MOF-74 with polarized light with a polarization plane gradually turned by $\pi/2$.

The polarization state of the light has been gradually adjusted from 0° to 90° in steps of 22.5° (yellow to red curves in Figure 3). All angles are given with respect to the long crystal axis. A high-power white-light-emitting diode was used as light source. The background spectrum has been measured from the object plane and remains unchanged when the polarizer is rotated. This indicates the independence of the optical transmission of the microscope imaging beam path on the light polarization state. Light absorption of the crystal occurs in the spectral range between 440 nm and 580 nm. Depending on the polarization state, a clear color change of the crystal from yellow to red can be observed. The corresponding camera images are shown as insets in the absorbance graphs (for additional investigation of the blue and green spectral region see Supporting Information, Figure S3). Thus, the absorption behavior of the Co-MOF-74 crystals towards polarized light is well in line with their strongly anisotropic crystals structure (hexagonal R$\bar{3}$, space group No. 148[26]).

We assign the transition in the spectral range from 500 nm to 600 nm to a d–d transition of the Co^{II} ions. This transition

shows a strong dependence on the polarization of the incident light (Figure 3). This strong dependence can be explained in that the transition dipole moment of this transition is aligned perpendicular to the rod's c-axis because of the unoccupied coordination sites of the Co^{II} ions. When the incident light is polarized in the same direction as the direction of the transition dipole moment, the absorption cross section of this transition is maximized and in turn the absorption cross section is minimized when the polarization of the light is aligned perpendicular to the transition dipole moment. A similar effect of optical anisotropy of light absorption was observed on crystals of the molecular sieve CoAPO-5 (structure type AFI) and explained by Döring et al.[27]

To evaluate the sensory performance of the Co-MOF-74 for gas sensing, absorption spectra of powder samples have been measured at room temperature. The Vis/NIR-absorption spectra of Co-MOF-74 are given in Figure 4. The spectra have been measured in reflection mode using an integrating sphere. This way, all light losses resulting from scattering are eliminated and only absorption effects are measured.

Three main absorption bands of Co-MOF-74 can be identified. The spectra were normalized on the maximum around 1200 nm which can be assigned to the spin allowed d–d transition of cobalt and is typical for an octahedral Co^{II} complex.[28] The second absorption band around 600 nm also corresponds to the d–d transition of an octahedral Co^{II} complex (see Supporting Information).[28] The last main absorption band at around 430 nm is assigned to the n–π* transition of the organic linker (see Supporting Information). Depending on the type of guest molecule in the pores of the MOF, both the band around 600 nm as well as the band around 1200 nm show a significant shift of their maxima position when compared to the Co-MOF-74 loaded with Ar as a reference. The position of the NIR band of the MOF loaded with Ar as guest with the presumably weakest interaction is located at 1295 nm (see Table 1). The adsorption of stronger interacting guest molecules causes distortion of the coordination polyhedra of Co-MOF-74, including changes in symmetry and ligand field, comparable to the results Bonino et al. reported for Ni-MOF-74.[21] H$_2$O as a guest molecule does not only cause a distortion of the coordination polyhedra but leads to a change in the oxidation state of cobalt.[21] When the interaction of the Co^{II}-center and the guest molecule becomes stronger compared to Ar, the NIR absorption band is shifted hypsochromically.

The weakest interaction compared to Ar could be seen for propane since it does not possess any functionality. However, a shift of the NIR absorption band from 1295 nm to 1275 nm could be demonstrated for propene, which can be explained by the interaction of Co^{II} with the double bond of propene. An even stronger shift can be observed for the interaction of Co-MOF-74 with CO$_2$ for which the maximum of the peak in the NIR-area can be found at 1262 nm. CO$_2$ binds with an oxygen to the metal center as shown schematically in Figure 4b.[29] However, the interaction with CO$_2$ is weak compared to the interaction with MeOH and steam. The Vis/NIR spectra indicate the strongest interaction between H$_2$O and Co-MOF-74 which can be explained by the strong interaction of the metal center with the oxygen atom of

Communications
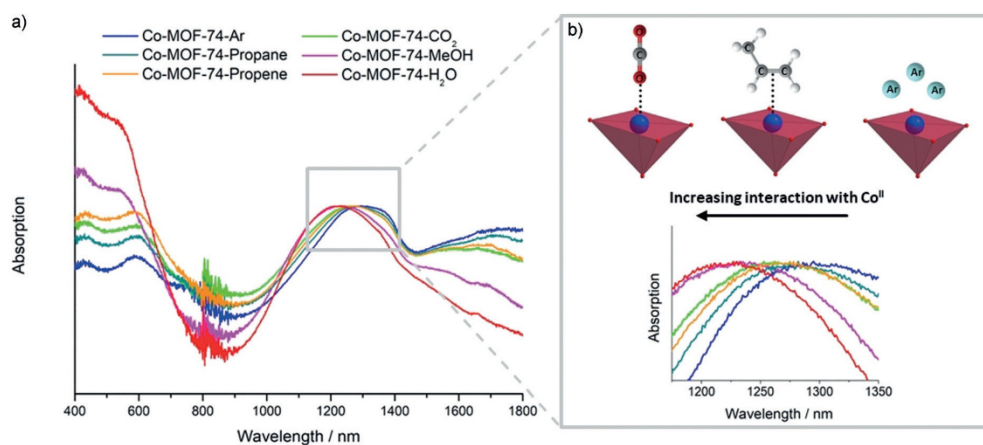
Figure 4. a) Normalized Vis/NIR-absorption spectra of Co-MOF-74 at room temperature depending on the interaction with various guest molecules. b) The shift of the maximum position of the NIR band. The high noise level around 800 nm is due to a change of the detector from Vis to NIR (with both detectors having a quite high noise level at their respective detection edge).

Table 1: Absorbance maxima of the Vis and NIR regions of the Co-MOF-74 UV/Vis-spectra depending on the guest molecules and their interaction.

Guest molecule	Maximum [nm] (Vis)	Maximum [nm] (NIR)	Interaction
Ar	585	1295	/
CO_2	593	1262	Me—O interaction
Propene	595	1275	π-backbonding
Propane	586	1282	Low-interaction/ no interaction
MeOH	520 (shoulder)	1233	Me—O interaction and hydrogen bonding
H_2O	525 (shoulder)	1227	Me—O interaction and hydrogen bonding

H_2O and the additional hydrogen-bonding interaction of the hydrogen molecules with the oxygen sites of the organic ligand. For MeOH a quite similar interaction can be found, since the metal center of Co-MOF-74 is also interacting with the oxygen of MeOH and the hydrogen is able to form hydrogen bonds.

In the Vis region, relative to Ar, the absorption band is strongly altered mainly in the presence of OH groups and thus in the presence of H_2O or MeOH. For propane, propene, and CO_2, the maximum of the absorption band is shifted only negligibly, while for MeOH and H_2O a significant hypsochromic shift is observed. In case of H_2O adsorption, its oxygen atom interacts with an open metal coordination site, thus weakening the bond between one hydrogen atom and the oxygen atom.[30]

This effect, in combination with the intermolecular hydrogen bonds between H_2O and the oxygen atoms of the organic linker, causes a charge density redistribution,[30] which results in the hypsochromic shift. We observed a comparable charge density redistribution for the interaction between MeOH and Co-MOF-74. The vibrational modes of Co-MOF-74 were investigated under the influence of different gas atmospheres by Raman spectroscopy. All spectra were recorded at room temperature and normalized for better comparability.
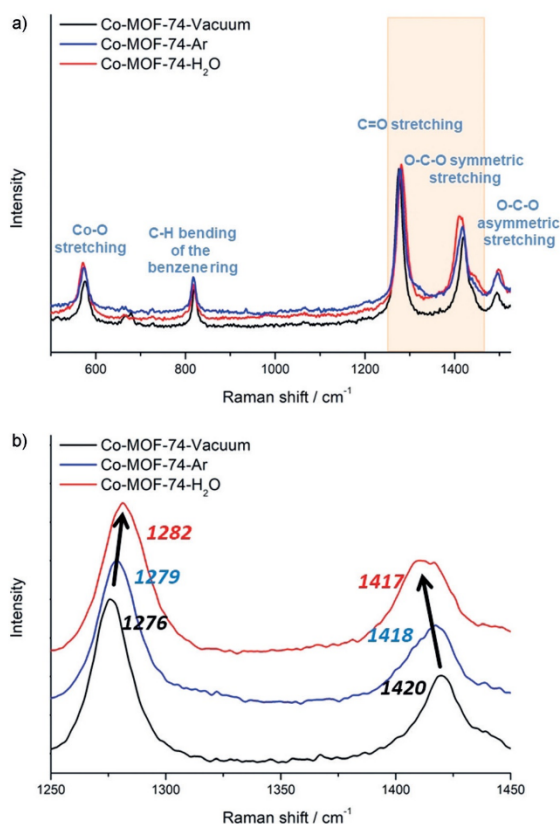
Figure 5a shows the Raman spectra of Co-MOF-74 under vacuum, Ar, and H_2O. Depending on the guest molecules, all peaks undergo a shift. The peaks of Co-MOF-74 at 576 cm^{-1} (vacuum), 573 cm^{-1} (Ar), and 571 cm^{-1} (H_2O) correspond to the Co—O stretching modes. The C—H bending of the benzene ring is represented by the signals at 820 cm^{-1} (vacuum), 818 cm^{-1} (Ar), and 817 cm^{-1} (H_2O). At 1494 cm^{-1} (vacuum), 1496 cm^{-1} (Ar), and 1498 cm^{-1} (H_2O) the peak corresponds to the O—C—O symmetric stretching of the carboxylate group of the organic linker.

A close look in Figure 5b in the region 1250 cm^{-1} to 1450 cm^{-1} reveals that both peaks shift in opposite directions. For the C=O stretching, the maximum of the peak shifts from 1276 cm^{-1} (vacuum) and 1279 cm^{-1} (Ar) to 1282 cm^{-1} (H_2O). In contrast, the O—C—O symmetric stretching peak maxima shifts from 1498 cm^{-1} (H_2O) to 1496 cm^{-1} (Ar) and 1494 cm^{-1} (vacuum). The part of the asymmetric O—C—O stretching mode increases with an increasing amount of H_2O, owing to the hydrogen bonding between one oxygen atom of the MOF and the adsorbed H_2O molecule. At the same time, the C=O stretching becomes more energetic.

It can be seen that besides the characteristic modes of Co-MOF-74, changes of the Raman shift can also be observed depending on the gas atmospheres and are in good agreement with the results of the Vis/NIR investigations for the adsorption of H_2O. By annealing the Co-MOF-74 crystals after water exposition in MeOH atmosphere and subsequent activation, the peak shifts in Raman spectra could be reversed.[24]

Figure 5. a) Raman spectra of Co-MOF-74 at room temperature under vacuum (black), Ar (blue), and H₂O (red). b) Expansion showing the peak shift depending on the guest molecule in Co-MOF-74.

results significantly expand the usage of MOFs for optical-based gas-sensing applications.

Conflict of interest

The authors declare no conflict of interest.

In conclusion, we were able to demonstrate the strongly anisotropic absorption behavior of Co-MOF-74 crystals illuminated by polarized light. Afterwards Co-MOF-74 has been evaluated for selective gas sensing. Several gases (CO_2, propene, propane, Ar, MeOH, H_2O) can be detected and distinguished by Co-MOF-74 through their interactions with the Co^{II} centers. We detected different peak shifts in the Vis/NIR spectra which could be correlated with the metal–guest interaction. Guests, such as propene, CO_2, MeOH, and H_2O, show a stronger interaction with the Co^{II} metal centers than propane and Ar. In case of propene, an interaction of the Co^{II} with the double bond is assumed, for CO_2 one oxygen atom is interacting with the metal center, and in case of MeOH and H_2O the molecules interact via their oxygen atom and can additionally develop hydrogen bonding between the hydrogen atoms of H_2O or MeOH and the oxygen atoms of the organic linker. Furthermore, Raman investigations showed a change in the vibrational modes of Co-MOF-74 depending on the adsorbed molecules. Water adsorption leads to peak shifts in the Raman spectra, which are in good agreement with our results from the Vis/NIR investigations. Overall, our

[1] J. L. C. Rowsell, O. M. Yaghi, *Microporous Mesoporous Mater.* **2004**, *73*, 3–14.

[2] H. Furukawa, K. E. Cordova, M. O. Keeffe, O. M. Yaghi, *Science* **2013**, *341*, 1230444.

[3] Y. Cui, B. Li, H. He, W. Zhou, B. Chen, G. Qian, *Acc. Chem. Res.* **2016**, *49*, 483–493.

[4] a) S. Friebe, B. Geppert, F. Steinbach, J. Caro, *ACS Appl. Mater. Interfaces* **2017**, *9*, 12878–12885; b) S. Friebe, A. Mundstock, K. Volgmann, J. Caro, *ACS Appl. Mater. Interfaces* **2017**, *9*, 41553–41558.

[5] Y. Belmabkhout, V. Guillerm, M. Eddaoudi, *Chem. Eng. J.* **2016**, *296*, 386–397.

[6] a) H. Cho, D. Yang, J. Kim, S. Jeong, W. Ahn, *Catal. Today* **2012**, *185*, 35–40; b) D. Ruano, M. Díaz-García, A. Alfayate, M. Sanchez-Sanchez, *ChemCatChem* **2015**, *7*, 674–681; c) H. Jiang, Q. Wang, H. Wang, Y. Chen, M. Zhang, *ACS Appl. Mater. Interfaces* **2016**, *8*, 26817–26826.

[7] a) P. Horcajada, T. Chalati, C. Serre, B. Gillet, C. Sebrie, T. Baati, J. F. Eubank, D. Heurtaux, P. Clayette, C. Kreuz, et al., *Nat. Mater.* **2010**, *9*, 172–178; b) S. Rojas, T. Devic, P. Horcajada, *J. Mater. Chem. B* **2017**, *5*, 2560–2573; c) T. Hidalgo, M. Giménez-Marqués, E. Bellido, J. Avila, M. C. Asensio, F. Salles, M. V. Lozano, M. Guillevic, R. Simón-Vázquez, A. González-Fernández, et al., *Sci. Rep.* **2017**, *7*, 43099.

[8] a) L. Heinke, M. Tu, S. Wannapaiboon, R. A. Fischer, C. Wöll, *Microporous Mesoporous Mater.* **2015**, *216*, 200–215; b) G. Lu, J. T. Hupp, *J. Am. Chem. Soc.* **2010**, *132*, 7832–7833.

[9] E. D. Bloch, W. L. Queen, M. R. Hudson, J. A. Mason, D. J. Xiao, L. J. Murray, R. Flacau, C. M. Brown, J. R. Long, *Angew. Chem. Int. Ed.* **2016**, *55*, 8605–8609; *Angew. Chem.* **2016**, *128*, 8747–8751.

[10] a) Z. Hu, S. Pramanik, K. Tan, C. Zheng, W. Liu, X. Zhang, Y. J. Chabal, J. Li, *Cryst. Growth Des.* **2013**, *13*, 4204–4207; b) S. S. Nagarkar, B. Joarder, A. K. Chaudhari, S. Mukherjee, S. K. Ghosh, *Angew. Chem. Int. Ed.* **2013**, *52*, 2881–2885; *Angew. Chem.* **2013**, *125*, 2953–2957.

[11] a) T. Loiseau, C. Serre, C. Huguenard, G. Fink, F. Taulelle, M. Henry, T. Bataille, G. Férey, *Chem. Eur. J.* **2004**, *10*, 1373–1382; b) A. J. Fletcher, K. M. Thomas, M. J. Rosseinsky, *J. Solid State Chem.* **2005**, *178*, 2491–2510.

Communications

[12] Y. Takashima, V. M. Martínez, S. Furukawa, M. Kondo, S. Shimomura, H. Uehara, M. Nakahama, K. Sugimoto, S. Kitagawa, *Nat. Commun.* **2011**, *2*, 168.

[13] a) M. G. Campbell, S. F. Liu, T. M. Swager, M. Dincă, *J. Am. Chem. Soc.* **2015**, *137*, 13780–13783; b) C. A. Fernandez, P. C. Martin, T. Schaef, M. E. Bowden, P. K. Thallapally, L. Dang, W. Xu, X. Chen, B. P. McGrail, *Sci. Rep.* **2014**, *4*, 6114.

[14] S. Achmann, G. Hagen, J. Kita, I. M. Malkowsky, C. Kiener, R. Moos, *Sensors* **2009**, *9*, 1574–1589.

[15] Z.-Z. Lu, R. Zhang, Y.-Z. Li, Z.-J. Guo, H.-G. Zheng, *J. Am. Chem. Soc.* **2011**, *133*, 4172–4174.

[16] N. L. Rosi, J. Kim, M. Eddaoudi, B. Chen, M. O'Keefee, O. M. Yaghi, *J. Am. Chem. Soc.* **2005**, *127*, 1504–1518.

[17] P. D. C. Dietzel, P. A. Georgiev, J. Eckert, R. Blom, T. Strässle, T. Unruh, *Chem. Commun.* **2010**, *46*, 4962–4964.

[18] P. D. C. Dietzel, V. Besikiotis, R. Blom, *J. Mater. Chem.* **2009**, *19*, 7362–7370.

[19] a) U. Böhme, B. Barth, C. Paula, A. Kuhnt, W. Schwieger, A. Mundstock, J. Caro, M. Hartmann, *Langmuir* **2013**, *29*, 8592–8600; b) A. Luna-Triguero, J. M. Vincent-Luna, T. M. Becker, T. J. H. Vlugt, D. Dubbeldam, P. Go, *ChemistrySelect* **2017**, *2*, 665–672.

[20] Y. Bae, C. Y. Lee, K. C. Kim, O. K. Farha, P. Nickias, J. T. Hupp, S. T. Nguyen, R. Q. Snurr, *Angew. Chem. Int. Ed.* **2012**, *51*, 1857–1860; *Angew. Chem.* **2012**, *124*, 1893–1896.

[21] F. Bonino, C. Lamberti, P. D. C. Dietzel, C. Prestipino, S. Bordiga, *Chem. Mater.* **2008**, *20*, 4957–4968.

[22] S. Chavan, F. Bonino, J. G. Vitillo, E. Groppo, C. Lamberti, P. D. C. Dietzel, S. Bordiga, *Phys. Chem. Chem. Phys.* **2009**, *11*, 9811–9822.

[23] T. Pham, K. A. Forrest, R. Banerjee, G. Orcajo, J. Eckert, B. Space, *J. Phys. Chem. C* **2015**, *119*, 1078–1090.

[24] C. Chmelik, A. Mundstock, P. D. C. Dietzel, J. Caro, *Microporous Mesoporous Mater.* **2014**, *183*, 117–123.

[25] L. Valenzano, B. Civalleri, S. Chavan, G. T. Palomino, C. O. Area, S. Bordiga, *J. Phys. Chem. C* **2010**, *114*, 11185–11191.

[26] W. Wong-Ng, J. A. Kaduk, H. Wu, M. Suchomel, *Powder Diffr.* **2012**, *27*, 256–262.

[27] I. Girnus, K. Hoffmann, F. Marlow, J. Caro, G. Döring, *Microporous Mater.* **1994**, *2*, 537–541.

[28] N. P. Magwa, E. Hosten, G. M. Watkins, Z. R. Tshentu, *Int. J. Nonferrus Metallurgy* **2012**, *3*, 49–58.

[29] H. Wu, J. M. Simmons, G. Srinivas, W. Zhou, T. Yildirim, *J. Phys. Chem. Lett.* **2010**, *1*, 1946–1951.

[30] K. Tan, S. Zuluaga, Q. Gong, P. Canepa, H. Wang, J. Li, Y. J. Chabal, T. Thonhauser, *Chem. Mater.* **2014**, *26*, 6886–6895.

6.3 Metal-organic framework Co-MOF-74-based host-guest composites for resistive gas sensing

I. Strauss, A. Mundstock, M. Treger, K. Lange, S. Hwang, C. Chmelik, P. Rusch,

N. C. Bigall, T. Pichler, H. Shiozawa, J. Caro

Metal−Organic Framework Co-MOF-74-Based Host−Guest Composites for Resistive Gas Sensing

Ina Strauss,*,[†] Alexander Mundstock,[†] Marvin Treger,[†] Karsten Lange,[†] Seungtaik Hwang,[‡] Christian Chmelik,[‡] Pascal Rusch,[†] Nadja C. Bigall,[†,§] Thomas Pichler,[∥] Hidetsugu Shiozawa,[∥,⊥] and Jürgen Caro*,[†]

[†]Institute of Physical Chemistry and Electrochemistry, Leibniz Universität Hannover, Callinstraße 3A, D-30167 Hanover, Germany

[‡]Faculty of Physics and Earth Sciences, Universität Leipzig, Linnéstraße 5, D-04103 Leipzig, Germany

[§]Laboratory for Nano and Quantum Engineering, Leibniz University Hannover, Schneiderberg 39, D-30167 Hanover, Germany

[∥]Faculty of Physics, University of Vienna, Boltzmanngasse 5, A-1090 Vienna, Austria

[⊥]J. Heyrovsky Institute of Physical Chemistry, Czech Academy of Sciences, Dolejskova 3, CZ-18223 Prague 8, Czech Republic

Ⓢ *Supporting Information*

ABSTRACT: Increasing demands in the field of sensing, especially for gas detection applications, require new approaches to chemical sensors. Metal−organic frameworks (MOFs) can play a decisive role owing to their outstanding performances regarding gas selectivity and sensitivity. The tetrathiafulvalene (TTF)-infiltrated MOF, Co-MOF-74, has been prepared following the host−guest concept and evaluated in resistive gas sensing. The Co-MOF-74-TTF crystal morphology has been characterized via X-ray diffraction and scanning electron microscopy, while the successful incorporation of TTF into the MOF has been validated via X-ray photoemission spectroscopy, thermogravimetric analysis, UV/vis, infrared (IR), and Raman investigations. We demonstrate a reduced yet ample uptake of CO_2 in the pores of the new material by IR imaging and adsorption isotherms. The nanocomposite Co-MOF-74-TTF exhibits an increased electrical conductivity in comparison to Co-MOF-74 which can be influenced by gas adsorption from a surrounding atmosphere. This effect could be used for gas sensing.

KEYWORDS: *infiltration of MOFs, Guest@MOF, conducting MOFs, gas sensing, tetrathiafulvalene*
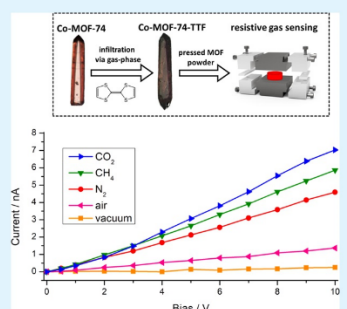
■ INTRODUCTION

Metal−organic frameworks (MOFs) are a class of crystalline and porous organic−inorganic hybrid materials.[1,2] A MOF consists of metal ions or metal-oxide clusters as inorganic building units which are connected by organic ligands acting as linkers. The intrinsic porosity of the framework qualifies MOFs for applications like catalysis, drug-delivery systems, gas separation, storage, or sensing.[3−8]

The use of MOFs for the latter has recently gathered increasing attention.[3−9] New chemical sensors are needed for various controlling systems or devices including smart network-connected medical devices or automated industrial process monitoring systems.[10] Today, metal oxides are widely used in chemical sensors leading to problems like atypical operation temperature above 200 °C to promote surface reactions, cross selectivity, and baseline drifts because of aging effects.[11] The use of MOFs for sensing applications could solve those problems by taking advantage of their selective gas adsorption at room temperature.[5,8] There are several concepts for MOF-based gas sensors like colorimetric or resistive sensing applications.[12−15] Here, resistive sensor devices have the advantages that they enable the use of MOF powders in the form of tablets, making them simple to construct and produce.[9,16] The major bottle neck for the construction of MOF-based resistive gas sensors is the development of electrically conductive or semiconductive MOFs.[17−22] In 2014, Allendorf and co-workers published an electrically conductive MOF based on HKUST-1 doped with the organic semiconductor 7,7,8,8-tetracyanoquinodimethane (TCNQ).[23−25] This was the first conductive MOF following the Guest@MOF concept which is based on the idea that the combination of MOFs and guest molecules can promote new materials with new properties.[25,26] This concept led to the development of conductive composite materials based on MOFs infiltrated with organic semiconductors.[27−29]
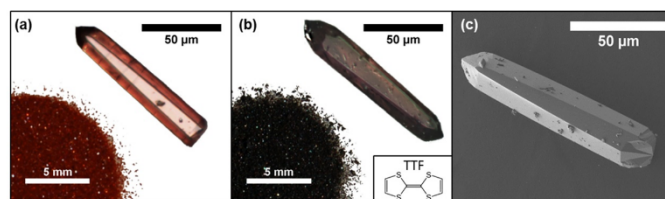
Co-MOF-74, also known as CPO-27-Co or $Co_2(dobdc)$, contains Co^{II} as metal ions connected through 2,5-dioxido-1,4-benzenedicarboxylate as organic ligands. This MOF-74 possesses a one-dimensional pore system with a pore diameter of 1.1−1.2 nm.[30,31]

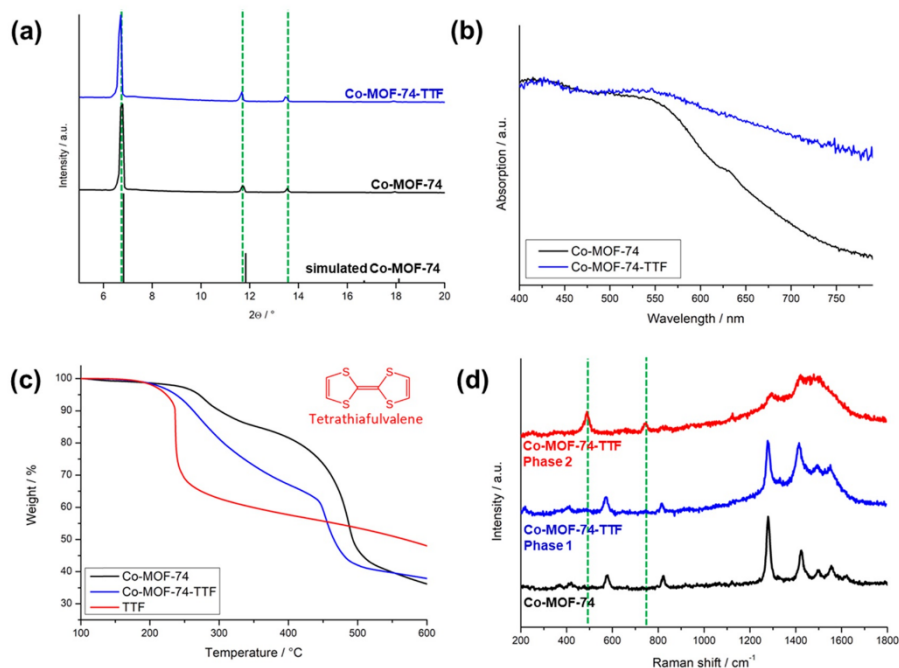**Figure 1.** Optical microscopy images of powder and single crystals of Co-MOF-74 (a) as well as Co-MOF-74-TTF (b) and the SEM image of Co-MOF-74-TTF (c).

Figure 2. (a) XRD data of Co-MOF-74 and Co-MOF-74-TTF compared to the simulated Co-MOF-74 pattern. (b) UV/vis-spectra of Co-MOF-74 compared to Co-MOF-74 infiltrated with TTF. (c) Normalized TGA measurements of Co-MOF-74, Co-MOF-74-TTF, and TTF under the N_2 atmosphere. (d) Spatially resolved Raman spectra of Co-MOF-74 showing two different Co-MOF-74-TTF phases at room temperature under vacuum.

In our previous work, we showed that Co-MOF-74, with its hexagonal honeycomb-like lattice and open metal sites, is a potential material for gas sensing.[32]

Here, we present a novel Co-MOF-74-based composite material for gas sensing applications. Following the Guest@MOF concept, we infiltrated Co-MOF-74 powder with the organic semiconductor tetrathiafulvalene (TTF).[33] Subsequently, resistive gas sensing experiments with pressed tablets were performed.

■ EXPERIMENTAL SECTION

Materials. All chemicals were received from commercial vendors and used without further purification. For the following synthesis, cobalt nitrate hexahydrate ($Co(NO_3)_2 \cdot 6H_2O$, 99%, Sigma-Aldrich), 2,5-dihydroxy-terephthalic acid (DHBDC, 98%, Sigma-Aldrich), N,N-dimethylformamide (DMF, ≥99.8%, Sigma-Aldrich), ethanol (EtOH, ≥99.8%, Sigma-Aldrich), methanol (MeOH, ≥99.8%, Sigma-Aldrich), TCNQ (>98%, TCI), TTF (>98%, TCI), and water (H_2O, Millipore) were used.

Preparation of Co-MOF-74 Powders. The MOF-74 powders were prepared according to a slightly modified procedure previously published by Chmelik et al.[34] All MOF-74 syntheses were performed in 60 mL Teflon-lined autoclaves (Parr Germany). The metal salt (0.713 g, 2.45 mmol $Co(NO_3)_2 \cdot 6H_2O$) was dissolved in a mixture of DMF, EtOH, and H_2O (60 mL, v/v/v, 1/1/1) and DHBDC (0.145 g, 0.73 mmol) was added. The resulting suspension was ultrasonicated until the solution turns clear and heated for 24 h at 121 °C. After cooling down to room temperature, the precipitate was obtained by centrifugation and washed/solvent-exchanged with MeOH three times. The received solid was dried under reduced pressure and activated under vacuum at 160 °C for 4 h.

Loading of the MOF. The MOF powders were infiltrated with the organic semiconductors TCNQ or TTF via the gas phase by storing them in a previously evacuated flask over the respective organic semiconductor molecules at 70 °C overnight, followed by a stepwise increase of the temperature up to 170 °C within 4 h. Afterward, the resulting solid composites were washed with MeOH, dried under reduced pressure, and activated before gas sensing under vacuum at 160 °C over 4 h.

14176

Research Article

Characterization of the Materials. X-ray diffraction (XRD) (Bruker D8 Advance, Cu $K\alpha_1$ radiation λ = 0.154 nm) and infrared (IR) spectroscopy (Agilent Technologies Cary 630 FTIR) were used to characterize the MOF powders. The crystal morphologies of the materials were analyzed with optical microscopy (Bruker Senterra Raman spectrometer) and scanning electron microscopy (SEM) (JEOL JSM-6700F NT, 2 kV acceleration voltage). UV/vis measurements were performed using a Cary 5000 UV/vis absorption spectrophotometer from Agilent Technologies. Both samples were measured in an integrating sphere (Agilent DRA-2500) in the reflection mode with a home-made quartz glass cuvette. All spectra were normalized to the maximum absorbance peak.

Thermogravimetric measurements were carried out on Mettler-Toledo TGA/DSC 3+ between 40 and 600 °C with a heating rate of 1 °C/min under N_2 flow (50 mL/min).

Spatially resolved Raman spectra were measured with a Horiba Jobin Yvon LabRAM spectrometer equipped with a Coherent Innova 70 ion laser at a wavelength of 514.5 nm (E_{ex} = 2.41 eV).

IR images and IR absorbance spectra under the CO_2 atmosphere were achieved with an IR microscope (Bruker Hyperion 3000) connected to a vacuum Fourier transform IR spectrometer (Bruker Vertex 80v) at room temperature. For the IR images, a focal plane array detector was used consisting of an array of 128 × 128 single detectors with a size of 40 × 40 μm each. By increasing the magnification power of the scanning objective (15 times), a resolution of approximately 2.7 × 2.7 μm was obtained. The transfer of the crystals into an IR optical cell was carried out inside a glove box under an Ar atmosphere in order to prevent air contact. Subsequently, the cell was connected to the static vacuum system consisting of a pumping station (Pfeiffer Vacuum HiCube 80 Classic) and stainless-steel cylindrical gas reservoirs.

CO_2 adsorption isotherms were measured by 3P INSTRUMENTS (Odelzhausen, Germany).

X-ray photoemission spectroscopy (XPS) experiments were performed using a Scienta RS4000 hemispherical analyzer with a monochromatic Al Kα X-ray source (1486.6 eV). Toluene solutions containing the MOF crystals were drop-cast onto a gold substrate. Gold 4f lines were used to calibrate the binding energy.

Conductivity measurements were performed in a three-necked glass flask with a home-built electrode setup under atmospheric pressure of the respective gases. Therefore, 0.1 g of each MOF powder was pressed resulting in 0.1 cm thin tablets which were placed between the electrodes. The measurement cell was evacuated for 1 h at 100 °C. Subsequently, $I-V$ curves were recorded by a potentiostat (Bio-Logic VMP3) in the two-electrode configuration. Alternatively, the three-necked glass flask was flushed with nitrogen, methane, or carbon dioxide by a gas flow rate of 30 mL·min^{-1}. After every measurement, the glass flask was evacuated for 30 min.

■ RESULTS AND DISCUSSION

Figure 1 shows the optical microscopy images of Co-MOF-74 and Co-MOF-74-TTF (Figure 1a,b). The as-synthesized Co-MOF-74 powder shows a red color (Figure 1a), whereas the infiltrated MOF powder appears to be black (Figure 1b). Figure 1c displays an SEM image of a typical Co-MOF-74-TTF crystal. The rodlike crystal has a width of 20 μm and a length of 70 μm. The one-dimensional pores of Co-MOF-74 with a diameter of 1.1−1.2 nm are aligned parallel to the long crystal axis.[32]

In order to characterize the crystal structure of Co-MOF-74-TTF, XRD was performed. Figure 2a compares the XRD patterns of Co-MOF-74 and Co-MOF-74-TTF to the simulated Co-MOF-74 pattern. The crystal structure of the infiltrated MOF is almost equal to the noninfiltrated Co-MOF-74. However, a slight shift to a lower 2θ value for the infiltrated MOF is observed. The UV/vis spectra of the MOFs are shown in Figure 2b. A higher absorption for Co-MOF-74-TTF within

600 and 800 nm compared to Co-MOF-74 can be observed. This proves the successful incorporation of TTF guest molecules into the MOF host structure. Another indication for a successful incorporation of TTF into the pore can be found in the IR spectra, measured at room temperature under air, as given in Figure S1 (Supporting Information). Co-MOF-74 shows ν OH stretching, which can be attributed either to the presence of carboxyl groups or of adsorbed water molecules in the range of 3000−3500 cm^{-1}. Because the infiltrated MOF does not show this stretching mode, we assume the TTF molecules to be infiltrated into the pores, causing reduced water adsorption at the open Co metal sites. These assumptions have been validated by thermogravimetric analysis (TGA) (Figure S2, Supporting Information).

The TGA of the empty Co-MOF-74 equilibrated in air shows a weight loss of 26.4% in the temperature range up to 100 °C, which can be assigned to adsorbed water. The Co-MOF-74-TTF sample contains a lower amount of water compared to the noninfiltrated MOF (5.7 %). Figure 2c shows the TGA of Co-MOF-74, Co-MOF-74-TTF, and TTF under the N_2 atmosphere. The results are normalized at 100 °C. The TGA curve of the infiltrated MOF is found between the curves of the empty Co-MOF-74 and the pure TTF. From TGA, we calculated a total amount of TTF infiltrated in Co-MOF-74 to be approximately 15 wt %.

Spatially resolved Raman investigations of Co-MOF-74-TTF crystals (Figure 2d) show the existence of two phases in the μm scale indicating that the TTF distribution is not homogeneous. One phase is in good accordance with the typical Raman patterns of the unloaded Co-MOF-74, while within the second phase, two additional peaks occur, which can be assigned to TTF.[35] The peak at 494 cm^{-1} is associated with the C−S stretching band and the other peak at 743 cm^{-1} is associated with C−H bending.[35] Further Information concerning the measured areas within the crystals can be found in the Supporting Information (Figure S3).

In order to confirm the existence of Co−S bindings in the second phase, XPS investigations were performed. Figure 3 shows the XPS investigations of Co-MOF-TTF and TTF at the S 2p edge. The S 2p spectra after linear background subtraction have been fit with spin−orbit doublets with shared energy difference and the area intensity ratio between the $2p_{3/2}$
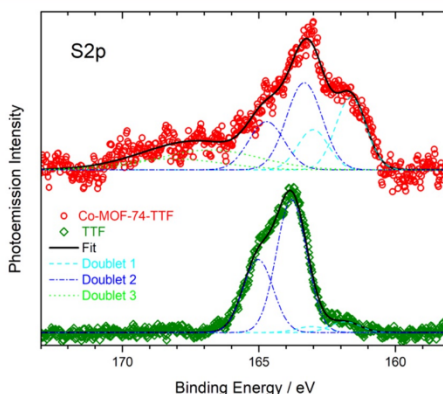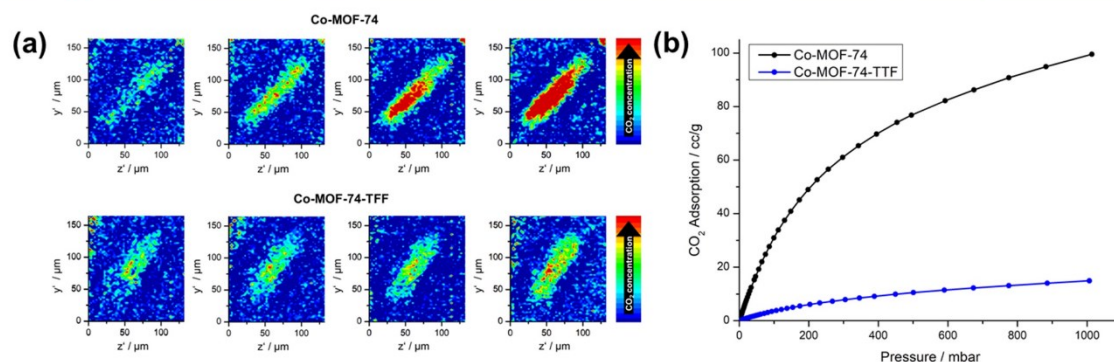

Figure 3. XPS investigation of Co-MOF-TTF and TTF at the S 2p edge.

Figure 4. (a) IR microscopic images of CO_2 adsorption on an empty Co-MOF-74 and a composite Co-MOF-74-TTF crystal shown in Figure 1c at 50, 200, 500, and 1000 mbar CO_2 pressure (from left to right). (b) CO_2 adsorption isotherms of the empty Co-MOF-74 and the composite Co-MOF-74-TTF at 25 °C.

and $p_{1/2}$ Gaussian peaks. For the TTF reference, two doublets can be found. Doublet 1 is low in intensity with the $2p_{3/2}$ peak located at 161.84 eV and doublet 2 is the major component located at 163.80 eV.

For the TTF encapsulated in the Co-MOF-74, doublet 1 is comparable to doublet 2 in intensity. The $2p_{3/2}$ binding energies are downshifted to 161.63 and 163.34 eV for doublets 1 and 2, respectively. In addition, the broad higher energy structure fit as doublet 3 emerges with the $2p_{3/2}$ peak located at 166.80 eV.

The large area intensity of doublet 1 in Co-MOF-74-TTF could be attributed to a sulfur-cobalt bonding state as cobalt sulfide and organic thiols bound on meta surfaces have the S 2p doublet in the same binding energy range.[36−39] The S-to-Co atomic ratio evaluated from the XPS data is approximately 6−7 to 1. Because a TTF molecule contains four sulfur atoms, this means that 1 Co atom interacts with approximately 1.6 TTF molecules (Figure S4, Supporting Information).

IR microscopy images were collected at 50, 200, 500, and 1000 mbar CO_2 pressure (Figure 4a). Because the Co-MOF-74 batch consists of equally shaped crystals like the one shown in Figure 1, we can directly compare the IR microscopic images of adsorbed CO_2 of the unloaded and the infiltrated Co-MOF-74. For Co-MOF-74, a significant increase of the CO_2 uptake is visible when the CO_2 pressure inside the cell is increased stepwise from 50 mbar up to 1000 mbar CO_2 (from left to right). In contrast to that, Co-MOF-74-TTF does not show a significant increase of CO_2 uptake with increasing CO_2 pressure because a part of its pore volume is blocked by infiltrating TTF. This finding is in good accordance with the IR absorbance spectra of Co-MOF-74-TTF measured at 10, 20, 50, 100, and 200 mbar CO_2 shown in Figure S5 (Supporting Information). The intensity of the CO_2 bands does not change when the pressure is varied stepwise from 10 to 200 mbar. It follows from IR imaging (Figure 4a) and IR spectroscopy (Figure S5, Supporting Information) that the CO_2 concentration in Co-MOF-74 increases stronger than that in Co-MOF-74-TTF when increasing the CO_2 pressure. Therefore, CO_2 adsorption isotherms of Co-MOF-74 and Co-MOF-74-TTF, showed in Figure 4b, were measured. On comparing the isotherms, the amount of adsorbed CO_2 is drastically reduced in Co-MOF-74-TTF because of the TTF molecules infiltrated into the pores.

As expected, our TTF-infiltrated MOF shows a measurable electric conductivity, similar to that found before for Co-MOF-74 doped with TCNQ.[29] One possible mechanism of the interaction between TTF and Co-MOF-74 might be based on through-bond conduction as suggested for TCNQ-MOFs before.[28] In addition to that, electrons may also conduct through π−π-stacking instead of bond conduction. To check the gas-sensing capability of Co-MOF-74-TTF, the electrical current was measured in dependence of the applied voltage. A measurement setup including a cell for gas sensing was built (Figure 5a). The cell features a gas inlet and outlet for changing the gas atmosphere in the round-bottom flask. The electrode setup (Figure 5b) consists of two stainless-steel electrodes which are held together with screws.

Pressed tablets of the MOF powders are placed between the electrodes, which are connected to the potentiostat with
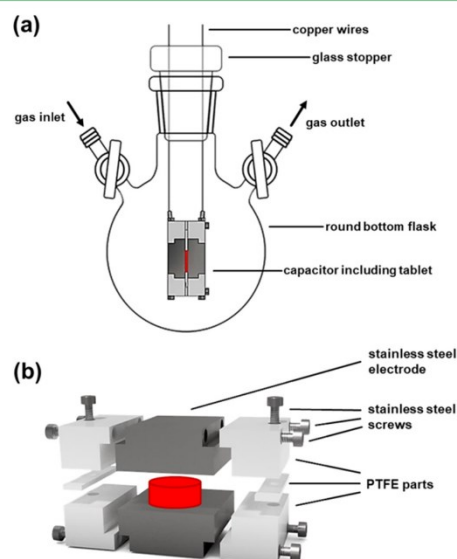
Figure 5. Measurement setup (a) and home-build electrodes in detail (b).
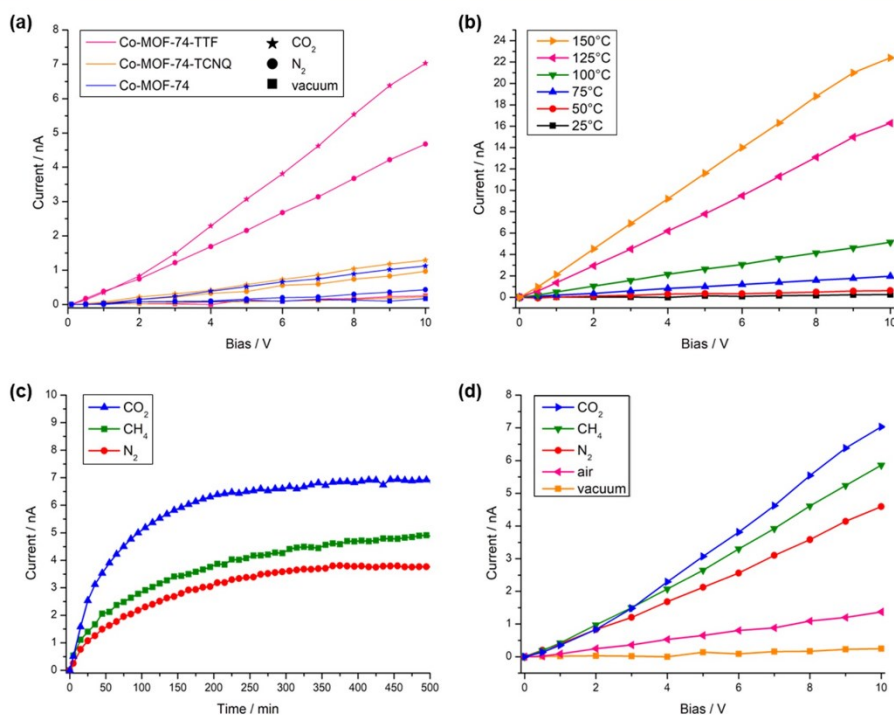
Figure 6. Electrical measurements. (a) $I-V$-curves of Co-MOF-74-TTF compared to Co-MOF-74 and Co-MOF-74-TCNQ under vacuum, N_2, and CO_2 atmospheres. (b) $I-V$-curves of Co-MOF-74-TTF under vacuum at different temperatures. (c) Long-term conductivity measurements of Co-MOF-74-TTF under N_2, CH_4, and CO_2 atmospheres with a bias of 10 V. The atmosphere was changed from vacuum to $N_2/CH_4/CO_2$ at 0 min. (d) $I-V$-curves of Co-MOF-74-TTF measured after 24 h under vacuum, air, N_2, CH_4, and CO_2 atmospheres.

copper wires through the air-tight glass stopper as shown in Figure 5a.

Figure 6a compares the $I-V$ curves of the unloaded Co-MOF-74 with the Co-MOF-74-TTF under vacuum, N_2, and CO_2. The electrical conductivity of the unloaded Co-MOF-74 is rather low under all conditions. Therefore, Co-MOF-74 is not a suited material for gas sensing via conductivity measurements. Co-MOF-74-TTF, on the other hand, exhibits evaluable electrical conductivity under the N_2 and CO_2 atmosphere. When compared to the TCNQ-loaded MOF, Co-MOF-74-TTF exhibits a significantly higher electrical conductivity and also larger changes in the conductivity caused by MOF−gas interactions. That is to say, the different gases cause on Co-MOF-74-TTF larger changes in the magnitude of the current and can be distinguished therefrom.

Furthermore, temperature-dependent conductivity measurements of Co-MOF-74-TTF were performed (Figure 6b). Long-time $I-V$ measurements were conducted under CO_2, CH_4, and N_2 at 10 V (Figure 6c). The gas atmosphere was changed from vacuum to different gases at time 0 min. A magnified $I-V$ plot from 0 to 200 s is shown in the Figure S6 (Supporting Information). These short-time measurements show that the TTF-MOF has a short response time regarding the gases.

However, because of transport limitation inside the pressed tablet, no equilibrium of the gas uptake was observed within the first 500 min. Therefore, the following $I-V$ curves were measured 24 h after the initial gas dosing. Figure 6d shows the $I-V$ curves of Co-MOF-74-TTF under vacuum, air, N_2, CH_4,

and CO_2. The highest conductivity was observed for CO_2, while the lowest conductivity was found for vacuum. The conductivity under ambient air was low as well.

In a previous publication, we observed shifts of the absorbance maxima in the UV/vis spectra for Co-MOF-74, which were dependent on the strength of the interaction between the MOF and the guest molecules.[32] Here, we observe a similar behavior for the electrical conductivity of the infiltrated MOF. CO_2 is interacting stronger with Co-MOF-74-TTF than CH_4 and N_2.

The interaction of the open metal sites of Co-MOF-74 with CO_2 can be further described as a Lewis acid−base interaction, with the metal center acting as a Lewis acid, while the CO_2 molecule behaves as an electron donor (Lewis base).[40] This interaction is further favored by the electronic deficiency of the metal sites, leading to a strong interaction between CO_2 and the cobalt center.[40] We assume that for Co-MOF-74-TTF, the CO_2 molecule, as an electron donor, leads to a higher response compared to CH_4 and N_2. Garcia et al. stated that the permanent dipole moment, which is present in the cobalt atoms, is able to induce the polarization of molecules like CH_4 and showed that the affinity of Co-MOF-74 toward CH_4 is lower than toward CO_2.[40] For N_2, as an inert gas, we assume an even lower interaction. Compared to CH_4, N_2 also possesses a lower polarizability.[41] These assumptions are in good accordance to the result of the electrical measurements shown in Figure 6d. When Co-MOF-74 is exposed to surrounding air, the conductivity is even lower than for N_2. We attribute this low sensitivity to the amount of water in air.

As shown before, Co-MOF-74 can be deactivated by H_2O.[33] Thus, it is possible that in Co-MOF-74-TTF, the TTF and H_2O molecules compete for the metal center resulting in lower current. We further investigated the behavior of Co-MOF-74-TTF under vacuum, CO_2, and N_2 atmospheres via Raman spectroscopy (Figure S7, Supporting Information). When gases become adsorbed in the crystals, gas-specific peak shifts of the characteristic modes of the Co-MOF-74-TTF can be observed. This is in good agreement with the behavior of the noninfiltrated MOF, which showed a shift of the characteristic peaks depending on the applied gas atmosphere as well, justified in more respectively less energetic binding modes.[30]

■ CONCLUSIONS

Following the Guest@MOF concept, we synthesized Co-MOF-74 with the organic semiconductor TTF molecules as a host−guest composite via a gas-phase incorporation route. XPS investigations confirm the existence of Co−S bindings (approximately 1.6 TTF molecules interact with 1 cobalt atom) between TTF and the open-metal Co-centers of the MOF. With TGA, we could prove a TTF loading of Co-MOF-74 of 15 wt %.

Co-MOF-74-TTF has a significantly higher conductivity in comparison to the unloaded and TCNQ-infiltrated Co-MOF-74. Furthermore, $I-V$ experiments under different gas atmospheres were performed, recommending Co-MOF-74-TTF as an excellent material for gas-sensing devices because of modification of resistivity. IR imaging and CO_2 physisorption show a decreased ability of Co-MOF-74-TTF to adsorb CO_2. Because of different strengths of the interactions between a gas and the MOF, conductivity changes could be observed. The highest conductivity was obtained for CO_2 because of the strong interaction between CO_2 and the Co-centers of the MOF. For weaker gas−MOF interactions (CO_2 > CH_4 > N_2), a smaller increase of the conductivity is observed. Raman measurements have proven different interactions of Co-MOF-74-TTF with gas molecules. Peak shifts of the characteristic modes are observed for different gas atmospheres.

■ ASSOCIATED CONTENT

⑤ Supporting Information

The Supporting Information is available free of charge on the ACS Publications website at DOI: 10.1021/acsami.8b22002.

> Co-MOF-74 IR-spectra compared to Co-MOF-74 infiltrated with TTF; thermogravimetric analysis measurements of Co-MOF-74 and Co-MOF-74-TTF; Co-MOF-74-TTF crystal indicating the two different phases of the material; XPS investigation of Co-MOF-TTF and Co-MOF-74 at the Co 2p edge; IR spectra of Co-MOF-74 and Co-MOF-74-TTF measured at RT with 10, 20, 50, 100, and 200 mbar CO_2; and short-time $I-V$ measurements of Co-MOF-74-TTF under CO_2, CH_4, and N_2 (PDF)

■ AUTHOR INFORMATION

Corresponding Authors

*E-mail: ina.strauss@pci.uni-hannover.de (I.S.).
*E-mail: juergen.caro@pci.uni-hannover.de (J.C.).

ORCID ⊙

Ina Strauss: 0000-0001-8824-4162
Karsten Lange: 0000-0002-6741-6911
Nadja C. Bigall: 0000-0003-0171-1106
Thomas Pichler: 0000-0001-5377-9896
Jürgen Caro: 0000-0003-0931-085X

Notes

The authors declare no competing financial interest.

■ REFERENCES

(1) Batten, S. R.; Champness, N. R.; Chen, X.-M.; Garcia-Martinez, J.; Kitagawa, S.; Öhrström, L.; O'Keeffe, M.; Paik Suh, M.; Reedijk, J. Terminology of Metal-Organic Frameworks and Coordination Polymers (IUPAC Recommendations 2013). *Pure Appl. Chem.* **2013**, *85*, 1715−1724.

(2) Yaghi, O. M.; O'Keeffe, M.; Ockwig, N. W.; Chae, H. K.; Eddaoudi, M.; Kim, J. Reticular Synthesis and the Design of new Materials. *Nature* **2003**, *423*, 705−714.

(3) Wang, Z.; Chen, G.; Ding, K. Self-Supported Catalysts. *Chem. Rev.* **2009**, *109*, 322−359.

(4) Wu, M.-X.; Yang, Y.-W. Metal-Organic Framework (MOF)-Based Drug/Cargo Delivery and Cancer Therapy. *Adv. Mater.* **2017**, *29*, 1606134.

(5) Li, J.-R.; Kuppler, R. J.; Zhou, H.-C. Selective Gas Adsorption and Separation in Metal-Organic Frameworks. *Chem. Soc. Rev.* **2009**, *38*, 1477−1504.

(6) Li, Y.-X.; Ji, Y.-N.; Jin, M.-M.; Qi, S.-C.; Li, S.-S.; Xue, D.-M.; Yue, M. B.; Liu, X.-Q.; Sun, L.-B. Controlled Construction of Cu(I) Sites within Confined Spaces via Host-Guest Redox: Highly Efficient Adsorbents for Selective Co Adsorption. *ACS Appl. Mater. Interfaces* **2018**, *10*, 40044−40053.

(7) Morris, R. E.; Wheatley, P. S. Gas Storage in Nanoporous Materials. *Angew. Chem., Int. Ed.* **2008**, *47*, 4966−4981.

(8) Kreno, L. E.; Leong, K.; Farha, O. K.; Allendorf, M.; van Duyne, R. P.; Hupp, J. T. Metal-Organic Framework Materials as Chemical Sensors. *Chem. Rev.* **2012**, *112*, 1105−1125.

(9) Achmann, S.; Hagen, G.; Kita, J.; Malkowsky, I.; Kiener, C.; Moos, R. Metal-Organic Frameworks for Sensing Applications in the Gas Phase. *Sensors* **2009**, *9*, 1574−1589.

(10) Jazdi, N. Cyber physical systems in the context of Industry 4.0. *IEEE International Conference on Automation, Quality and Testing, Robotics (AQTR)*, 2014; pp 1−4.

(11) Capone, S.; Forleo, A.; Francioso, L.; Rella, R.; Siciliano, P.; Spadavecchia, J.; Presicce, D. S.; Taurino, A. M. Solid State Gas Sensors: State of the Art and Future Activities. *Adv. Mater.* **2003**, *5*, 1335−1348.

(12) Razavi, S. A. A.; Masoomi, M. Y.; Morsali, A. Stimuli-Responsive Metal-Organic Framework (MOF) with Chemo-Switchable Properties for Colorimetric Detection of CHCl3. *Chem.—Eur. J.* **2017**, *23*, 12559−12564.

(13) Zhang, Y.; Li, B.; Ma, H.; Zhang, L.; Zhang, W. An RGH-MOF as a naked eye colorimetric fluorescent sensor for picric acid recognition. *J. Mater. Chem. C* **2017**, *5*, 4661−4669.

(14) Smith, M. K.; Jensen, K. E.; Pivak, P. A.; Mirica, K. A. Direct Self-Assembly of Conductive Nanorods of Metal−Organic Frameworks into Chemiresistive Devices on Shrinkable Polymer Films. *Chem. Mater.* **2016**, *28*, 5264−5268.

(15) Campbell, M. G.; Sheberla, D.; Liu, S. F.; Swager, T. M.; Dincă, M. Cu_3(hexaiminotriphenylene)$_2$: An Electrically Conductive 2D

Metal-Organic Framework for Chemiresistive Sensing. *Angew. Chem., Int. Ed.* **2015**, *54*, 4349−4352.

(16) Campbell, M.; Dincă, M. Metal-Organic Frameworks as Active Materials in Electronic Sensor Devices. *Sensors* **2017**, *17*, 1108.

(17) Dincă, M.; Léonard, F. Metal−Organic Frameworks for Electronics and Photonics. *MRS Bull.* **2016**, *41*, 854−857.

(18) Leong, C. F.; Usov, P. M.; D'Alessandro, D. M. Intrinsically conducting metal-organic frameworks. *MRS Bull.* **2016**, *41*, 858−864.

(19) Takaishi, S.; Hosoda, M.; Kajiwara, T.; Miyasaka, H.; Yamashita, M.; Nakanishi, Y.; Kitagawa, Y.; Yamaguchi, K.; Kobayashi, A.; Kitagawa, H. Electroconductive Porous Coordination Polymer $Cu[Cu(pdt)_2]$ Composed of Donor and Acceptor Building Units. *Inorg. Chem.* **2009**, *48*, 9048−9050.

(20) Gándara, F.; Uribe-Romo, F. J.; Britt, D. K.; Furukawa, H.; Lei, L.; Cheng, R.; Duan, X.; O'Keeffe, M.; Yaghi, O. M. Porous, Conductive Metal-Triazolates and Their Structural Elucidation by the Charge-Flipping Method. *Chem.—Eur. J.* **2012**, *18*, 10595−10601.

(21) Sun, L.; Miyakai, T.; Seki, S.; Dincă, M. Mn2(2,5-disulfhydrylbenzene-1,4-dicarboxylate): A Microporous Metal-Organic Framework with Infinite (−Mn-S−)∞ Chains and High Intrinsic Charge Mobility. *J. Am. Chem. Soc.* **2013**, *135*, 8185−8188.

(22) Darago, L. E.; Aubrey, M. L.; Yu, C. J.; Gonzalez, M. I.; Long, J. R. Electronic Conductivity, Ferrimagnetic Ordering, and Reductive Insertion Mediated by Organic Mixed-Valence in a Ferric Semi-quinoid Metal-Organic Framework. *J. Am. Chem. Soc.* **2015**, *137*, 15703−15711.

(23) Talin, A. A.; Centrone, A.; Ford, A. C.; Foster, M. E.; Stavila, V.; Haney, P.; Kinney, R. A.; Szalai, V.; El Gabaly, F.; Yoon, H. P.; Léonard, F.; Allendorf, M. D. Tunable Electrical Conductivity in Metal-Organic Framework Thin-Film Devices. *Science* **2014**, *343*, 66−69.

(24) Chui, S. S. Chemically Functionalizable Nanoporous Material $[Cu_3(TMA)_2(H_2O)_3]_n$. *Science* **1999**, *283*, 1148−1150.

(25) Kepler, R. G.; Bierstedt, P. E.; Merrifield, R. E. Electronic Conduction and Exchange Interaction in a New Class of Conductive Organic Solids. *Phys. Rev. Lett.* **1960**, *5*, 503−504.

(26) Allendorf, M. D.; Foster, M. E.; Léonard, F.; Stavila, V.; Feng, P. L.; Doty, F. P.; Leong, K.; Ma, E. Y.; Johnston, S. R.; Talin, A. A. Guest-Induced Emergent Properties in Metal-Organic Frameworks. *J. Phys. Chem. Lett.* **2015**, *6*, 1182−1195.

(27) Sengupta, A.; Datta, S.; Su, C.; Herng, T. S.; Ding, J.; Vittal, J. J.; Loh, K. P. Tunable Electrical Conductivity and Magnetic Property of the Two Dimensional Metal Organic Framework $[Cu(TPyP)-Cu_2(O_2CCH_3)_4]$. *ACS Appl. Mater. Interfaces* **2016**, *8*, 16154−16159.

(28) Guo, Z.; Panda, D. K.; Gordillo, M. A.; Khatun, A.; Wu, H.; Zhou, W.; Saha, S. Lowering Band Gap of an Electroactive Metal-Organic Framework via Complementary Guest Intercalation. *ACS Appl. Mater. Interfaces* **2017**, *9*, 32413−32417.

(29) Shiozawa, H.; Bayer, B. C.; Peterlik, H.; Meyer, J. C.; Lang, W.; Pichler, T. Doping of Metal-Organic Frameworks Towards Resistive Sensing. *Sci. Rep.* **2017**, *7*, 2439.

(30) Rosi, N. L.; Kim, J.; Eddaoudi, M.; Chen, B.; O'Keeffe, M.; Yaghi, O. M. Rod Packings and Metal−Organic Frameworks Constructed from Rod-Shaped Secondary Building Units. *J. Am. Chem. Soc.* **2005**, *127*, 1504−1518.

(31) Dietzel, P. D. C.; Georgiev, P. A.; Eckert, J.; Blom, R.; Strässle, T.; Unruh, T. Interaction of hydrogen with accessible metal sites in the metal-organic frameworks M2(dhtp) (CPO-27-M; M = Ni, Co, Mg). *Chem. Commun.* **2010**, *46*, 4962−4964.

(32) Strauss, I.; Mundstock, A.; Hinrichs, D.; Himstedt, R.; Knebel, A.; Reinhardt, C.; Dorfs, D.; Caro, J. Vis/NIR- und Raman-Untersuchung der Wechselwirkung von Gastmolekülen mit Co-MOF-74. *Angew. Chem. Int. Ed.* **2018**, *130*, 7434−7439.

(33) Wudl, F.; Wobschall, D.; Hufnagel, E. J. Electrical conductivity by the bis(1,3-dithiole)-bis(1,3-dithiolium) system. *J. Am. Chem. Soc.* **1972**, *94*, 670−672.

(34) Chmelik, C.; Mundstock, A.; Dietzel, P. D. C.; Caro, J. Idiosyncrasies of Co_2(dhtp): In Situ-Annealing by Methanol. *Microporous Mesoporous Mater.* **2014**, *183*, 117−123.

(35) Adeel, S. M.; Martin, L. L.; Bond, A. M. Redox-induced solid-solid state transformation of tetrathiafulvalene (TTF) microcrystals into mixed-valence and π-dimers in the presence of nitrate anions. *J. Solid State Electrochem.* **2014**, *18*, 3287−3298.

(36) Moulder, J. F.; Stickle, W. F.; Sobol, P. E.; Bomben, K. D. *Handbook of X-ray Photoelectron Spectroscopy*; PerkinElmer Corporation: Eden Prairie, 1992; p 61.

(37) Castner, D. G.; Hinds, K.; Grainger, D. W. X-ray Photoelectron Spectroscopy Sulfur 2p Study of Organic Thiol and Disulfide Binding Interactions with Gold Surfaces. *Langmuir* **1996**, *12*, 5083−5086.

(38) Rufael, T. S.; Huntley, D. R.; Mullins, D. R.; Gland, J. L. Methyl Thiolate on Ni(111): Multiple Adsorption Sites and Mechanistic Implications. *J. Phys. Chem.* **1995**, *99*, 11472−11480.

(39) Mullins, D. R.; Lyman, P. F. Adsorption and reaction of methanethiol on tungsten(001). *J. Phys. Chem.* **1993**, *97*, 9226−9232.

(40) García, E. J.; Mowat, J. P. S.; Wright, P. A.; Pérez-Pellitero, J.; Jallut, C.; Pirngruber, G. D. Role of Structure and Chemistry in Controlling Separations of CO_2/CH_4 and $CO_2/CH_4/CO$ Mixtures over Honeycomb MOFs with Coordinatively Unsaturated Metal Sites. *J. Phys. Chem. C* **2012**, *116*, 26636−26648.

(41) Li, J.-R.; Kuppler, R. J.; Zhou, H.-C. Selective Gas Adsorption and Separation in Metal-Organic Frameworks. *Chem. Soc. Rev.* **2009**, *38*, 1477−1504.

7 UiO-66

7.1 Preface

In the following two publications, the performance of zirconium-based UiO-66 and UiO-66-NH$_2$ frameworks will show our effort to evaluate their possible incorporation into gas sensing devices. Therefore, the first publication is focused on the investigation of the acidic and basic properties of UiO-66 and UiO-66-NH$_2$. While the synthesis, characterization and scriptualisation of these parts and the theoretical MOF part were performed by the author of this thesis, the FTIR study to investigate the evolution of the acid and basic sites was performed by Kristina Chakarova, Mihail Mihaylov and Nikola Drenchev. By using probe molecules (like carbon monoxide, nitrogen, acetonitrile) and studying the MOFs adsorption behaviours, a deeper insight into the development of their acid-basic properties would be obtained. The manuscript was authored by Kristina Chakarova and Konstantin Hadjiivanov.

With an enhanced understanding regarding the adsorption properties of UiO-66 materials, the second publication evaluated these materials regarding their possible incorporation into CO$_2$ sensing devices. The CO$_2$ dependent FTIR measurements were performed by Kristina Chakarova and Mihail Mihaylov and showed that the NH$_2$ groups significantly improve the capability of sensing low CO$_2$ concentrations. The same investigations also revealed that the co-existence of water molecules during low CO$_2$ concentration measurements further enhance the performance of UiO-66-NH$_2$. The FTIR section was scriptualised by Konstantin Hadjiivanov and Kristina Chakarova. Via capacity measurements the capability of UiO-66 materials toward high carbon dioxide concentrations was proven. Based on Maxwell-Wagner-Sillars polarization, the adsorption of CO$_2$ on UiO-66-NH$_2$ causes a decrease of the capacity at low frequencies, which can be easily sensed. Alexander Mundstock took a supportive role during the process of the manuscript by helping with the interpretation of the dielectric data as well as with the construction of the measurement cell and by proofreading the draft. Natalija Guschanski ensured the high quality of the dielectrical investigations by guiding the interpretation of the data with her extensive expertise in the field of frequency dependent dielectric research. Jürgen Caro ensured the high quality of the publication, by supporting the whole process with his extensive expertise concerning the field of MOFs, as well as refining the manuscript.

All not-mentioned tasks within the development of the manuscript, such as the synthesis, characterization, interpretation and investigation of the materials as well as the construction of measurement cells and the authoring of the manuscript, were performed by the author of this thesis.

7.2 Evolution of acid and basic sites in UiO-66 and UiO-66-NH$_2$ metal-organic frameworks: FTIR study by probe molecules

K. Chakarova, I. Strauss, M. Mihaylov, N. Drenchev, K. Hadjiivanov
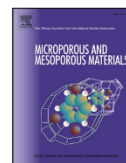
Evolution of acid and basic sites in UiO-66 and UiO-66-NH$_2$ metal-organic frameworks: FTIR study by probe molecules

Kristina Chakarova[a], Ina Strauss[b], Mihail Mihaylov[a], Nikola Drenchev[a], Konstantin Hadjiivanov[a,c,*]

[a] Institute of General and Inorganic Chemistry, Bulgarian Academy of Sciences, Sofia, 1113, Bulgaria
[b] Institute of Physical Chemistry and Electrochemistry, Leibniz Universität Hannover, Callinstraße 3A, D-30167, Hannover, Germany
[c] Bulgarian Academy of Sciences, Sofia, 1040, Bulgaria

ARTICLE INFO

ABSTRACT

Metal-organic frameworks (MOFs) and MOF-based materials find increasing and diverse applicability. The performance of MOFs in adsorption and catalysis is strongly related to their acid-basic properties. Here we report on the development of acidity (protonic and Lewis) and basicity during thermo-vacuum treatment of two MOFs of practical importance, UiO-66 and UiO-66-NH$_2$. Residual DMF is more strongly bound to UiO-66-NH$_2$ but is practically removed from both samples at 473 K. The structural μ_3-OH groups (belonging to the Zr$_6$ cluster) for both samples are observed at 3678-3672 cm^{-1}. Their intrinsic frequency was estimated to be at 3682 cm^{-1} and the lower values detected are due to a very weak H-bonding to the MOF walls. Both samples are practically dehydroxylated at 523 K but easily re-hydroxylated at ambient temperature in presence of water. Three probe molecules (CO, N$_2$ and CD$_3$CN) were utilized to assess the acidity and basicity of the samples. Low-temperature CO adsorption experiments revealed a weak protonic acidity of the UiO-66 sample evacuated at 298 K: the CO induced shift of the O–H modes ($\Delta_t\nu_{OH}$, calculated on the basis of the intrinsic frequency) was -83 cm^{-1} with a small fraction of more acidic groups ($\Delta_t\nu_{OH} = -93$ cm^{-1}). Evacuation at 473 K leads to a strong (and reversible) decrease in the population of the structural OH groups in UiO-66 and creation of a fraction of more acidic hydroxyls ($\Delta_t\nu_{OH} = -108$ cm^{-1}). Similar results were obtained with the DMF-free UiO-66-NH$_2$: the $\Delta_t\nu_{OH}$ was -91 cm^{-1} for a sample evacuated at 298 K while for a sample evacuated at 473 K two shifts were observed, -98 and -117 cm^{-1}. These results were fully confirmed by adsorption of N$_2$. In this case an additional N–N band was detected at 2324 cm^{-1} (2246 cm^{-1} after adsorption of ^{15}N$_2$) and attributed to N$_2$ polarized by O^{2-} basic sites. The band developed with the pre-evacuation temperature evidencing creation of basic sites. No Lewis acidity was established by CO and N$_2$ probes on samples evacuated up to 573 K. However, with samples evacuated at 473 K or higher temperature, Zr^{4+} Lewis acid sites were unambiguously monitored by CD$_3$CN through a ν(CN) band at 2299 cm^{-1}. The existence of this "hidden" Lewis acidity is explained by structural re-arrangement of the Zr^{4+} environment induced by relatively strong bases as CD$_3$CN. Subsequent re-hydroxylation of the sample provokes almost full disappearance of the Lewis acid sites at the expense of OH groups formed.

1. Introduction

The growing interest to metal organic frameworks (MOFs) is due to their various potential applications. In particular, MOFs are considered as very perspective materials for gas separation [1,2]. Different strategies have been applied to control the adsorption properties of MOFs. The introduction of functional groups into the structure has led to promising results. For instance, the advantages of MIL-53-NH$_2$ for CO$_2$ separation as compared to MIL-53 have been thoroughly discussed [3]. In this work we compare the sorption properties of UiO-66 and UiO-66-NH$_2$ towards different probe molecules in order to identify the nature of the active sites for adsorption and to estimate the effect of the NH$_2$ groups on the MOF properties.

UiO-66 is built up from [Zr$_6$O$_4$(OH)$_4$] clusters which are linked with 1,4-benzenedicarboxylic acid [4] (see Fig. 1). There are several works dealing with the hydroxyl coverage and sorption properties of UiO-66 [4–38]. The material is interesting with its reversible hydroxylation/dehydroxylation properties attributed to the easy ability of the Zr^{4+} cations to change their coordination state. It is established that UiO-66 evacuated at ambient temperature is characterized by two main
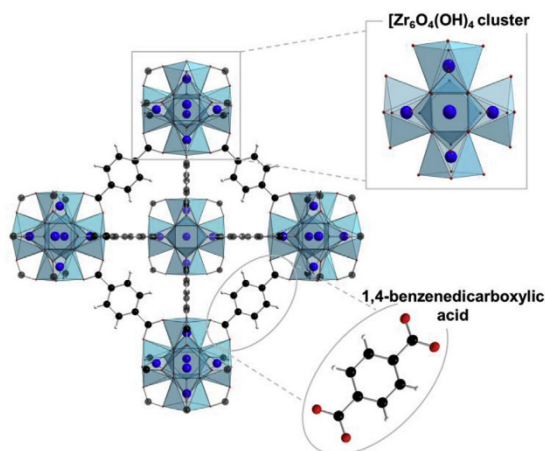
Fig. 1. Crystal structure of UiO-66: [Zr$_6$O$_4$(OH)$_4$] clusters linked by 1,4-benzene-dicarboxylic acid.

families of hydroxyl groups: isolated ones (μ_3-OH), monitored in the IR spectra by a band at ca. 3675 cm^{-1} [6,9,28–31,36–39], and perturbed species, characterized by a broad band centered around 3350-3250 cm^{-1} [6,9,28,36]. Recent studies indicated that the latter band is associated with hydroxyls that are H-bonded to organic residues [22,36]. Some other additional (up to eleven) low-intensity IR hydroxyl bands were also detected and again attributed to presence of admixtures [6,9]. The hydroxyl bands are removed by evacuation at elevated temperatures but subsequent adsorption of water practically restores the initial spectra. It was also proposed [18] that H-bonded hydroxyls at missing linker defects (where two Zr sites are occupied by terminal H$_2$O and OH ligands, respectively) give rise to a band at 2745 cm^{-1}. However, in a following work the authors re-assigned this band to a combination mode [25].

According to the literature [5,20,31], UiO-66-NH$_2$ is characterized by μ_3-OH band at 3675-3673 cm^{-1} which is considered to be identical with that found with UiO-66. The NH$_2$ groups in UiO-66-NH$_2$ are detected by ν_s(NH$_2$) at ca. 3515 cm^{-1}; ν_{as}(NH$_2$) at ca. 3390 cm^{-1}; δ(NH$_2$) at 1629 cm^{-1} and ν(C$_{ar}$-N) at 1340 and 1257 cm^{-1} [14,19,21,31–33,35,37]. Note that with some flexible MOFs, as MIL-53(Al), the NH$_2$ groups attached to the linker form H-bonds with the structural hydroxyls [4,40] which is not the case with UiO-66. Importantly, the NH$_2$ groups are a good base for post-synthetic reactions leading to different functionalized materials [37].

The surface acidity of UiO-66 has been tested by CO as a probe molecule. It was found that the 3675 cm^{-1} hydroxyl groups are characterized by a weak acidity (adsorption induced shift, $\Delta\nu$OH = -83 cm^{-1} [6] or -69 cm^{-1} [39]).

Adsorption of 5-nonanone was used to compare the Lewis acidity of UiO-66 and UiO-66-NH$_2$ samples [16]. The ν(CO) band for ketone adsorbed on the two samples was observed at 1649 and 1646 cm^{-1}, respectively. On this basis the authors concluded that the electron-donating NH$_2$-groups decrease the acidity of the sample. On the contrary, NH$_2$ groups create strong basic sites (a ν_{C-D} band of adsorbed CDCl$_3$ at 2245 cm^{-1} vs. a band at 2253 cm^{-1} detected with UiO-66) [16]. However, there are no data comparing the properties of the hydroxyl groups of both materials.

The aim of this work is to perform a comparative study of UiO-66 and UiO-66-NH$_2$ and to conclude on the effect of the introduced NH$_2$ groups on the properties of the hydroxyl groups, hydroxylation/dehydroxylation processes and the entire adsorption properties of the samples.

2. Experimental

2.1. Synthesis of UiO-66 and UiO-66-NH$_2$

The UiO-66 and UiO-66-NH$_2$ samples were synthesized via a benzoic acid modulated hydrothermal synthesis following a slightly modified recipe reported elsewhere [41]. For the powder synthesis of UiO-66, 0.28 g of zirconium chloride (ZrCl$_4$, anhydrous, 98%, Alfa Aesar) was solved in 4.5 mL dimethylformamide (DMF, 99.8%, Carl Roth). A second solution containing of 4.4 g benzoic acid (C$_7$H$_6$O $\geq$ 99.5%, Sigma Aldrich) and 0.42 g terephthalic acid (H$_2$bdc, 98%, Sigma Aldrich) in 10 mL DMF was prepared. Both solutions were heated up to 423 K and combined afterwards in a Teflon lined autoclave. The autoclave was placed in a conventional oven for 24 h at 453 K. The crystals were washed several times with MeOH and dried at 333 K. For the powder synthesis of UiO-66-NH$_2$, 0.46 g of 2-aminoterephthalic acid (NH$_2$bdc, 99%, Sigma Aldrich) was used instead of H$_2$bdc.

2.2. Characterization

In order to evaluate the crystal structure, X-Ray diffraction measurements of UiO-66 and UiO-66-NH$_2$ samples were performed on a Bruker D8 Advance X-ray diffractometer with LYNXEYE detection technology and Cu$_{K\alpha}$ (λ = 0.154 nm) radiation. A 2θ-range from 5° to 30° was applied (step size 0.03, time per step 155 s) and the samples were rotated during the measurements.

Scanning Electron Microscopy (SEM) micrographs of UiO-66 and UiO-66-NH$_2$ were performed at a field emission scanning electron microscope JEOL JSM-6700F, with a cold field emission gun. An acceleration voltage of 2 kV and acceleration current of 10 µA were used. The crystals were deposited on a graphite sample holder.

2.3. FTIR spectroscopy

FTIR spectra were recorded with a Nicolet 6700 FTIR spectrometer accumulating 64 scans at a spectral resolution of 2 cm^{-1}. Self–supporting pellets (ca. 10 mg cm^{-2}) were prepared from the sample powder and treated directly in a purpose-made IR cell allowing measurement at ambient and low (ca. 100 K) temperature. The cell was connected to a vacuum-adsorption apparatus with a residual pressure below 10^{-3} Pa. Prior to the adsorption experiments, the samples were activated by vacuum treatment at different temperatures. The partly deuterated materials were prepared in situ by introduction of D$_2$O (5 mbar) directly in the IR cell, followed by evacuation. The adsorbates used had the following characteristics: CO (Merck, 99.5%); N$_2$ (Messer, 99.999%); ^{15}N$_2$ (Aldrich, 98 at. % ^{15}N) and CD$_3$CN (Merck, deuteration degree 99.96%).

3. Results

3.1. Crystal Structure and Morphology

The crystalline structure of the synthesized UiO-66 and UiO-66-NH$_2$ powders has been evaluated by XRD measurements (see Fig. 2). As expected, the UiO-66-NH$_2$ powder shows a similar XRD as the UiO-66 powder. Both results are in good accordance with the literature pattern of UiO-66.

The morphologies of UiO-66 and UiO-66-NH$_2$ crystals were characterized by SEM and the results are shown in Fig. 3. Both samples consist of octahedrally shaped, nano-scaled crystals. The UiO-66 sample exhibits a narrow crystal size distribution ranging between 150 and 250 nm, while the UiO-66-NH$_2$ sample exhibits smaller particles with a mean crystal size between 100 and 200 nm.
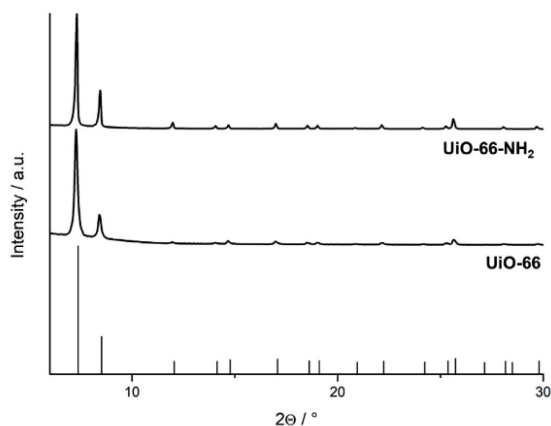
Fig. 2. XRD patterns of UiO-66 and UiO-66-NH$_2$ compared to the literature data of UiO-66.

3.2. Background FTIR spectra

3.2.1. UiO-66

There are several works reporting the background spectra of UiO-66 and here we will briefly underline the most important observations related to this study. The evolution of the IR spectra of the UiO-66 sample after evacuation at different temperature is presented in Fig. 4 (more details are given in the Supporting Information, see Fig. S1). The spectrum of the evacuated sample (Fig. 4, spectrum a) is consistent with literature reports [9] and displays very intense bands in the 1700–1250 cm^{-1} region, arising from the carboxylate groups and phenyl ring deformations. Bands in the 3100-2800 cm^{-1} region are due to C−H stretching modes. A sharp band is detected at 3673 cm^{-1} (see also the left inset in Fig. 4) and is attributed to free μ$_3$-bridging hydroxyls belonging to Zr$_6$ clusters [6,22,23,25,27–31,36,38]. The appearance of this band after evacuation at ambient temperature indicates easy breaking of the H-bond with water present on non-activated sample (Fig. S1) and a low acidity of the μ$_3$-OH groups.

A broad band centered around 3350 cm^{-1} evidences H-bonded OH groups. Most probably the band has a complex origin. A careful inspection of the 5500-5000 cm^{-1} region (where molecular H$_2$O combination modes, unique to H$_2$O are observed [42]) indicates a weak band at 5250 cm^{-1} which suggests the existence of small amount of non-dissociated water (Fig. S1, left inset, spectrum a). Therefore, the broad OH band at 3350 cm^{-1} is at least partly due to residual water. In agreement with recent reports [6,11,22], we assign part of this band to OH groups H-bonded to organic residues. Indeed, bands at 1730, 1705 and 1227 cm^{-1} were recorded and associated with esters [25] and residual terephthalic acid (probably isolated species), respectively. The

band at 1667 cm^{-1} together with a corresponding weak band at 1096 cm^{-1} arises from residual with residual DMF [6,22,25,34,36].

Upon heating to 373 K, spectral changes are well expressed in the 1750–1600 cm^{-1} region indicating about 25% loss of free acid and DMF impurities (see the right inset in Fig. 4). These impurities are practically removed at 473 K. At this temperature, the μ$_3$-OH band showed a 72% decrease in intensity, signaling a large removal of structure hydroxyls (dehydroxylation). These hydroxyls are almost completely removed after the final evacuation at 573 K. The observations are in general agreement with earlier reports [6,22,30].

Subsequent adsorption/desorption of water leads to full restoration of the intensity of the μ$_3$-OH groups but weak bands of esters/terephthalic acid (1732 and 1704 cm^{-1}) also reappeared (Fig. 4, spectrum e). At the same time, a band at ca. 3350 cm^{-1} emerged, with a lower intensity than with the initial sample. This is consistent with the association of a part of the broad band around 3350 cm^{-1} with organic residues.

3.2.2. UiO-66-NH$_2$

The IR spectra of UiO-66-NH$_2$ after evacuation at different temperatures are shown in Fig. 5 (for more details see also Figs. S2 and S3). We note that, due to the smaller particle size of the UiO-66-NH$_2$ material the light scattering is very low. Indeed, it is seen from Fig. S3 that an increase of the absorbance with the wavenumber is observed with the UiO-66 sample in the 4000–2000 cm^{-1} region which is not the case with UiO-66-NH$_2$.

After evacuation at ambient temperature the spectrum of UiO-66-NH$_2$ contains a weak band at 3673 cm^{-1} due to the OH stretching modes of μ$_3$-OH groups. Two bands, at 3477 and 3375 cm^{-1}, are assigned to the ν_{as}(NH$_2$) and ν_s(NH$_2$) modes, respectively. A broad absorbance centered around 3300 cm^{-1} evidences the existence of H-bonded hydroxyls. Different C−H modes are observed in the 3100-2800 cm^{-1} region. In particular, bands in the 2980-2910 cm^{-1} region are indicative of methyl groups. The bands at 1337 and 1258 cm^{-1} are attributed to ν(C−N) modes. We note the existence of two strong DMF features around 1660 and 1095 cm^{-1}. The high intensity of these bands indicates that DMF is relatively strongly bound to the material.

Evacuation at elevated temperatures leads to the following important changes in the spectra:

- The μ$_3$-OH band initially develops (up to 348 K) without substantial change in position. Then (up to 423 K) it is gradually red shifted to 3669 cm^{-1}. Finally, at 473 K the band starts to decline noticeably.
- The NH$_2$ stretching bands are gradually converted into a new set of bands, at 3508 and 3394 cm^{-1}.
- The broad OH band gradually disappears. Difference spectra indicate that first a component around 3272 cm^{-1} vanishes, followed by a component centered at ca. 3150 cm^{-1}.
- The DMF bands around 1660 and 1095 cm^{-1} gradually disappear, their intensity being low after evacuation at 423 K.
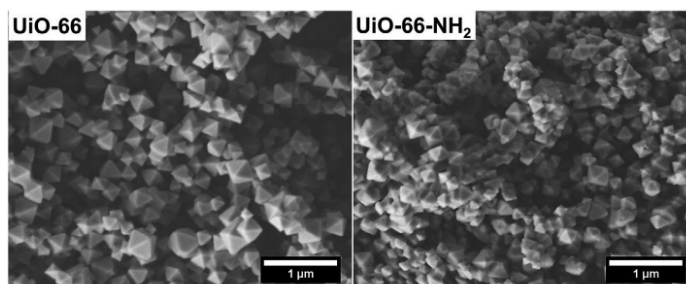

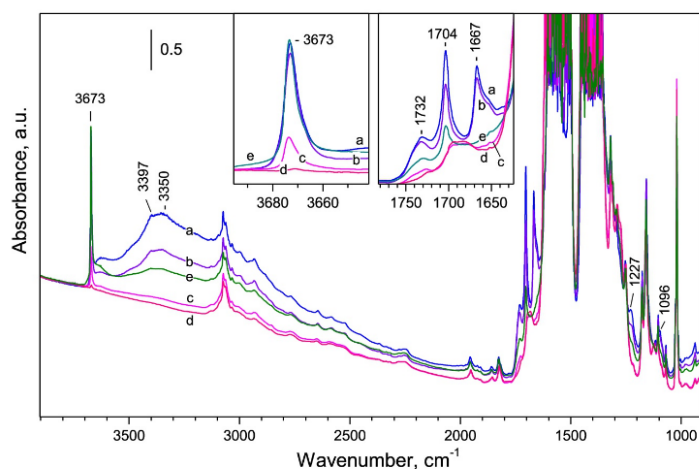**Fig. 3.** SEM images of UiO-66 (left) and UiO-66-NH$_2$ (right).

112

Fig. 4. FTIR spectra of UiO-66 evacuated at 298 K (a), 373 K (b), 473 K (c) and 573 K (d). Spectrum (e) refers to a sample re-hydroxylated after (d) and then evacuated at 298 K.
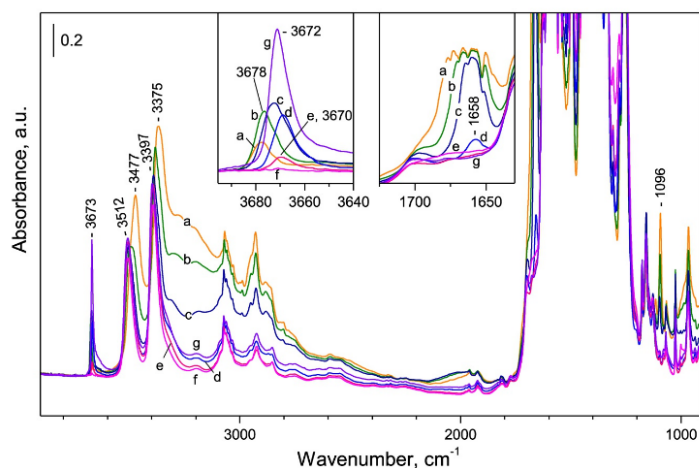

Fig. 5. FTIR spectra of UiO-66-NH$_2$ evacuated at 298 K (a), 348 K (b) 373 K (c), 423 K (d) 473 K (e) and 523 K (f). Spectrum (g) refers to a sample re-hydroxylated after (d) and then evacuated at 298 K.

The fact that NH$_2$-functionalized material contains much more residual DMF than UiO-66 indicates that the −NH$_2$ groups participate in the bonding of DMF and this bonding is stronger than the bonding mode with the participation of the structural hydroxyls. It seems that the shifts and initial development of O−H and N−H bands listed above are mainly due to gradual removal of the DMF (1660 and 1095 cm^{-1}) upon stepwise heating in vacuum.

In order to check the hydroxylation/dehydroxylation abilities of the material, we have studied water adsorption/desorption on a sample with DMF removed by prolonged evacuation at 443 K (Fig. 6).

Introduction of water to the sample leads to development of broad features centered around 5200 and 3250 cm^{-1} (Fig. 6, spectrum a). Upon outgassing at 298 K most of the water is removed (Fig. 6, spectrum b) and the resulting spectrum displays an intense OH band at 3673 cm^{-1} and NH$_2$ bands at 3508 and 3401 cm^{-1}, these frequencies being similar to those observed with samples evacuated at temperatures higher than 423 K. Note, however, that the band characterizing structural hydroxyls is of lower intensity as compared to the UiO-66 sample,

as already reported [31].

Although with very low intensity, the combination mode of water at ca. 5250 cm^{-1} is still noticed, which indicates the retaining of very small amount of water. Further evacuation at 443 K (Fig. 6, spectrum c) leads to disappearance of a broad feature centered around 3250 cm^{-1} and decrease in intensity of the OH band without substantial change in position. Thus, the results confirm that the DMF affects the OH and NH$_2$ groups and the changes in the first set of experiments were largely due to its removal.

3.2.3. Deuteration

Due to the relatively high light scattering with the UiO-66, leading to enhanced noise in the OH stretching region, the adsorption experiments with this sample were performed with partially deuterated sample. Thus, we were able to exploit the spectra in the OD region in order to make unambiguous conclusions.

As expected, partial deuteration of the material led to erosion of the hydroxyl bands and appearance, at their expense, of O-D bands. In
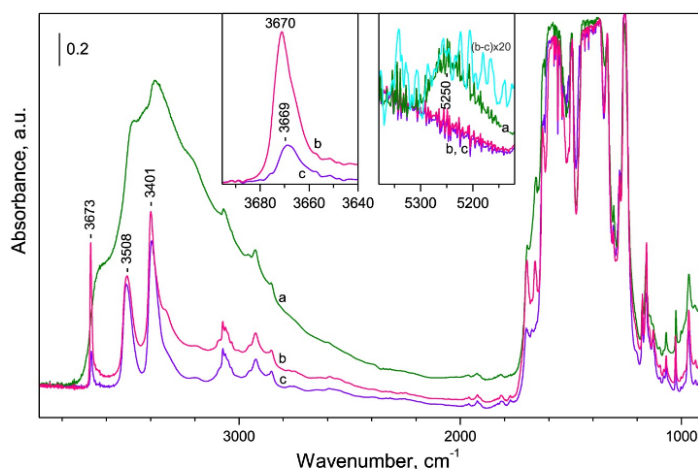
Fig. 6. FTIR spectra of DMF-free UiO-66-NH$_2$ (evacuated at 443 K), in presence of water (a) and subsequent evacuation at 298 K (b) and at 443 K (c).

particular, the band at 3674 cm^{-1} was shifted to 2709 cm^{-1}. The isotopic shift factor (1.356) is slightly lower than the theoretical value (1.374) but is consistent with experimental observations [42].

3.2.4. Changes in the background spectra at low temperature

To assess surface acidity, we used several probe molecules. Two of them, CO and N$_2$, are weak bases and therefore were adsorbed at low temperature. However, temperature affects the exact positions and even the shape of the IR bands. Therefore, to know the reference wavenumber, one should know the spectra at low temperature before adsorption of probe molecules. Details are provided in the SI (Fig. S4) and here we underline the following key observations:

- The ν(OH) band at 3673 cm^{-1} (sample UiO-66) is split into two components, at 3676 and 3669 cm^{-1}.
- The ν(OH) band at 3677 cm^{-1} (sample UiO-66-NH$_2$ evacuated at 298 K) is also split (bands at 3682 and 3677 cm^{-1}) while the band of the sample evacuated at 473 K seems to be blue shifted (from 3699 to 3672 cm^{-1}).
- Complex changes/shifts occur with the NH$_2$ stretching modes.

3.2.5. Intrinsic frequency of the OH groups

It was recently reported that the OH stretching frequencies of hydroxyl groups in porous materials as MOFs are slightly red shifted as a result of weak H-bonding [40]. Thus, the shift observed after adsorption of molecular probes appears to be additional and not fully indicative of the OH acidity. However, based on the results observed with two different probes it is possible to estimate the intrinsic OH frequency. The details are reported elsewhere [40] and schematic presentation is given on Fig. S5. Note that some small deviations from the real values can exists due to the fact that the preexisting H-bond could be partly preserved after interaction between the hydroxyl and the probe molecule. Based on the CO and N$_2$ adsorption experiments, the intrinsic frequency of the OH groups in UiO-66 was estimated to be ca. 3682 cm^{-1}. All adsorption-induced shifts, $\Delta_t\nu$(OH), are therefore calculated on the basis of this wavenumber.

3.3. Adsorption of CO

CO is one of the most used IR probe molecules for testing surface acidity and, in particular, the acidity of hydroxyl groups [43,44]. Formation of OH–CO adducts leads to a red shift of the ν(OH) modes and the absolute value of this shift correlates with the hydroxyl acidity. Due

to the weak interaction, the measurements are performed at low temperature.

3.3.1. UiO-66

As already noted, these experiments were performed with partially (ca. 50%) deuterated sample. Fig. 7A depicts the changes in the ν(OH) region occurring after low-temperature CO adsorption on the sample evacuated at ambient temperature. The respective changes in the ν(OD) region are shown in Fig. 7B. Considering the OH region, the main effect of CO admission at low coverage is the shift of the band at 3676 cm^{-1} (negative feature) to 3599 cm^{-1} (positive feature). Thus, the measured shift of ν(OH) appears to be −77 cm^{-1}. This shift is intermediate between the earlier reported values of −83 cm^{-1} [6] and −69 cm^{-1} [39]. Using the intrinsic OH frequency as a reference, the shift value, $\Delta_t\nu_{OH}$, is −83 cm^{-1}, which indicates a low acidity of the hydroxyls. For comparison, the band of silica SiOH groups is shifted upon adsorption of CO by ca. −90 cm^{-1} [42].

A careful inspection of the spectra (including comparison with the OD region) reveals a shoulder of the OH band at 3670 cm^{-1} that is also shifted. In addition, a shoulder at 3589 cm^{-1} is observed with the shifted band. However, there is no correlation between the intensities of the two shoulder bands at 3670 and 3589 cm^{-1}.

In the ν(CO) region (the inset in Fig. 7A) a band at 2153 cm^{-1} develops in parallel with the erosion of the ν(OH) band and is therefore associated with OH–CO interaction. At high coverage weakly (physically) adsorbed CO is monitored by two bands, at 2136 and 2132 cm^{-1}.

Similar results were obtained with the sample activated at 473 K. However, one important difference should be underlined. The shifted band has a well pronounced additional shoulder at 3574 cm^{-1}. Since no other negative band was detected in the spectra, the results suggest the existence of two families of OH groups coinciding in frequency but differing in acidity. For the more acidic hydroxyls the shift of the OH modes appears to be −108 cm^{-1}. Comparison between spectra at similar CO coverages obtained with samples activated at 298 and 473 K clearly shows that the more acidic OH species have been created during sample activation at 473 K and have not existed on the material evacuated at 298 K.

The carbonyl band in this case was detected at 2154 cm^{-1} (see the inset in Fig. 7C). A very weak feature around 2180 cm^{-1} could be associated with negligible amount of Lewis acid sites. Separate experiments indicated that the band did not increase with the activation temperature and was hardly observed with a dehydroxylated sample evacuated at 573 K.
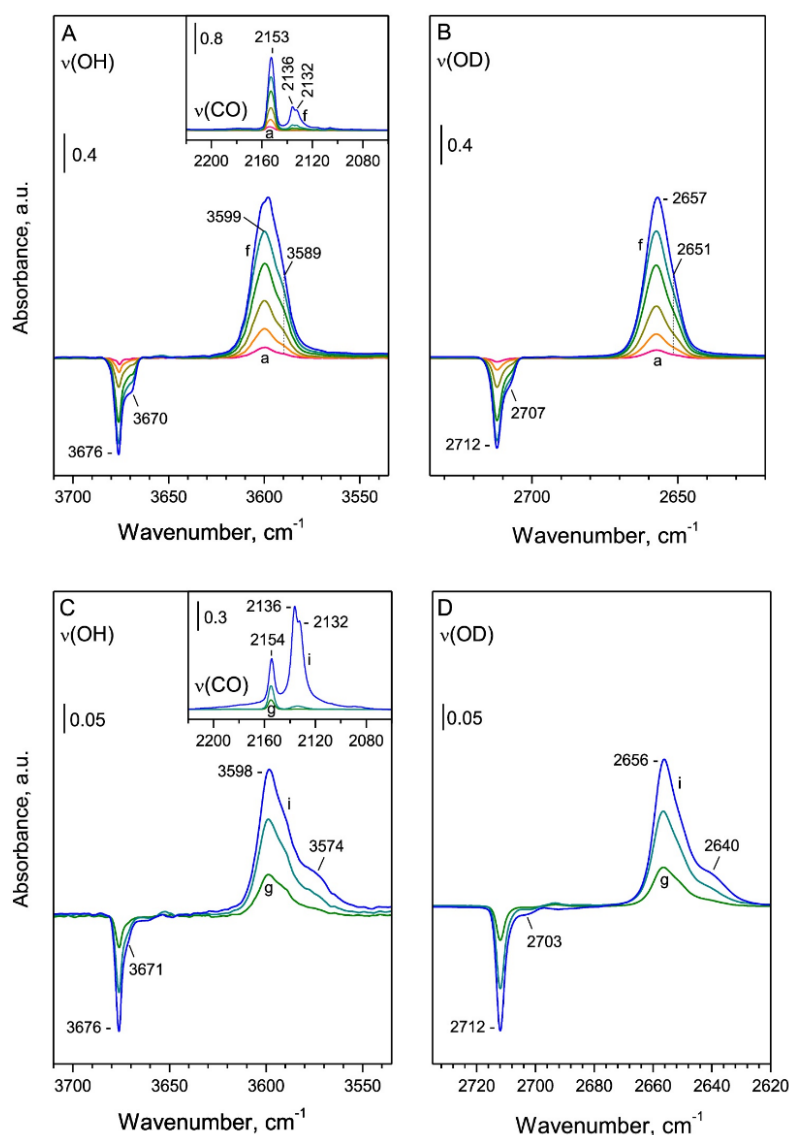
114

Fig. 7. FTIR spectra registered after low temperature CO adsorption on partly deuterated UiO-66 evacuated at 298 K (panels A, B) and at 473 K (panels C, D). The spectra (a)–(f) and (g)–are registered after introduction of increasing amounts of CO into the IR cell.

We also note the significantly enhanced intensity of the bands due to physically adsorbed CO. Finally, bands of very weak intensity were detected at 2126 and 2105 cm^{-1}. They are assigned to O-bonded CO and to OH$-^{13}$CO, respectively [39,42].

At high CO coverages the bands characterizing H-bonded hydroxyls shift additionally (spectra not shown) which is due to solvation of the OH/OD groups. Note that the effect was not observed with the sample activated at ambient temperature which suggests steric limitations and probably small pore volume.

3.3.2. UiO-66-NH$_2$

Here we shall initially compare the properties of the samples after evacuation at ambient temperature and 473 K.

Upon dosing of CO to the sample evacuated at ambient temperature a carbonyl band at 2146 cm^{-1} develops. Simultaneously, the OH band at 3677 cm^{-1} is eroded and a new well shaped band at 3608 cm^{-1} emerges instead (Fig. 8A). Thus, the total shift of the OH modes appears to be $-74 cm^{-1}$. This is slightly lower as compared to the results obtained with the amino-free sample. With coverage increase a component of the band at 3663 cm^{-1} is also eroded and CO stretching frequency is slightly shifted. At high coverages a band at 2136 cm^{-1}, assigned to physically adsorbed CO develops. At these stages the NH bands are also affected but these changes are negligible.

When CO was dosed to the sample activated at 473 K, the band of the μ_3-hydroxyls was first affected (Fig. 8B). The exact position of the negative band is 3672 cm^{-1}. Simultaneously, a new band at 3584 cm^{-1}
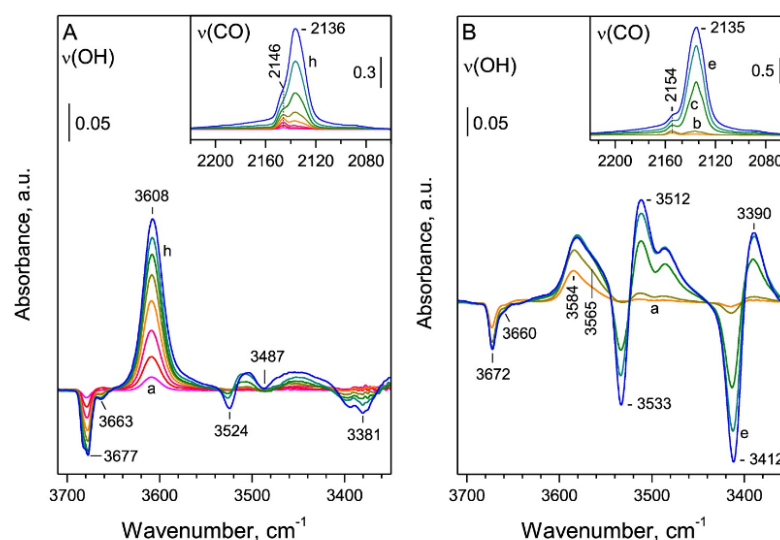
Fig. 8. FTIR spectra registered after low temperature CO adsorption on UiO-66-NH$_2$ evacuated at 298 K (panel A) and at 473 K (panel B). The spectra (a)–(h) are registered after introduction of increasing amounts of CO into the IR cell up to 5 mbar equilibrium pressure.

with a low-frequency shoulder at 3565 cm^{-1} developed. In the carbonyl region a band at 2154 cm^{-1} was detected. The total shift of the OH modes is $\Delta_t\nu = -98$ cm^{-1} and $\Delta_t\nu = -117$ cm^{-1} for the shoulder. Therefore, all of the OH groups in the 473 K activated sample are characterized by a higher acidity as compared to the case with the sample evacuated at ambient temperature. We recall that, with UiO-66, only a small fraction of the hydroxyls were characterized by enhanced acidity.

Further increase in the CO coverage leads to affecting the NH$_2$ bands as well (Fig. 8B). Note that with sample activated at ambient temperature the effect was hardly observed, most probably due to the fact that the NH$_2$ groups were engaged in interaction with DMF. These results could suggest a measurable acidity of the NH$_2$ groups. However, because of some peculiarities, we offer another explanation which will be described below (see N$_2$ adsorption on sample evacuated at 473 K).

The CO stretching frequency, ν(CO), is expected to correlate with the acidity of hydroxyls: the higher the acidity, the higher ν(CO). However, there are deviations from this correlation with porous materials which are due to dual interaction [42]. In this light, it seems that the position of the carbonyl band at 2146 cm^{-1}, observed with the sample evacuated at 298 K, is to some extent determined by dual interaction of CO with the material.

In order to obtain information to which extent the increase of the acidity of the OH groups is due to the removal of DMF we studied the CO adsorption on re-hydrated (DMF-free) sample. Note that this was not essential for UiO-66 because of the low amount of residuals. The results are summarized in Fig. 9. It is seen that the acidity of the OH groups ($\Delta_t\nu = -91$ cm^{-1}) is slightly higher than the acidity observed with the sample evacuated at 298 K. The acidity increases when the sample is evacuated at 473 K ($\Delta_t\nu = -99$ cm^{-1}).

3.4. Adsorption of N$_2$

Another widely used probe molecule for measuring surface acidity is N$_2$ [29,33]. Dinitrogen is a weaker base than CO (PA of N$_2$ is 493.8 kJ mol^{-1} vs. 594 kJ mol^{-1} for CO). Consequently, the N$_2$-induced shift of the ν(OH) modes is considerably smaller (ca. 2.8 times as measured for silica silanol groups [45,46]). However, the OH groups in porous materials are normally involved in weak H-bonding with the

walls. Upon interaction with basic molecules the preexisting bond is broken or considerably weakened. Therefore, the measured shift is only additional and does not give correct information on the acidity of the hydroxyls. To overcome this difficulty, it was recently proposed [40] that the combined use of two probe molecules (CO and N$_2$) allows estimation of the intrinsic frequency of the hydroxyls. Based on this approach we estimated the intrinsic frequency of the UiO-66 OH groups to be 3682 cm^{-1}. This value is, as expected, slightly higher from the measured one.

3.4.1. UiO-66

The results obtained after N$_2$ adsorption on our UiO-66 sample are summarized in Fig. 10 and are consistent with the CO adsorption results. The adsorption-induced shifts of the OH stretching modes are also presented in Table 1.

Adsorption of N$_2$ on the sample evacuated at ambient temperature results in a shift of the 3676 cm^{-1} OH band to 3652 cm^{-1} ($\Delta_t\nu = -30$ cm^{-1}). A shoulder at 3669 cm^{-1} is also shifted to the same value. The results confirm that the shoulder is due to the same OH groups that are involved into a very weak H-bonding. Complexation with dinitrogen breaks this bond and the final shifted OH band is at the same frequencies as with the 3676 cm^{-1} groups. In parallel with these changes, a band at 2328 cm^{-1}, attributed to the N−N modes of dinitrogen reacting with hydroxyl groups, is detected. A shoulder of this band around 2326 cm^{-1} is also discernible and will be discussed later on.

The results with the sample activated at 473 K are similar (Fig. 10B). In this case two peculiarities, consistent with the CO adsorption results, should be mentioned:

- The shift of the OH modes (acidity) is negligibly larger ($\Delta_t\nu = -31$ cm^{-1}).
- A fraction of the hydroxyls are characterized by a higher acidity ($\Delta_t\nu = -42$ cm^{-1}).

Another important difference is that a pronounced band at 2324 cm^{-1} is detected in the N−N region. It is characterized by a weak stability, consistent with the low stretching frequency. This band cannot be due to N$_2$ coordinated to open metal sites (separate
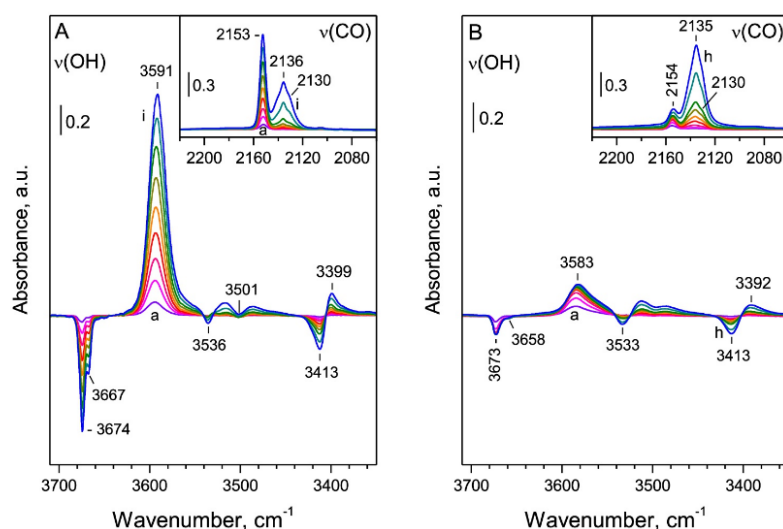
Fig. 9. FTIR spectra registered after low temperature CO adsorption on DMF-free UiO-66-NH$_2$: evacuated at 298 K (panel A) and at 473 K (panel B). The spectra (a)–(i) are registered after introduction of increasing amounts of CO into the IR cell.

experiments indicated that Zr^{4+}-N$_2$ complexes are detected at 2337 cm^{-1}). N$_2$ is a homo-nuclear molecule and therefore is not polar. However, it can be polarized by positively and negatively charged centers. Therefore, we hypothesize that the band at 2324 cm^{-1} is due to N$_2$ polarized by O^{2-} basic sites created during sample activation. Similar adsorption sites were earlier proposed for adsorption of another homonuclear diatomic molecule, H$_2$ [10].

3.4.2. UiO-66-NH$_2$

The results on N$_2$ adsorption on UiO$_2$-66-NH$_2$ are consistent with the above observation (see Fig. 11, Table 1 and Fig. S6). In order to obtain a deeper insight into the phenomena, we have studied N$_2$ adsorption on re-hydrated samples. To obtain better quality spectra in the N−N region, for these experiments we used ^{15}N$_2$.

The hydroxyl bands at 3674 and 3668 cm^{-1}, detected with the sample evacuated at 298 K, are shifted upon ^{15}N$_2$ adsorption to 3648 cm^{-1} (Fig. 11A). Thus, the $\Delta_t\nu$ is −34 cm^{-1}. A larger shift, i.e. $\Delta_t\nu = -38$ cm^{-1} is observed with the sample evacuated at 473 K (Fig. 11B). Noticeable, a strong band at 2246 cm^{-1} is registered with the sample evacuated at 473 K (see the inset in Fig. 11B). Clearly, this band is not related to OH−^{15}N$_2$ interaction. The band is analogue of the ^{14}N$_2$ band at 2324 cm^{-1}. It was already suggested that it is due to N$_2$ polarized by O^{2-} basic sites. Thus, it seems that, with this sample again, basic sites are created during evacuation at elevated temperatures.

It is also to be noted that difference spectra indicate that N−H bands are also affected by dinitrogen adsorption which could indicate some acidity of the NH$_2$ groups [48]. However, we will propose another explanation of this phenomenon in the Discussion section.

3.5. Adsorption of CD$_3$CN

To complete the picture on the acidity of UiO-66 and UiO-66-NH$_2$ hydroxyls, we studied the adsorption of CD$_3$CN. Acetonitrile is a small molecule with a relatively high proton affinity (779.2 kJ mol^{-1}), higher than the proton affinity of H$_2$O (691 kJ mol^{-1} [49]). Therefore, it can replace pre-adsorbed water. Typically, CD$_3$CN is not protonated and one can usually distinguish between the complexes formed with OH groups (ν_{CN} at 2300-2285 cm^{-1}) and with Lewis acid sites (ν_{CN} up to 2330 cm^{-1}) [50]. Due to the rather strong interaction, the experiments

are performed at ambient temperature.

3.5.1. UiO-66

Briefly, adsorption of CD$_3$CN on the UiO-66 sample evacuated at 293 K leads to its interaction with the principal hydroxyls (observed at 3673 cm^{-1} at this temperature) which results in a shift of the OH modes by −227 cm^{-1} (Fig. 12). As expected, with the sample activated at higher temperatures, the acidity of the hydroxyls slightly increases. However, the appearance of different bands is not resolved as in the case of CO and N$_2$ adsorption experiments.

Consider now the CN stretching region. Interestingly, adsorption of CD$_3$CN clearly revealed the existence of Lewis acid sites (Zr^{4+}) on the sample evacuated at 473 K through a ν(CN) band at 2299 cm^{-1} (Fig. 12, spectrum c). The amount of these sites was higher with a sample evacuated at 523 K (Fig. 12, spectrum c). A careful inspection of the spectra indicates negligible amount of Lewis acid sites even with the sample evacuated at ambient temperature. Subsequent re-hydroxylation results in a substantial decrease of the number of detected Lewis acid sites, their amount being only slightly larger as compared to the sample evacuated at ambient temperature. Therefore, we can conclude that the Lewis acid sites are formed as a result of sample dehydroxylation and the process is almost fully reversible.

Note that no Lewis acid sites were detected by CO and N$_2$ as probe molecules. This observation indicates that CD$_3$CN, being a relatively strong base, is able to cause some re-arrangement in the Zr^{4+} first coordination sphere.

3.5.2. UiO-66-NH$_2$

The spectra of CD$_3$CN adsorbed on UiO-66-NH$_2$ are presented in Fig. 13. In this case the acidity of the hydroxyls is difficult to estimate because of the superimposition of the O−H and N−H bands. Here again, Lewis acid sites develop with the activation temperature and almost disappear after re-hydroxylation.

4. Discussion

4.1. Hydroxylation/dehydroxylation process and Lewis acidity

A unique property of the Zr$_6$ node-based MOF materials is their fully
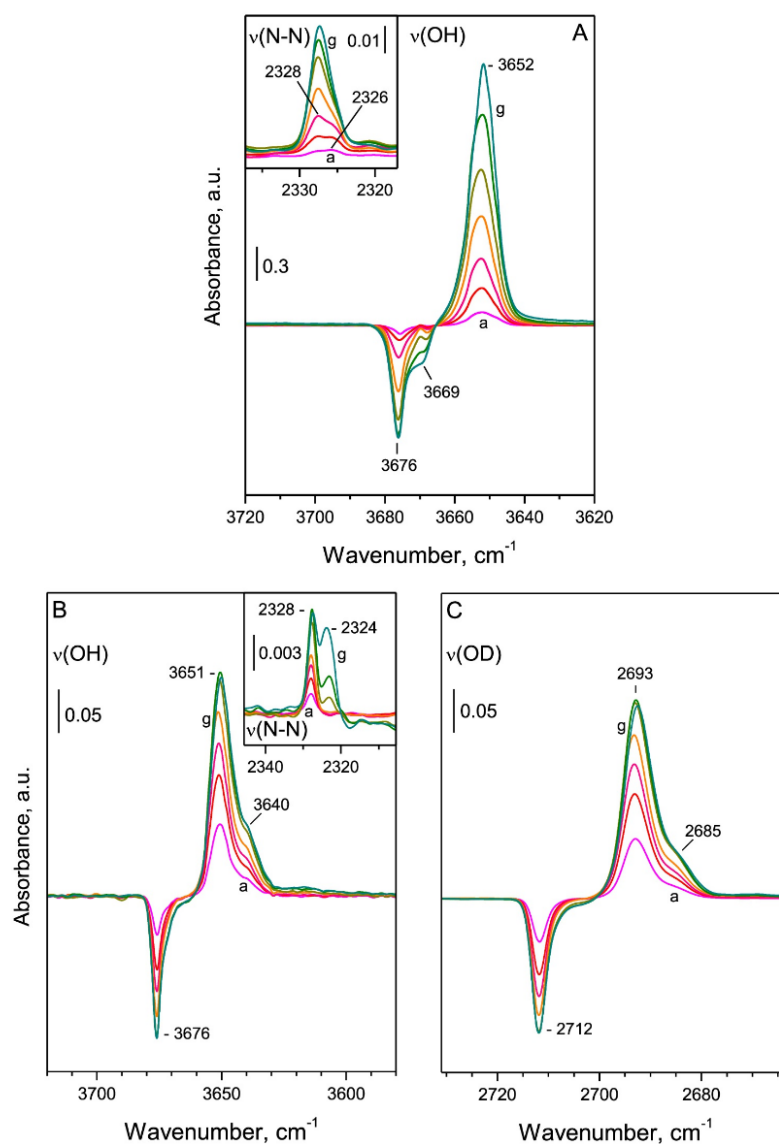
117

Fig. 10. FTIR spectra of N_2 adsorbed on UiO-66. Sample evacuated at 298 K (panel A) and at 473 K (partly deuterated sample, panels B and C). The spectra (a)–(g) are registered after introduction of increasing amounts of N_2 into the IR cell.

reversible dehydroxylation. Due to the flexibility in the coordinative state of Zr^{4+} species, it is possible to have both, the hydroxylated and dehydroxylated forms. According to theoretical predictions by Valenzano at al. [9], upon activation of Zr-MOFs at high temperature, the $Zr_6(\mu_3\text{-O})_4(\mu_3\text{-OH})_4$ cluster is able to lose two water molecules, leading to a distorted $Zr_6(\mu_3\text{-O})_6$ cluster with the Zr−O coordination numbers reduced from 8 to 7. In this way no oxygen vacancies and respectively no coordinatively unsaturated (c.u.s.) Zr^{4+} sites are formed. This "no O-vacancy" model of dehydroxylation was accepted by many researchers. Therefore, according to this model, open Zr sites can be associated exclusively with missing linker defects. Indeed, Driscoll et al. [22] reported a correlation between the loss of the organic linkers and the amount of open Zr sites (as detected by CO).

However, the experiments were performed after high evacuation temperature (above 723 K). Other authors [7] associate formation of c.u.s. Zr^{4+} ions with the dehydroxylation process of the inorganic cluster. Based on theoretical investigation, Hajek et al. [51] also proposed creation of Lewis sites as a result of sample dehydroxylation.

Our results on the CO adsorption experiments are in favor of the "no O-vacancy" hypothesis because no Zr^{4+} Lewis acid sites were detected by CO on the dehydrated samples (evacuated up to 573 K). However, the experiments with CD_3CN as a probe molecule clearly revealed creation of Lewis acid sites in parallel with the sample dehydroxylation as well as their disappearance upon re-hydroxylation of the cluster. Therefore, these results indicate that dehydroxylation leads to creation of c.u.s. Zr^{4+} sites.

K. Chakarova, et al.

Table 1
CO and N_2-induced shifts, $\Delta_t\nu(OH)$, of the O−H stretching modes of the μ_3-OH groups in UiO-66 and UiO-66-NH_2. The shifts are calculated on the basis of intrinsic frequency of $3682\,cm^{-1}$.

Sample	CO induced total shift, $\Delta_t\nu_{OH}$, cm^{-1}	N_2 induced total shift, $\Delta_t\nu_{OH}$, cm^{-1}
UiO-66 activated at 298 K	− 83	− 30
	− 93	n.r.[a]
UiO-66 activated at 473 K	− 84	− 31
	− 93	n.r.
	− 108	− 42
UiO-66-NH_2 activated at 298 K	− 74	− 30
UiO-66-NH_2, rehydrated, activated at 298 K	− 91	− 34
UiO-66-NH_2 activated at 473 K	− 98	− 38
	− 117	− 49

[a] Not resolved.

This contradiction can be explained by the following hypothesis. Partial and full dehydroxylation of the $Zr_6(\mu_3-O)_4(\mu_3-OH)_4$ cluster does not lead to creation of open metal sites as predicted by Valenzano at al [9]. Consequently, no Lewis acidity can be detected by probe molecules of weak basicity (CO and N_2). However, relatively strong bases, as CD_3CN, induce structural changes in the dehydroxylated Zr-node by making strong coordination bond with the Zr^{4+} sites. Therefore, this "hidden" Lewis acidity will always be present when a molecule with enough high basicity is introduced to the system. This observation is particularly important for catalysis based on Lewis acidity.

Interestingly, with another UiO-66 sample with missing linker defects and evacuated at 473 K, we have detected Lewis acid sites by CO adsorption (details not reported here).

4.2. Acidity and population of hydroxyl groups

Consider first the UiO-66 sample. Our results indicate that upon dehydroxylation the acidity of the hydroxyls increases. Therefore, we can conclude that distorted Zr-node is characterized by hydroxyls with enhanced acidity. We can speculate that the acid properties of the hydroxyls are connected with the ability of the whole Zr-node to participate in electron transfer. With fully hydroxylated sample this ability is
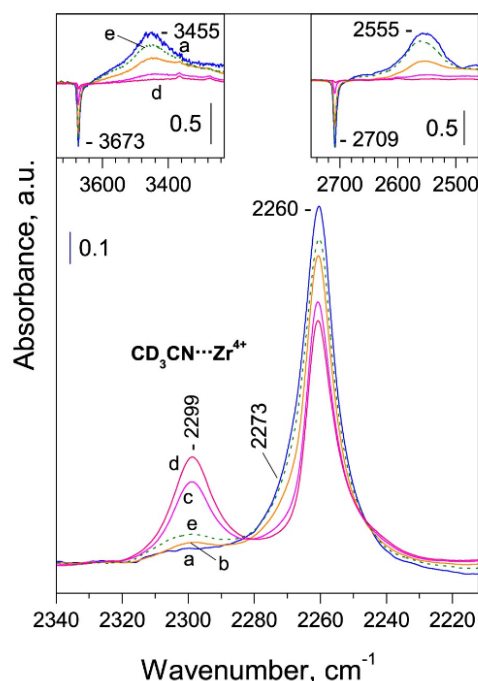

Fig. 12. FTIR spectra of CD_3CN (10 mbar equilibrium pressure) adsorbed on UiO-66. Samples evacuated at 298 K (a), 423 K (b), 473 K (c) and 573 K (d). Spectrum (e) (dotted line) refers to re-hydroxylated sample evacuated at 298 K.

distributed to more OH groups and, as a result, they demonstrate lower acidity. At the same time the OH stretching frequency remains practically unaffected which indicates the local geometric structure is preserved, i.e. the hydroxyls are of μ_3–OH type.

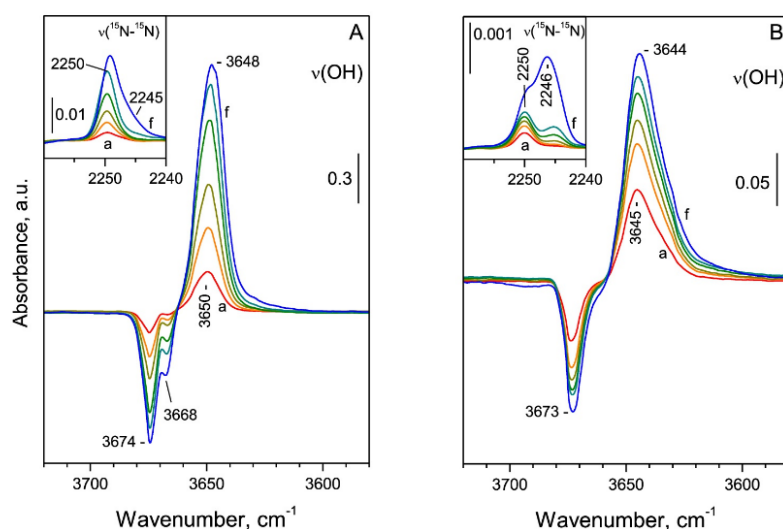In agreement with earlier reports [42], we observed that, in general,

Fig. 11. FTIR spectra of $^{15}N_2$ adsorbed on re-hydroxylated UiO-66-NH_2. Sample evacuated at 298 K (left) and at 473 K (right). The spectra (a)–(f) are registered after introduction of increasing amounts of $^{15}N_2$ into the IR cell.
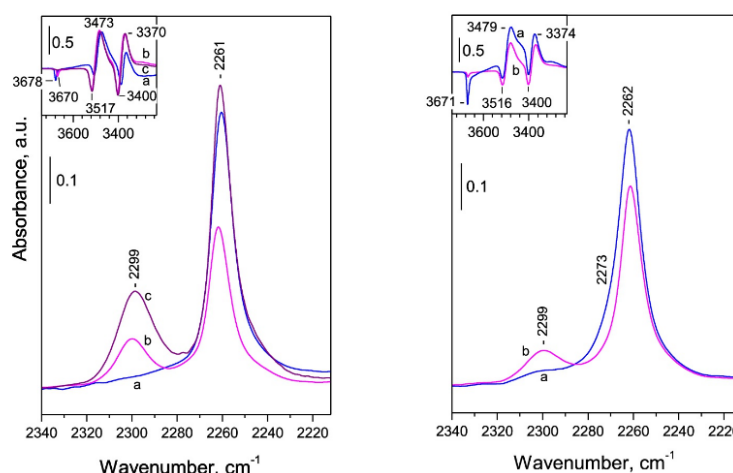
119

Fig. 13. FTIR spectra of CD$_3$CN (10 mbar equilibrium pressure) adsorbed on UiO-66-NH$_2$. Panel A: sample evacuated at 298 K (a), 473 K (b) and 523 K (c). Panel B: re-hydroxylated sample evacuated at 298 K (a) and at 473 K (b).

Table 2
Values of ν(OH) of hydroxyl groups in different MOFs, CO-induced shift of ν(OH) modes and ν(CO) of adsorbed CO.

MOF	ν(OH), cm^{-1}	$\Delta\nu$(OH), cm^{-1}	ν(CO), cm^{-1}	Ref.
UiO-66	3676	$-77, -87, -102$	2154–2153	this work
	3670	$-71, -96$		
UiO-66	3674	-83	2155	[6]
UiO-66	3674	-69	2152	[39]
UiO-66-NH$_2$	3674	$-83, -91$	2154–53	this work
	3667	-67		
MIL-53(Al)	3721	-45	2146	[40]
	3711	-42		
MIL-53(Al)-NH$_2$	3683	-23	2141, 2135	[40]
MIL-100(Fe)	3705	-105	2157	[52]
	3685	-170	2157	
MIL-100(Cr)	3585	-90		[53]
MIL-100(Al)	3588	$-86, -78$		[54]
MIL-101(Al)	3708	-48		[55]
$-$NH$_2$	3682	0		
MIL-126(Fe)	3670	-75	–	[56]
STA-26	3674	-69	2149	[57]
STA-27	3669	-40	2143	[58]

the acidity of the structural hydroxyls of both, hydroxylated and de-hydroxylated sample, is rather low. For comparison, the highest reported CO-induced shift of OH modes, observed with zeolites, amounts to -440 cm^{-1} [42]. Table 2 compares the CO-induced shifts of the OH stretching modes of hydroxyl groups in different MOFs. It is seen that the highest acidity was reported for OH groups in MIL-100(Fe): $\Delta\nu$(OH) of -105 and -170 cm^{-1}. However, the authors have not unambiguously attributed the OH bands to isolated hydroxyls. Comparison with other samples indicates that dehydroxylated UiO-66 (measured shift of -102 cm^{-1}) demonstrates the highest protonic acidity.

Similar results were observed with the UiO-66-NH$_2$ sample. However, contrary to the general expectations, introduction of NH$_2$ groups leads to a small but measurable increase in the acidity of the structural hydroxyls.

4.3. Basic sites

An interesting observation in this work is the creation, upon thermal treatment, of new kind of sites which were attributed to c.u.s. O^{2-} anions. These were monitored by a band at ca. 2325 cm^{-1} of adsorbed

N$_2$ (2246 cm^{-1} for ^{15}N$_2$). We were not able to establish a correlation between the number of these sites and the number of c.u.s. Zr^{4+} ions. In any case, these sites could be important for adsorption of some gases, as already proposed for H$_2$ [10]. We note that basic sites could be involved in the adsorption of acidic molecules, e.g. CO$_2$. The next part of our study will be devoted to CO$_2$ adsorption sites.

It is of interest to discuss whether the basic sites are monitored by CO. It is reported that, with strongly basic sites CO can form CO$_2$$^{2-}$ carbonite structures [59,60]. The latter are characterized by a set of IR bands at 1485-1225, 890-850 and 745-715 cm^{-1}. Although bands around 1400 cm^{-1} can be masked by the strong absorbance of the MOF linker, by analyzing the whole spectral region we have not found indications of formation of carbonite structures. Therefore, we conclude on the absence of strongly basic sites in our sample. It seems probable that the CO analogue of this adsorption form is observed in the region of physically adsorbed CO (2140-2130 cm^{-1}), where CO bonded to O^{2-} sites has been reported to absorb [47]. This is consistent with the noted differences in this region when CO was adsorbed on samples activated at different temperatures. Indeed, these bands developed with increasing sample activation temperature.

4.4. Role of NH$_2$ groups

A measurable acidity of the positively charged ammonium cations in zeolites was recently reported [48], but one cannot expect considerable acidity of NH$_2$ groups. We note that formation of NH··CO adducts should indeed lead to decrease in the NH frequency. At the same time, increase in the total intensity of the band should be observed. However, this was not detected in our case. In addition, the adsorption induced shift should depend on the basicity of the adsorbed molecule. The results presented in Fig. S7 clearly show that the CO and N$_2$-induced shifts of the N$-$H modes practically coincide. Interestingly, the amount of affected NH groups seems to correlate with the hydroxylation degree of the sample. All this imply that the shift of the N$-$H band is not related to acidity of the NH$_2$ groups. A possible explanation of the phenomenon is coordination of CO and N$_2$ to basic site. Unfortunately, at this stage we cannot offer more details on the interaction.

5. Conclusions

● Functionalization of UiO-66 with $-$NH$_2$ groups slightly affects the

acid and basic sites of the MOF. This is due to the fact that these sites are associated with the inorganic cluster of the material.

- UiO-66 and UiO-66-NH$_2$ samples are reversibly dehydroxylated. The decrease of the population of the hydroxyls leads to increase in their acidity.
- The hydroxyls of UiO-66-NH$_2$ are slightly more acidic as compared to UiO-66.
- Sample dehydroxylation leads to creation of Zr^{4+} Lewis acid sites detectable by relatively strong bases, as CD$_3$CN.
- Basic sites (coordinatively unsaturated O^{2-}) are also formed during dehydroxylation and can be detected with N$_2$ as a probe molecule.
- The NH$_2$ groups in UiO-66-NH$_2$ do not manifest any acidity. However, they are affected by adsorbed molecules.

Acknowledgments

Appendix A. Supplementary data

Supplementary data to this article can be found online at https://doi.org/10.1016/j.micromeso.2019.03.006.

References

[1] J.-R. Li, Y. Ma, M.C. McCarthy, J. Sculley, J. Yu, H.-K. Jeong, P.B. Balbuena, H.-C. Zhou, Carbon dioxide capture-related gas adsorption and separation in metal-organic frameworks, Coord. Chem. Rev. 255 (2011) 1791–1823.

[2] Q. Wang, J. Luo, Z. Zhong, A. Borgna, CO$_2$ capture by solid adsorbents and their applications: current status and new trends, Energy Environ. Sci. 4 (2011) 42–55.

[3] S. Couck, J.F.M. Denayer, G.V. Baron, T. Rémy, J. Gascon, F. Kapteijn, An amine-functionalized MIL-53 metal−organic framework with large separation power for CO$_2$ and CH$_4$, J. Am. Chem. Soc. 131 (2009) 6326–6327.

[4] J.M. Cavka, S. Jakobsen, U. Olsbye, N. Guillou, C. Lamberti, S. Bordiga, K.P. Lillerud, A new zirconium inorganic building brick forming metal organic frameworks with exceptional stability, J. Am. Chem. Soc. 130 (2008) 13850–13851.

[5] F. Vermoortele, R. Ameloot, A. Vimont, C. Serre, D. De Vos, An amino-modified Zr-terephthalate metal–organic framework as an acid–base catalyst for cross-aldol condensation, Chem. Commun. 47 (2011) 1521–1523.

[6] A.D. Wiersum, E. Soubeyrand-Lenoir, Q. Yang, B. Moulin, V. Guillerm, M.B. Yahia, S. Bourrelly, A. Vimont, S. Miller, C. Vagner, M. Daturi, G. Clet, C. Serre, G. Maurin, P.L. Llewellyn, An evaluation of UiO-66 for gas-based applications, Chem. Asian J. 6 (2011) 3270–3280.

[7] F. Ragon, B. Campo, Q. Yang, C. Martineau, A.D. Wiersum, A. Lago, V. Guillerm, C. Hemsley, J.F. Eubank, M. Vishnuvarthan, F. Taulelle, P. Horcajada, A. Vimont, P.L. Llewellyn, M. Daturi, S. Devautour-Vinot, G. Maurin, C. Serre, T. Devic, G. Clet, Acid-functionalized UiO-66(Zr) MOFs and their evolution after intra-framework cross-linking: structural features and sorption properties, J. Mater. Chem. A 3 (2015) 3294–3309.

[8] S. Chavan, J.G. Vitillo, M.J. Uddin, F. Bonino, C. Lamberti, E. Groppo, K.-P. Lillerud, S. Bordiga, Functionalization of UiO-66 metal-organic framework and highly cross-linked polystyrene with Cr(CO)$_3$: in situ formation, stability, and photoreactivity, Chem. Mater. 22 (2010) 4602–4611.

[9] L. Valenzano, B. Civalleri, S. Chavan, S. Bordiga, M.H. Nilsen, S. Jakobsen, K.P. Lillerud, C. Lamberti, Disclosing the complex structure of UiO-66 metal organic framework: a synergic combination of experiment and theory, Chem. Mater. 23 (2011) 1700–1718.

[10] S. Chavan, J.G. Vitillo, D. Gianolio, O. Zavorotynska, B. Civalleri, S. Jakobsen, M.H. Nilsen, L. Valenzano, C. Lamberti, K.P. Lillerud, S. Bordiga, H$_2$ storage in isostructural UiO-67 and UiO-66 MOFs, Phys. Chem. Chem. Phys. 14 (2012) 1614–1626.

[11] G.C. Shearer, S. Forselv, S. Chavan, S. Bordiga, K. Mathisen, M. Bjørgen, S. Svelle, K.P. Lillerud, In situ infrared spectroscopic and gravimetric characterisation of the solvent removal and dehydroxylation of the metal organic frameworks UiO-66 and UiO-67, Top. Catal. 56 (2013) 770–782.

[12] S. Øien, G. Agostini, S. Svelle, E. Borfecchia, K.A. Lomachenko, L. Mino, E. Gallo, S. Bordiga, U. Olsbye, K.P. Lillerud, C. Lamberti, Probing reactive platinum sites in UiO-67 zirconium metal-organic frameworks, Chem. Mater. 27 (2015) 1042–1056.

[13] R. Ameloot, M. Aubrey, B.M. Wiers, A.P. Gómora-Figueroa, S.N. Patel, N.P. Balsara, J.R. Long, Ionic conductivity in the metal–organic framework UiO-66 by dehydration and insertion of lithium tert-butoxide, Chem. Eur J. 19 (2013) 5533–5536.

[14] M. Kandiah, S. Usseglio, S. Svelle, U. Olsbye, K.P. Lillerud, M. Tilset, Post-synthetic modification of the metal–organic framework compound UiO-66, J. Mater. Chem.

[15] J.B. DeCoste, G.W. Peterson, B.J. Schindler, K.L. Killops, M.A. Browe, J.J. Mahle, The effect of water adsorption on the structure of the carboxylate containing metal–organic frameworks Cu-BTC, Mg-MOF-74, and UiO-66, J. Mater. Chem. A 1 (2013) 11922–11932.

[16] M.N. Timofeeva, V.N. Panchenko, J.W. Junc, Z. Hasanc, M.M. Matrosova, S.H. Jhung, Effects of linker substitution on catalytic properties of porous zirconium terephthalate UiO-66 in acetalization of benzaldehyde with methanol, Appl. Catal. Gen. 471 (2014) 91–97.

[17] C.L. Luu, T.T. Van Nguyen, T. Nguyen, T.C. Hoang, Synthesis, characterization and adsorption ability of UiO-66-NH$_2$, Adv. Nat. Sci. Nanosci. Nanotechnol. 6 (2015) 025004.

[18] D. Yang, S.O. Odoh, T.C. Wang, O.K. Farha, J.T. Hupp, C.J. Cramer, L. Gagliardi, B.C. Gates, Metal−organic framework nodes as nearly ideal supports for molecular catalysts: NU-1000- and UiO-66-supported iridium complexes, J. Am. Chem. Soc. 137 (2015) 7391–7396.

[19] M. Kandiah, M.H. Nilsen, S. Usseglio, S. Jakobsen, U. Olsbye, M. Tilset, C. Larabi, E.A. Quadrelli, F. Bonino, K.P. Lillerud, Synthesis and stability of tagged UiO-66 Zr-MOFs, Chem. Mater. 22 (2010) 6632–6640.

[20] G.W. Peterson, J.J. Mahle, J.B. De Coste, W.O. Gordon, J.A. Rossin, Extraordinary NO$_2$ removal by the metal-organic framework UiO-66-NH$_2$, Angew. Chem. Int. Ed. 55 (2016) 6235–6238.

[21] F. Zhang, S. Zheng, Q. Xiao, Y. Zhong, W. Zhu, A. Lin, M.S. El-Shall, Synergetic catalysis of palladium nanoparticles encaged within amine-functionalized UiO-66 in the hydrodeoxygenation of vanillin in water, Green Chem. 18 (2016) 2900–2908.

[22] D.M. Driscoll, D. Troya, P.M. Usov, A.J. Maynes, A.J. Morris, J.R. Morris, Characterization of undercoordinated Zr defect sites in UiO-66 with vibrational spectroscopy of adsorbed CO, J. Phys. Chem. C 122 (2018) 14582–14589.

[23] C.H. Sharp, J. Abelard, A.M. Plonka, W. Guo, C.L. Hill, J.R. Morris, Alkane–OH hydrogen bond formation and diffusion energetics of n-butane within UiO-66, J. Phys. Chem. C 121 (2017) 8902–8906.

[24] J.N. Joshi, G. Zhu, J.J. Lee, E.A. Carter, C.W. Jones, R.P. Lively, K.S. Walton, Probing metal−organic framework design for adsorptive natural gas purification, Langmuir 34 (2018) 8443–8450.

[25] D. Yang, M.A. Ortuño, V. Bernales, C.J. Cramer, L. Gagliardi, B.C. Gates, Structure and dynamics of Zr$_6$O$_8$ metal−organic framework node surfaces probed with ethanol dehydration as a catalytic test reaction, J. Am. Chem. Soc. 140 (2018) 3751–3759.

[26] P.S. Barcia, D. Guimarjes, P.A.P. Mendes, J.A.C. Silva, V. Guillerm, H. Chevreau, C. Serre, A.E. Rodrigues, Reverse shape selectivity in the adsorption of hexane and xylene isomers in MOF UiO-66, Microporous Mesoporous Mater. 139 (2011) 67–73.

[27] F. Bonino, C. Lamberti, S. Bordiga, IR and Raman spectroscopies probing MOFs structure, defectivity, and reactivity, in: S. Kaskel (Ed.), The Chemistry of Metal–Organic Frameworks: Synthesis, Characterization, and Applications, Wiley-VCH Verlag GmbH, 2016, p. 657.

[28] C. Atzori, G.S. Shearer, L. Maschio, B. Civalleri, F. Bonino, C. Lamberti, S. Svelle, K.P. Lillerud, S. Bordiga, Effect of benzoic acid as a modulator in the structure of UiO-66: an experimental and computational study, J. Phys. Chem. C 121 (2017) 9312–9324.

[29] V.V. Butova, A.P. Budnyk, K.M. Charykov, K.S. Vetlitsyna-Novikova, A.L. Bugaev, A.A. Guda, A. Damin, S.M. Chavan, S. Øien-Ødegaard, K.P. Lillerud, A.V. Soldatov, C. Lamberti, Partial and complete substitution of the 1,4-benzenedicarboxylate linker in UiO-66 with 1,4-naphthalenedicarboxylate: synthesis, characterization, and H$_2$-adsorption properties, Inorg. Chem. 58 (2019) 1607–1620.

[30] G.C. Shearer, S. Chavan, J. Ethiraj, J.G. Vitillo, S. Svelle, U. Olsbye, C. Lamberti, S. Bordiga, K.P. Lillerud, Tuned to perfection: ironing out the defects in metal–organic framework UiO-66, Chem. Mater. 26 (2014) 4068–4071.

[31] J. Ethiraj, E. Albanese, B. Civalleri, J.G. Vitillo, F. Bonino, S. Chavan, G. Shearer, K.P. Lillerud, S. Bordiga, CO$_2$ Adsorption in amine functionalized mixed ligand metalorganic frameworks of UiO-66 topology, ChemSusChem 7 (2014) 3382–3388.

[32] S.M. Chavan, G.C. Shearer, S. Svelle, U. Olsbye, F. Bonino, J. Ethiraj, K.P. Lillerud, S. Bordiga, Synthesis and characterization of amine functionalized mixed ligand metal–organic frameworks of UiO-66 topology, Inorg. Chem. 53 (2014) 9509–9515.

[33] M. Sarker, J.Y. Song, H. Sung, Carboxylic-acid-functionalized UiO-66-NH$_2$: a promising adsorbent for both aqueous- and non-aqueous-phase adsorptions, Chem. Eng. J. 331 (2018) 124–131.

[34] X. Zhang, X. Lv, X. Shi, Y. Yang, Y. Yang, Enhanced hydrophobic UiO-66 (University of Oslo 66) metal–organic framework with high capacity and selectivity for toluene capture from high humid air, J. Colloid Interface Sci. 539 (2019) 152–160.

[35] L. Fu, S. Wang, G. Lin, L. Zhang, Q. Liu, J. Fang, C. Wei, G. Liu, Post-functionalization of UiO-66-NH$_2$ by 2,5-dimercapto-1,3,4-thiadiazole for the high efficient removal of Hg(II) in water, J. Hazard Mater. 368 (2019) 42–51.

[36] T.G. Grissom, C.H. Sharp, P.M. Usov, D. Troya, A.J. Morris, J.R. Morris, Benzene, toluene, and xylene transport through UiO-66: diffusion rates, energetics, and the role of hydrogen bonding, J. Phys. Chem. C 122 (2018) 16060–16069.

[37] H. Saleem, U. Rafique, R.P. Davies, Investigations on post-synthetically modified UiO-66-NH$_2$ for the adsorptive removal of heavy metal ions from aqueous solution, Microporous Mesoporous Mater. 221 (2016) 238–244.

[38] H.G.T. Nguyen, L. Mao, A.W. Peters, C.O. Audu, Z.J. Brown, O.K. Farha, J.T. Hupp, S.B.T. Nguyen, Comparative study of titanium-functionalized UiO-66: support effect on the oxidation of cyclohexene using hydrogen peroxide, Catal. Sci. Technol. 5 (2015) 4444–4451.

[39] D.M. Driscoll, D. Troya, P.M. Usov, A.J. Maynes, A.J. Morris, J.R. Morris, Geometry and energetics of CO adsorption on hydroxylated UiO-66, Phys. Chem. Chem. Phys. 21 (2019) 5078–5085.

[40] M. Mihaylov, S. Andonova, K. Chakarova, A. Vimont, E. Ivanova, N. Drenchev,

K. Hadjiivanov, An advanced approach for measuring acidity of hydroxyls in con-fined space: FTIR study of low-temperature CO and $^{15}N_2$ adsorption on MOF sam-ples from the MIL-53(Al) series, Phys. Chem. Chem. Phys. 17 (2015) 24304–24314.

[41] S. Friebe, A. Mundstock, K. Volgmann, J. Caro, On the better understanding of the surprisingly high performance of metal-organic framework-based mixed-matrix membranes using the example of UiO-66 and Matrimid, ACS Appl. Mater. Interfaces 9 (2017) 41553–41558.

[42] K. Hadjiivanov, Identification and characterization of surface hydroxyl groups by infrared spectroscopy, Adv. Catal. 57 (2014) 99–318.

[43] K. Hadjiivanov, G. Vayssilov, Characterization of oxide surfaces and zeolites by carbon monoxide as an IR probe molecule, Adv. Catal. 47 (2002) 307–511.

[44] L. Kustov, New trends in IR-spectroscopic characterization of acid and basic sites in zeolites and oxide catalysts, Top. Catal. 4 (1997) 131–144.

[45] A. Zecchina, C. Otero Arean, Diatomic molecular probes for mid-IR studies of zeolites, Chem. Soc. Rev. 25 (1996) 187–197.

[46] K. Chakarova, N. Drenchev, M. Mihaylov, P. Nikolov, K. Hadjiivanov, OH/OD isotopic shift factors of isolated and H-bonded surface silanol groups, J. Phys. Chem. C 117 (2013) 5242–5248.

[47] K. Hadjiivanov, A. Penkova, M.A. Centeno, FTIR Indication of CO interaction with O^{2-} ions: a new adsorption form in the gap between chemi- and physisorbed CO, Catal. Commun. 8 (2007) 1715–1719.

[48] D. Perra, N. Drenchev, K. Chakarova, M.G. Cutrufello, K. Hadjiivanov, Remarkable acid strength of ammonium ions in zeolites: FTIR study of low-temperature CO adsorption on NH_4FER, RSC Adv. 4 (2014) 56183–56187.

[49] E.P.L. Hunter, S.G. Lias, Evaluated gas phase basicities and proton affinities of molecules: an update, J. Phys. Chem. Ref. Data 27 (1998) 413–656.

[50] F. Thibault-Starzyk, F. Maugé, M. Che, J. C Vedrine (Eds.), Characterization of Solid Materials and Heterogeneous Catalysts. From Structure to Surface Reactivity, vol. 1, Wiley, VCH, Weinheim, 2012, pp. 3–48.

[51] J. Hajek, B. Bueken, M. Waroquier, F. De Vos, V. Van Speybroeck, The remarkable amphoteric nature of defective UiO-66 in catalytic reactions, ChemCatChem 9 (2017) 2203–2210.

[52] F. Vermoortele, R. Ameloot, L. Alaerts, R. Matthessen, B. Carlier, E.V.R. Fernandez, J. Gascon, F. Kapteijn, D.E. De Vos, Tuning the catalytic performance of

metalorganic frameworks in fine chemistry by active site engineering, J. Mater. Chem. 22 (2012) 10313–10321.

[53] A. Vimont, H. Leclerc, F. Mauge, M. Daturi, J.-C. Lavalley, S. Surble, C. Serre, G. Férey, Creation of controlled Brønsted acidity on a zeotypic mesoporous chro-mium(iii) carboxylate by grafting water and alcohol molecules, J. Phys. Chem. C 111 (2007) 383–388.

[54] C. Volkringer, H. Leclerc, J.-C. Lavalley, T. Loiseau, G. Férey, M. Daturi, A. Vimont, Infrared spectroscopy investigation of the acid sites in the metal – organic frame-work aluminum trimesate MIL-100(Al), J. Phys. Chem. C 116 (2012) 5710–5719.

[55] E.V. Ramos-Fernandez, C. Pieters, B. van der Linden, J. Juan-Alcañiz, P. Serra-Crespo, M.W.G.M. Verhoeven, H. Niemantsverdriet, J. Gascon, F. Kapteijn, Highly dispersed platinum in metal organic framework NH_2-MIL-101(Al) containing phosphotungstic acid – characterization and catalytic performance, J. Catal. 289 (2012) 42–52.

[56] M. Dan-Hardi, H. Chevreau, T. Devic, P. Horcajada, G. Maurin, G. Férey, D. Popov, C. Riekel, S. Wuttke, J.-C Lavalley, A. Vimont, T. Boudewijns, D. De Vos, C. Serre, How interpenetration ensures rigidity and permanent porosity in a highly flexible hybrid solid, Chem. Mater. 24 (2012) 2486–2492.

[57] A.M. Bumstead, D.B. Cordes, D.M. Dawson, K.K. Chakarova, M.Y. Mihaylov, C.L. Hobday, T. Düren, K.I. Hadjiivanov, A.M.Z. Slawin, S.E. Ashbrook, R.R.R. Prasad, P.A. Wright, Modulator-controlled synthesis of microporous STA-26, an interpenetrated 8,3-connected zirconium MOF with the the-i topology, and its reversible lattice shift, Chem. Eur J. 24 (2018) 6115–6126.

[58] R.R.R. Prasad, S.E. Seidner, D.B. Cordes, M.M. Lozinska, D.M. Dawson, M.J. Thompson, T. Düren, K.K. Chakarova, M.Y. Mihaylov, K.I. Hadjiivanov, F. Hoffmann, A.M.Z. Slawin, S.E. Ashbrook, M.L. Clarke, P.A. J Wright, STA-27, a porous Lewis acidic scandium MOF with an unexpected topology type prepared with 2,3,5,6-tetrakis(4-carboxyphenyl)pyrazine, J. Mater. Chem. A 7 (2019) 5686–5701, https://doi.org/10.1039/C8TA10610J.

[59] M.A. Babaeva, D.S. Bystrov, A.Y. Kovalgin, A.A. Tsyganenko, CO interaction with the surface of thermally activated CaO and MgO, J. Catal. 123 (1990) 396–416.

[60] M.A. Babaeva, A.A. Tsyganenko, Infrared spectroscopic evidence for the formation of carbonite CO_2^{2-} ions in CO interaction with basic oxide surfaces, React. Kinet. Catal. Lett. 34 (1987) 9–14.

7.3 UiO-66 and UiO-66-NH₂ based sensors: Dielectric and FTIR investigations on the effect of CO₂ adsorption

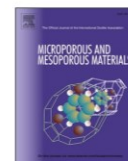I. Strauss, K. Chakarova, A. Mundstock, M. Mihaylov, K. Hadjiivanov, N. Guschanski, J. Caro

UiO-66 and UiO-66-NH$_2$ based sensors: Dielectric and FTIR investigations on the effect of CO$_2$ adsorption[☆]

Ina Strauss [a,**], Kristina Chakarova [b], Alexander Mundstock [a], Mihail Mihaylov [b], Konstantin Hadjiivanov [b], Natalija Guschanski [c], Jürgen Caro [a,*]

[a] Institute of Physical Chemistry and Electrochemistry, Leibniz Universität Hannover, Callinstraße 3A, D-30167, Hannover, Germany
[b] Institute of General and Inorganic Chemistry, Bulgarian Academy of Sciences, Sofia, 1113, Bulgaria
[c] Faculty for Electrical Engineering and Information Technology, Hochschule Hannover, Ricklinger Stadtweg 120, D-30167, Hannover, Germany

ARTICLE INFO

ABSTRACT

Nano-scaled UiO-66 and UiO-66-NH$_2$ crystals are synthesized via a solvothermal procedure and investigated regarding their applicability in CO$_2$ sensing devices. The interaction between CO$_2$ and UiO-66 as well as UiO-66-NH$_2$ is studied via FTIR and dielectric measurements with a home-made sensing-cell contraption. The affinity towards low CO$_2$ concentrations is proved by FTIR measurements with 20 ppm CO$_2$. We show, that the co-existence of water leads to an even higher CO$_2$ adsorption compared to the absence of water. Both UiO-MOFs show a good response towards low CO$_2$ concentrations, but UiO-66-NH$_2$ is far more sensitive than UiO-66. In dielectric studies, the affinity of UiO-66 and UiO-66-NH$_2$ towards CO$_2$ results in a strong decrease of the capacity at low frequencies. While UiO-66-NH$_2$ seems to be suited for sensing devices within a CO$_2$ concentration range from 1 up to 100%, UiO-66 seems not be suitable for capacitive CO$_2$ sensing.

1. Introduction

The detection of CO$_2$ is an important task in different fields such as environment and safety control, biotechnology or chemical and combustion industry [1]. Depending on the field of application, the requirements regarding sensitivity and accuracy of the sensor can vary from high to low CO$_2$ concentrations, which results in a large number of developed devices. Within the environmental application field, Pettenkofer suggested a CO$_2$ concentration of 1000 ppm as the maximum value of tolerable indoor air concentration and the American Conference of Governmental Industrial Hygienists (ACGIH) state the threshold limit value for long term exposure at 5000 ppm, while within the field of industrial applications, for example in food packaging, CO$_2$ sensors are desired which are able to differentiate concentrations between the range of 10% up to 80% [1–7].

Metal-organic frameworks (MOFs) [8], as inorganic-organic hybrid compounds in the class of soft porous materials, have been studied for about 15 years now [9], proving their potential applicability in catalysis [10,11], gas storage [12,13], drug delivery [14,15] or sensing [16,17], reasoned in their large intrinsic porosity and BET surface as well as tailorability to create an affinity towards guest molecules such as H$_2$S, SO$_2$ including CO$_2$ [18–22].

In our previous work we showed, that UiO-66 and UiO-66-NH$_2$ are strongly affected by the interaction with adsorbed molecules like CO, N$_2$ and CD$_3$CN [23]. Here we investigate these two UiO MOFs towards their suitability for the sensing of CO$_2$. MOFs, which are easy to produce as tablets and thin films, could therefore lead to a new kind of simple and cost-effective sensors [24].

The Zr-based MOF UiO-66 consists of the secondary building unit (SBU) [Zr$_6$O$_4$(OH)$_4$], which is connected to the organic linker benzene-1,4-dicarboxylic acid, while in UiO-66-NH$_2$ these SBUs are connected to 2-aminoterephthalic acid (see Fig. 1) [25]. The octahedral Zr$_6$-clusters of the SBUs are alternatively capped by μ$_3$-OH and μ$_3$-O groups [26]. Due to thermal activation, it is possible to remove the μ$_3$-OH groups without
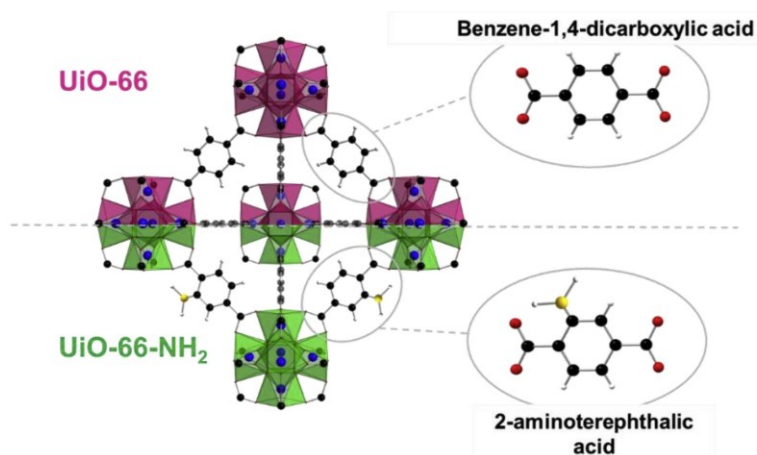

Fig. 1. Schematic representation of the crystal structure of UiO-66 and UiO-66-NH$_2$ showing the differences in the linker molecules.

changes regarding the connecting carboxylates [27].

2. Experimental

2.1. Synthesis of UiO-66 and UiO-66-NH$_2$

Both samples were synthesized via a benzoic acid modulated hydrothermal synthesis as described before [23]. For the synthesis of UiO-66 powder, a solution of 0.28 g zirconium chloride (ZrCl$_4$, anhydrous, 98%, Alfa Aesar) and 4.5 mL dimethylformamide (DMF, 99.8%, Carl Roth) and a second solution of 4.4 g benzoic acid (C$_7$H$_6$O $\geq$ 99.5%, Sigma Aldrich) and 0.42 g terephthalic acid (H$_2$bdc, 98%, Sigma Aldrich) in 10 mL DMF were prepared and heated up to 150 °C. The solutions were combined in a Teflon lined autoclave, which was placed

for 24 h in a conventional oven at 180 °C. Afterwards, the crystals were washed three times with MeOH and dried at 60 °C. For the synthesis of UiO-66-NH$_2$ 0.46 g of 2-aminoterephthalic acid (NH$_2$bdc, 99%, Sigma Aldrich) was used instead of H$_2$bdc.

2.2. Charactzerization

The crystal structures of UiO-66 and UiO-66-NH$_2$ were analyzed via X-Ray diffraction measurements performed on a Bruker D8 Advance X-ray diffractometer with LYNXEYE detection technology and Cu$_{K\alpha}$ (λ = 0.154 nm) radiation.

Scanning electron microscopy was performed with a JEOL JSM-6700F field emission scanning electron microscope. The particle images were taken with an acceleration voltage of 2 kV and an acceleration
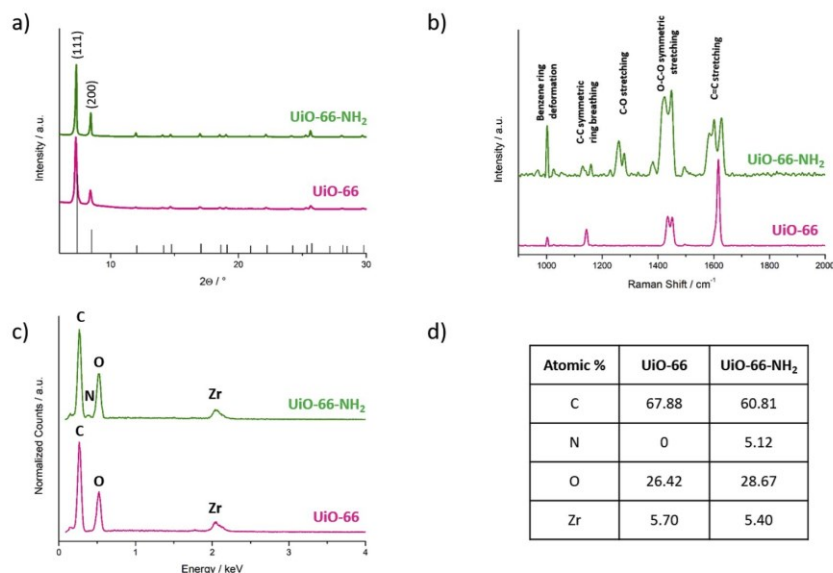

Fig. 2. (a) Powder XRD patterns of UiO-66 and UiO-66-NH$_2$ compared to the UiO-66 theoretical data. (b) Raman spectra of UiO-66 compared to UiO-66-NH$_2$. (c) EDX spectra of UiO-66 and UiO-66-NH$_2$. (d) Atomic % of contained elements in UiO-66 and UiO-66-NH$_2$ based on the EDX analysis.
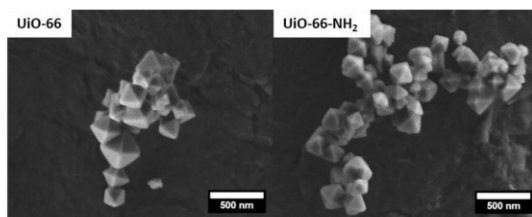
Fig. 3. SEM images of UiO-66 and UiO-66-NH$_2$ powders showing octahedrally shaped crystals.

current of 10 μA. Energy dispersive X-ray (EDX) spectra were taken with an acceleration voltage of 5 kV and an acceleration current of 10 μA. Raman spectroscopy was performed using a Bruker Senterra Raman spectrometer with a laser excitation wavelength of 532 nm.

2.3. FTIR spectroscopy

The FTIR spectra of UiO-66 and UiO-66-NH$_2$ were recorded with a Nicolet 6700 FTIR spectrometer accumulating 64 scans at a spectral resolution of 2 cm^{-1}. Self–supporting pellets (ca. 10 mg cm^{-2}) were prepared from the sample powder and treated directly in the IR cell. The IR cell was connected to a vacuum-adsorption apparatus with a residual pressure below 10^{-3} Pa. Prior to the adsorption experiments, the samples were evacuated at RT. or at 250 °C. The adsorption measurements were made using CO$_2$ (Messer, 99.995%).

2.4. Dielectric studies

CO$_2$ dependent capacity measurements were performed with a Novocontrol Alpha A impedance analyzer, using high quality interdigitated electrodes with a diameter of 15 mm and a spacing between the comb fingers and their width of 75 μm (BDS 1410-15-75, Novocontrol Technologies) within a home-made measurement cell. The UiO-66 and UiO-66-NH$_2$ samples were dispersed in ethanol, drop casted on the interdigitated electrodes and dried at room temperature for 24 h. After an evacuation, the cell was filled with N$_2$ and/or CO$_2$. The subsequent

measurement was carried out within a frequency range from 10^{-2} to 10^7 Hz and a RMS amplitude of the AC voltage of 0.5 V was used. Both samples were measured twice in order to determine the sensors stability. Since the values did not significantly change, due to the well-known high stability of UiO-66, only one measurement sample is shown [28].

3. Results

3.1. Characterization

The UiO-66 and UiO-66-NH$_2$ crystals are characterized via XRD, Raman and EDX measurements (Fig. 2) as well as via SEM images (Fig. 3). The XRD patterns for both materials are shown in Fig. 2a and exhibit the main characteristic reflexes of the UiO-66 series at 7.4° and 8.5°, which is in good accordance with the theoretical pattern of UiO-66 also shown in Fig. 2a. Raman spectra are shown in Fig. 2b and match with previously published spectra of UiO-66 and UiO-66-NH$_2$ [29,30]. The main peaks can be assigned to the C=C stretching of the aromatic rings (1632 cm^{-1}), the carboxylate O–C–O symmetric stretch (1445 cm^{-1}), the C–O stretching, which is only seen in the spectra of UiO-66-NH$_2$ (1270 cm^{-1}), the C–C symmetric ring breathing (1143 cm^{-1}) and the benzene ring deformation (1012 cm^{-1}) [29,30]. In Fig. 2c) and d) the EDX spectra of UiO-66 and UiO-66-NH$_2$ with the corresponding table of the Atomic % of elements existing in both materials are shown. As assumed, only the UiO-66-NH$_2$ powder possesses nitrogen. The atomic % of the nitrogen, corresponding to the NH$_2$-group of the linker molecule of UiO-66-NH$_2$ is 5.12% (according to the structural formula, UiO-66-NH$_2$ contains 5.05% nitrogen). SEM images of both materials show the nano-scaled crystals with their typical octahedral morphology. The crystalls possess an approximate crystal size in the range around 100 nm.

3.2. FTIR investigations of CO$_2$ adsorption and CO$_2$/H$_2$O co-adsorption on UiO-66 and UiO-66-NH$_2$

The FTIR spectra of the UiO-66 and UiO-66-NH$_2$ samples after different pre-treatments and in the presence of 20 mbar CO$_2$ are presented in Fig. 4. The results on the evolution of the FTIR spectra are already reported [23] and here we recall the following observations:
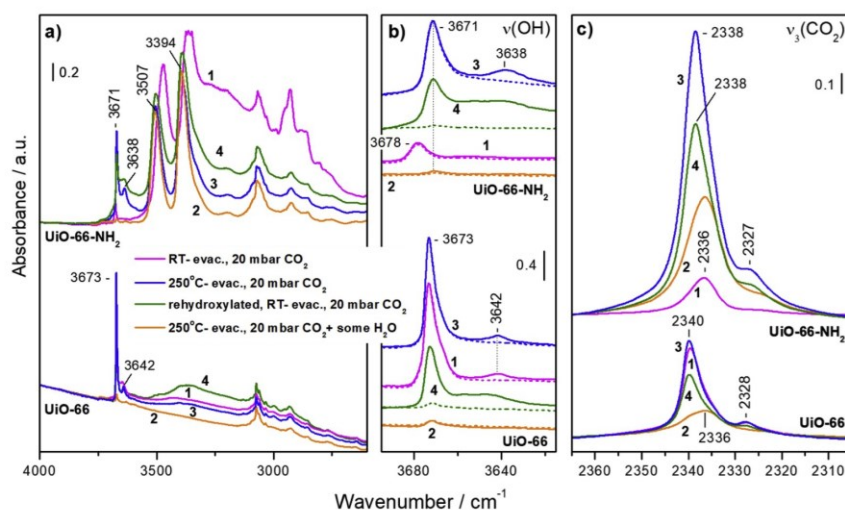

Fig. 4. FTIR spectra of UiO-66 and UiO-66-NH$_2$ in the presence of 20 mbar CO$_2$. The materials were previously evacuated at ambient temperature **1** and at 250 °C **2** and re-hydroxylated **3**. Spectrum **4** was registered after co-adsorption of CO$_2$ and H$_2$O. Dashed lines in panel b) show the corresponding background spectra before CO$_2$ adsorption. The spectra in panel c) are background and CO$_2$ gas-phase corrected. All spectra are registered at RT.
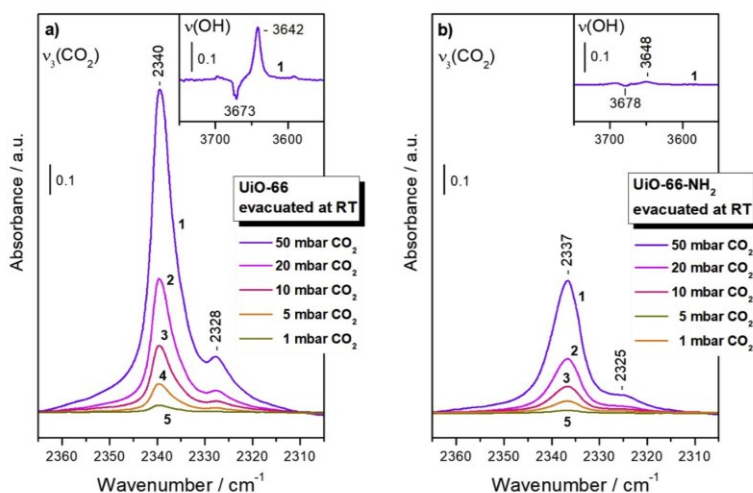
Fig. 5. FTIR spectra of different amounts of CO_2 adsorbed on UiO-66 a) and UiO-66-NH_2 b) after evacuation of the samples at ambient temperature. All spectra are background and CO_2 gas-phase corrected.

- The spectrum of UiO-66 evacuated at RT contains a sharp band at 3673 cm^{-1} due to μ_3-OH groups. This band almost disappears after evacuation at 250 °C indicating sample de-hydroxylation. It is practically restored after subsequent treatment with H_2O vapors, i.e. the sample is re-hydroxylated.
- Similar effects were observed with UiO-66-NH_2. However, with this sample the OH band appeared at 3678 cm^{-1} with moderate intensity after evacuation at RT and was very intense in the re-hydroxylated sample (at 3671 cm^{-1}). In addition, bands due to residual DMF were registered in the initial spectrum and vanished after activation. The results indicate that a large part of the structural OH groups have been blocked by DMF which resisted evacuation at RT. The OH groups H-bonded to DMF are responsible for the appearance of a

broad IR feature centered around 3200 cm^{-1}. During the activation process, these DMF impurities disappeared.

The amount of adsorbed CO_2 was monitored by the intensity of the $\nu_3(CO_2)$ band around 2340 cm^{-1} (Fig. 4c). The most intense band is at 2340 cm^{-1} (UiO-66) and 2338 cm^{-1} (UiO-66-NH_2) and a component at 2336 cm^{-1} is visible within both samples. These bands are attributed to the $\nu_3(CO_2)$ modes of adsorbed CO_2. A weak low-frequency satellite at 2328-2327 cm^{-1} is also detected and is due to the so-called "hot" band (resulting from a transition between two excited vibrational states). It is seen that the amount of adsorbed CO_2, estimated on the basis of the intensity of the $\nu_3(CO_2)$ band, roughly correlates with the intensity of the μ_3-OH band, thus indicating that the hydroxyl groups are active sites for CO_2 adsorption. This statement is also supported by the appearance of a

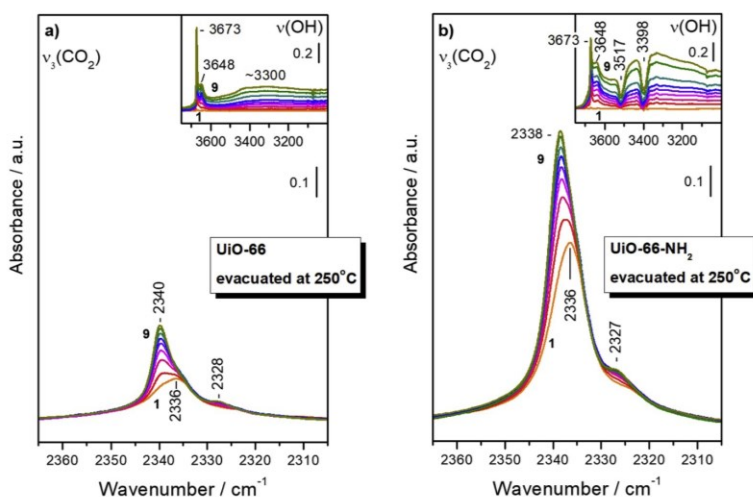**Fig. 6.** FTIR spectra of CO_2 and H_2O co-adsorbed on UiO-66 a) and UiO-66-NH_2 b). Spectra a/b) **1** correspond to 20 mbar CO_2 adsorbed on samples evacuated at 250 °C, spectra a/b) **2–9** show the evolution after subsequent adsorption of increasing amounts of H_2O (for details see text). All spectra are background and CO_2 gas-phase corrected.

4

band at to 3648-3640 cm^{-1}, attributed to H-bonded OH···OCO adducts, and a parallel decrease in intensity of the μ_3-OH band (Fig. 4b). There are three important peculiarities that should be underlined:

- De-hydroxylated samples also adsorb CO_2 and the adsorption form can be associated with the band at 2336 cm^{-1}. Therefore, in addition to the OH groups, there is a second kind of CO_2 adsorption sites in both samples.
- The CO_2-induced shift of the ν(OH) modes at 3773 cm^{-1}, $\Delta\nu$(OH), is around -31 cm^{-1} for UiO-66 and (see Fig. 5) and -33cm^{-1} for UiO-66-NH$_2$. These values are intermediate between the shifts caused by adsorption of CO (-82 cm^{-1}) and N$_2$ (-25cm^{-1}), which correlates with the proton affinities of these three probe molecules. However, it seems that a larger fraction of OH groups is affected under 20 mbar CO_2 with the UiO-66-NH$_2$ sample. This phenomenon is probably due to some kind of additional stabilization of the OH···OCO adducts and to the slightly higher acidity of the hydroxyls in UiO-66-NH$_2$.
- The CO_2 adsorption capacity of DMF-free UiO-66-NH$_2$ is higher than for UiO-66.

Analysis of the spectra 1–3 in Fig. 4 indicates that the second kind of CO_2 adsorption sites (monitored by a band at 2336 cm^{-1}) is not substantially affected by the sample hydroxylation degree. This suggests that water has a positive effect on the CO_2 adsorption capacity. To confirm this hypothesis, we have studied co-adsorption of CO_2 and water on both samples and the results are presented in Fig. 6. First, CO_2 (equilibrium pressure 20 mbar) was contacted with the sample. Then a tank containing water vapour was opened to the cell (nominal final partial H$_2$O pressure of 2 mbar) and this allowed water to diffuse to the sample pellet. During this process, we continuously recorded spectra corresponding to increasing amounts of water adsorbed onto the sample. It is seen that increasing the amount of the co-adsorbed water indeed leads to a gradual increase of the overall intensity of the ν_3(CO_2) band. In parallel with this, three bands are developed in the OH stretching region of the UiO-66 sample: at 3673, 3648 and around 3300 cm^{-1}. The bands at 3673 and 3643 cm^{-1} were already assigned to isolated and CO_2-affected hydroxyls. The band at 3300 cm^{-1} has a more complex origin and is attributed to H-bonded hydroxyls due to μ_3-OH···OH$_2$ species and adsorbed water. Similar spectra were recorded with the UiO-66-NH$_2$ sample. However, in this case some of the NH$_2$ groups were also affected (negative bands at 3517 and 3398 cm^{-1}), evidently by the adsorbed water molecules. These findings are comparable to the previously published DFT calculations. According to Ethiraj et al. the adsorption mechanism takes places at three different adsorption sites within the hydroxylated UiO-66-NH$_2$. First of all, CO_2 is able to interact directly with the hydroxyl group of the UiO-66-like OH-group. In addition to that, CO_2 simultaneously interacts with the amino group and undertakes hydrogen bonding interaction with the OH group vicinal to the amino groups [31].

The spectra with the most intense bands from Fig. 6 are also shown in Fig. 4 for comparison. It is seen that the intensity of the CO_2 bands reaches about 2/3 of the maximal intensity obtained with the re-hydroxylated samples. This observation is easy to explain because during CO_2 and H$_2$O co-adsorption the samples are re-hydroxylated, but the competitive adsorption of H$_2$O and CO_2 on the hydroxyl groups leads to some decrease in the CO_2 uptake.

3.3. Capacity measurements of UiO-66 and UiO-66-NH$_2$ under CO_2 and other gases

Subsequent to the FTIR CO_2 investigations, frequency dependent CO_2 capacity measurements of an interdigital capacitor, using UiO-66 and UiO-66-NH$_2$ as dielectric coating material were performed. The interdigital capacitor is placed in the measurement cell, which possesses a gas inlet and gas outlet to control the N$_2$/CO_2 gas flow. The capacitor is connected to a 4 wire impedance interface, as shown in Fig. 7.
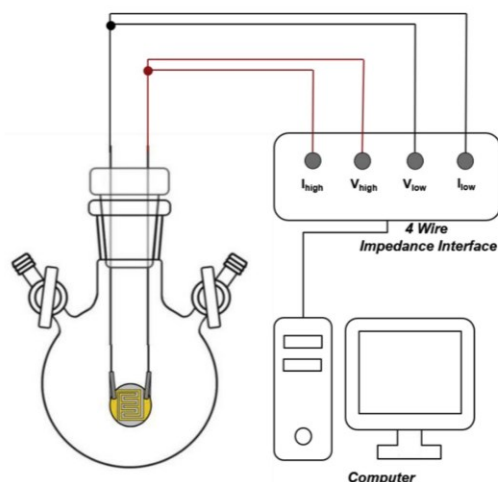

Fig. 7. Experimental 4-wire impedance set-up, showing the interdigital capacitor placed in a home-made measurement cell.
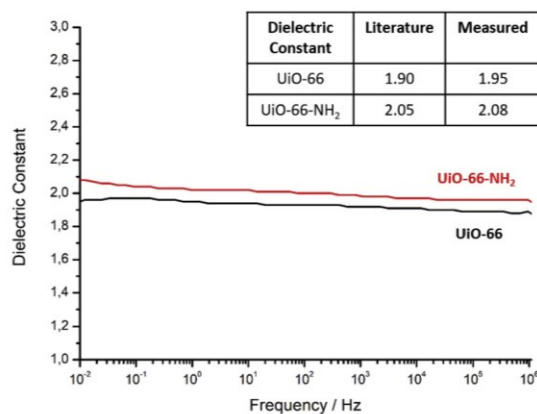

Dielectric Constant	Literature	Measured
UiO-66	1.90	1.95
UiO-66-NH$_2$	2.05	2.08

Fig. 8. Dielectric constants of UiO-66 and UiO-66-NH$_2$ measured under vacuum. The inset table compares the measured values with literature data.

Determining the permittivity, Fig. 8 shows the results of the dielectric measurements of UiO-66 and UiO-66-NH$_2$ under vacuum. For UiO-66 we measured a dielectric constant of 1.95 and for UiO-66-NH$_2$ of 2.08. These results are in good accordance with literature data of the dielectric constants of UiO-66 (1.90) and UiO-66-NH$_2$ (2.05) [32]. The frequency dependent capacity of UiO-66-NH$_2$ was determined under vacuum, in Ne, Ar, N$_2$ and CO_2 (see Fig. 9). When UiO-66-NH$_2$ is in a Ne, Ar or N$_2$ atmosphere, the capacity at low frequencies is relatively high, compared to CO_2 and vacuum. We assume, that these observations might be traced back to a build-up of charge carriers on a mesoscopic scale at the inner boundaries (cage and frameworks of the UiO or the intercrystal boundaries), called Maxwell-Wagner-Sillars (MWS) polarizations [33]. The separated charges can be considered as a kind of a "superdipole", which is reoriented according to the electrical field especially at low frequencies [34,35]. Due to the selective adsorption of CO_2 [36] at the functional amino-group, the charge separation over mesoscopic distances is suppressed resulting in a less pronounced Maxwell-Wagner-Sillars polarization. However, in vacuum the capacity of UiO-66-NH$_2$ is suprisigly as low as in the case of the strongly adsorbed
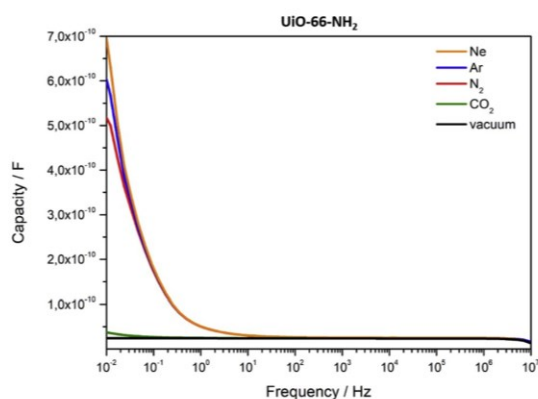
5

Fig. 9. Frequency dependent capacity of UiO-66-NH$_2$ under vacuum and with Ne, Ar, N$_2$ and CO$_2$ atmospheres.
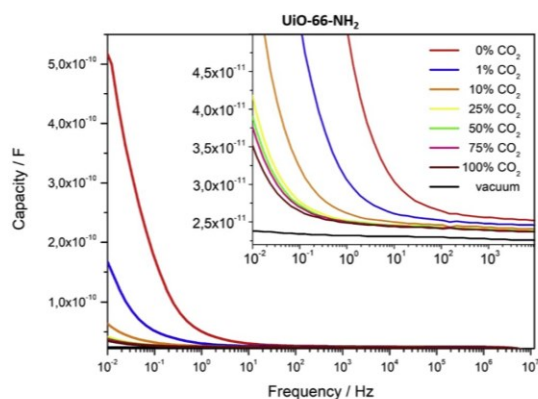

Fig. 10. Frequency dependent capacity of UiO-66-NH$_2$ under vacuum and with N$_2$/CO$_2$ mixtures varying from 100/0% up to 0/100%. Inset shows the zoom-in of the measurements in the frequency range between 10^{-2} up to 10^4.

CO$_2$. We cannot fully understand this reproducible experimental finding. Obviously, both selective CO$_2$ adsorption and evacuation block the MWS polarization. It could be that a slight expansion of the MOF framework by adsorption of guest molecules is a condition for the occurrence of the MWS polarization which is again suppressed in case of the strong CO$_2$ adsorption. Fig. 10 shows the frequency dependent capacity of the interdigital capacitor with UiO-66-NH$_2$ as dielectric

material. The measurements were performed with a varying ratio of N$_2$/CO$_2$ from 100/0% up to 0/100%. The highest capacity was obtained for the measurement with 100% N$_2$/0% CO$_2$ and it can be seen, that with an increase of CO$_2$ partial pressure, the capacity is decreased. Fig. 11 compares the described frequency dependent capacity of UiO-66-NH$_2$ under vacuum and with a mixture of N$_2$/CO$_2$ varying between 100/0% up to 0/100% with those of UiO-66. This MOF shows no significant changes of the capacity as a function the frequency under vacuum and in different CO$_2$ atmospheres. These findings are in good accordance with CO$_2$ adsorption isotherms of UiO-66 and UiO-66-NH$_2$, which show a significantly higher uptake of CO$_2$ for the functionalized MOF [37].

4. Conclusions

We show that UiO-66 as well as UiO-66-NH$_2$ are able to adsorb CO$_2$, but only the latter one is suited for gas sensing applications. UiO-66-NH$_2$ has a significantly higher CO$_2$ absorbance than UiO-66 due to the amine-functionalization as proven by FTIR measurements. Furthermore, UiO-66 is incapable of detecting large CO$_2$ concentrations, while UiO-66-NH$_2$ still shows capacity changes corresponding to the applied CO$_2$ percentages up to 100%, as validated by additional dielectric investigations. In dielectric studies, strongly adsorbed CO$_2$ suppresses the Maxwell-Wagner-Sillars polarization which reduces the capacity at low frequencies. Regarding the performance of both MOFs in the presence of co-adsorbed water, FTIR results show a significantly higher CO$_2$ absorbance band in comparison to experiments in the absence of water. Here as well, the UiO-66-NH$_2$ outperforms the non-functionalized UiO-66. Last but not least, FTIR experiments showed the crucial importance of the thermal activation of MOFs, especially to eliminate impurities such as solvents. In conclusion, UiO-66-NH$_2$ might be a potential MOF-based sensor material for sensing both, low and high concentrations of CO$_2$.

Author contribution

I. S. has developed the concept of this paper, made most of the experiments (synthesis, characterization, dielectric measurements) and has written the draft of the paper. K.C. performed the CO$_2$ dependent FTIR measurements and wrote the FTIR part of the paper in consultation with K.H. A.M. and M.M. have equally contributed to this paper by experimental support and discussions of the results. Profs. K.H., N.G. and J.C. discussed concept, experiments and the manuscript.

Declaration of competing interest

The authors declare that they have no known competing financial interests or personal relationships that could have appeared to influence the work reported in this paper.
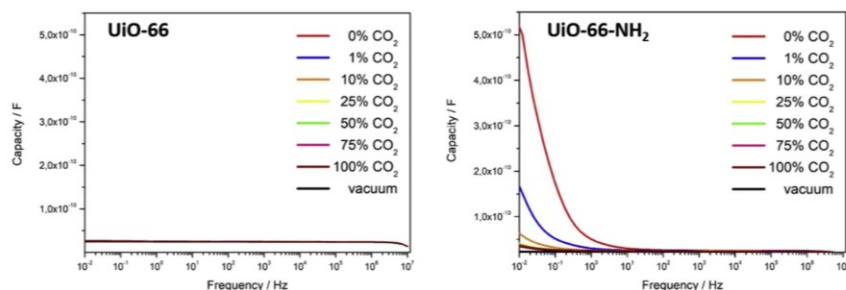

Fig. 11. Frequency dependent capacity of UiO-66 and UiO-66-NH$_2$ under vacuum and under a mixture of N$_2$/CO$_2$ varying between 100/0% up to 0/100%.
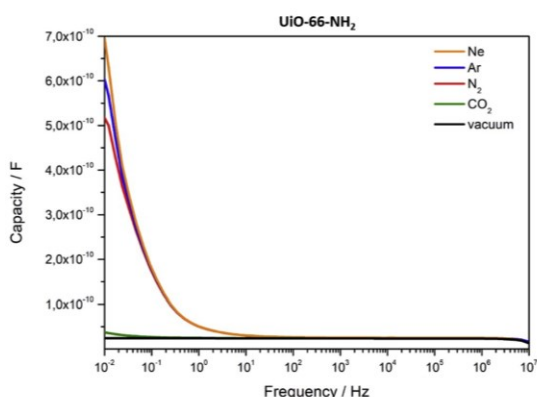
6

Fig. 9. Frequency dependent capacity of UiO-66-NH$_2$ under vacuum and with Ne, Ar, N$_2$ and CO$_2$ atmospheres.
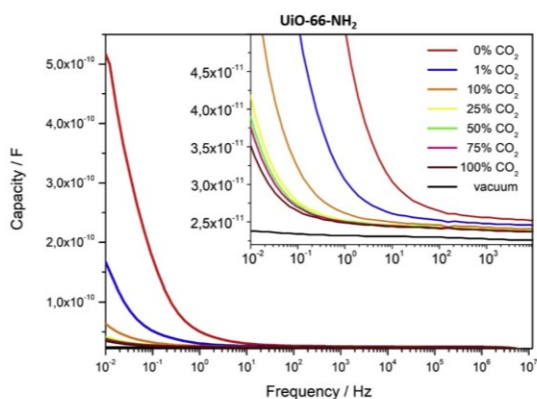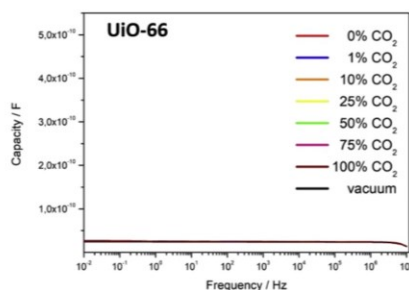

Fig. 10. Frequency dependent capacity of UiO-66-NH$_2$ under vacuum and with N$_2$/CO$_2$ mixtures varying from 100/0% up to 0/100%. Inset shows the zoom-in of the measurements in the frequency range between 10^{-2} up to 10^4.

CO$_2$. We cannot fully understand this reproducible experimental finding. Obviously, both selective CO$_2$ adsorption and evacuation block the MWS polarization. It could be that a slight expansion of the MOF framework by adsorption of guest molecules is a condition for the occurrence of the MWS polarization which is again suppressed in case of the strong CO$_2$ adsorption. Fig. 10 shows the frequency dependent capacity of the interdigital capacitor with UiO-66-NH$_2$ as dielectric

material. The measurements were performed with a varying ratio of N$_2$/CO$_2$ from 100/0% up to 0/100%. The highest capacity was obtained for the measurement with 100% N$_2$/0% CO$_2$ and it can be seen, that with an increase of CO$_2$ partial pressure, the capacity is decreased. Fig. 11 compares the described frequency dependent capacity of UiO-66-NH$_2$ under vacuum and with a mixture of N$_2$/CO$_2$ varying between 100/0% up to 0/100% with those of UiO-66. This MOF shows no significant changes of the capacity as a function the frequency under vacuum and in different CO$_2$ atmospheres. These findings are in good accordance with CO$_2$ adsorption isotherms of UiO-66 and UiO-66-NH$_2$, which show a significantly higher uptake of CO$_2$ for the functionalized MOF [37].

4. Conclusions

We show that UiO-66 as well as UiO-66-NH$_2$ are able to adsorb CO$_2$, but only the latter one is suited for gas sensing applications. UiO-66-NH$_2$ has a significantly higher CO$_2$ absorbance than UiO-66 due to the amine-functionalization as proven by FTIR measurements. Furthermore, UiO-66 is incapable of detecting large CO$_2$ concentrations, while UiO-66-NH$_2$ still shows capacity changes corresponding to the applied CO$_2$ percentages up to 100%, as validated by additional dielectric investigations. In dielectric studies, strongly adsorbed CO$_2$ suppresses the Maxwell-Wagner-Sillars polarization which reduces the capacity at low frequencies. Regarding the performance of both MOFs in the presence of co-adsorbed water, FTIR results show a significantly higher CO$_2$ absorbance band in comparison to experiments in the absence of water. Here as well, the UiO-66-NH$_2$ outperforms the non-functionalized UiO-66. Last but not least, FTIR experiments showed the crucial importance of the thermal activation of MOFs, especially to eliminate impurities such as solvents. In conclusion, UiO-66-NH$_2$ might be a potential MOF-based sensor material for sensing both, low and high concentrations of CO$_2$.

Author contribution

I. S. has developed the concept of this paper, made most of the experiments (synthesis, characterization, dielectric measurements) and has written the draft of the paper. K.C. performed the CO$_2$ dependent FTIR measurements and wrote the FTIR part of the paper in consultation with K.H. A.M. and M.M. have equally contributed to this paper by experimental support and discussions of the results. Profs. K.H., N.G. and J.C. discussed concept, experiments and the manuscript.

Declaration of competing interest

The authors declare that they have no known competing financial interests or personal relationships that could have appeared to influence the work reported in this paper.
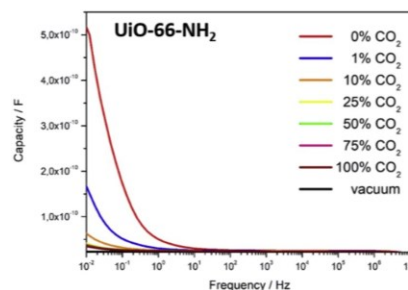

Fig. 11. Frequency dependent capacity of UiO-66 and UiO-66-NH$_2$ under vacuum and under a mixture of N$_2$/CO$_2$ varying between 100/0% up to 0/100%.

References

[1] G. Gerlach, U. Guth, W. Oelßner, Carbon Dioxide Sensing, first ed., Wiley-VCH, Berlin, 2019.
[2] J. Sundell, On the history of indoor air quality and health, Indoor Air 14 (2004) 51–58.
[3] J. Park, H. Cho, S. Yi, NDIR CO_2 gas sensor with improved temperature compensation, Procedia Eng. 5 (2010) 303–306.
[4] J.P. Kerry, M.N. O'Grady, S.A. Hogan, Past, current and potential utilization of active and intelligent packaging systems for meat and muscle-based products: a review, Meat Sci. 74 (2006) 113–130.
[5] S. Neethirajan, D.S. Jayas, S. Sadistap, Carbon dioxide (CO_2) sensors for the agri-food industry- A review, Food Bioprocess Technol. 2 (2009) 115–121.
[6] M. Ozdemir, J.D. Floros, Active food packaging technologies, Crit. Rev. Food Sci. Nutr. 44 (3) (2004) 185–193.
[7] I.M. Pérez de Vargas-Sansalvador, C. Fay, T. Phelan, M.D. Fernández-Ramos, L. F. Capitán-Vallvey, D. Diamond, F. Benito-Lopez, A new light emitting diode-light emitting diode portable carbon dioxide gas sensor based on an interchangeable membrane system for industrial applications, Anal. Chim. Acta 699 (2011) 216–222.
[8] J.L.C. Rowsell, O.M. Yaghi, Metal-organic frameworks: a new class of porous materials, Microporous Mesoporous Mater. 73 (2004) 3–14.
[9] J. Caro, Quo vadis, MOF? Chem. Ing. Tech. 90 (2018) 1759–1768.
[10] G. Fu, B. Bueken, D. De Vos, Zr-metal-organic framework catalysts for oxidative desulfurization and their improvement by postsynthetic lingand exchange, Small Methods 2 (2018) 1800203.
[11] A. Dhakshinamoorthy, Z. Li, H. Garcia, Catalysis and photocatalysis by metal organic frameworks, Chem. Soc. Rev. 47 (2018) 8134–8172.
[12] D. Farrusseng, Metal-organic Frameworks: Applications from Catalysis to Gas Storage, first ed., Wiley-VCH, Weinheim, 2011.
[13] H. Li, K. Wang, Y. Sun, C.T. Lollar, J. Li, H.C. Zhou, Recent advances in gas storage and separation using metal-organic frameworks, Mater. Today 2 (2018) 108–121.
[14] M.X. Wu, Y.W. Yang, Metal-organic framework (MOF)-based drug/cargo delivery and cancer therapy, Adv. Mater. 29 (2017) 1606134.
[15] W. Cai, J. Wang, C. Chu, W. Chen, C. Wu, G. Liu, Metal-organic framework-based stimuli-responsive systems for drug delivery, Adv. Sci. 6 (2019) 1801526.
[16] I. Strauss, A. Mundstock, M. Treger, K. Lange, S. Hwang, C. Chmelik, P. Rusch, N. C. Bigall, T. Pichler, H. Shiozawa, J. Caro, Metal-organic framework Co-MOF-74-based host-guest composites for resistive gas sensing, Appl. Mater. Interfaces 11 (2019) 14175–14181.
[17] M.E. DMello, N.G. Sundaram, A. Singh, A.K. Singh, S.B. Kalindindi, An amine functionalized zirconium metal-organic framework as an effective chemiresistive sensor for acidic gases, Chem. Commun. 55 (2019) 349–352.
[18] K. Vikrant, V. Kumar, Y.S. Ok, K.H. Kim, A. Deep, Metal-organic framework (MOF)-based advanced sensing platforms for the detection of hydrogen sulfide, Trends Anal. Chem. 105 (2018) 263–281.
[19] V. Chernikova, O. Yassine, O. Shekhah, M. Eddaoudi, K.N. Salama, Highly sensitive and selective SO_2 MOF sensor: the integration of MFM-300 MOF as a sensitive layer on a capacitive interdigitated electrode, J. Mater. Chem. A 6 (2018) 5550–5554.
[20] V. Pentyala, P. Davydovskaya, R. Pohle, G. Urban, O. Yurchenko, Mg-MOF74 and Co-MOF74 as sensing layers for CO_2 detection, Procedia Eng. 87 (2014) 1071–1074.
[21] J.J. Gassensmith, J.Y. Kim, J.M. Holcroft, O.K. Farha, J.F. Stoddart, J.T. Hupp, N. C. Jeong, A metal-organic framework-based material for electrochemical sensing of carbon dioxide, J. Am. Chem. Soc. 136 (2014) 8277–8282.
[22] S. Couck, J.F.M. Denayer, G.V. Baron, T. Rémy, J. Gascon, F. Kapteijn, An amine-functionalized MIL-53 metal-organic framework with large separation power for CO_2 and CH_4, J. Am. Chem. Soc. 131 (2009) 6326–6327.
[23] K. Chakarova, I. Strauss, M. Mihaylov, N. Drenchev, K. Hadjiivanov, Evolution of acid and basic sites in UiO-66 and UiO-66-NH_2 metal-organic frameworks: FTIR study by probe molecules, Microporous Mesoporous Mater. 281 (2019) 110–122.
[24] M. Campbell, M. Dincă, Metal-organic frameworks as active materials in electronic sensor devices, Sensors 17 (2017) 1108.
[25] V.R. Bakuru, S.R. Churipard, S.P. Maradur, S.B. Kalidindi, Exploring the Brønsted acidity of UiO-66 (Zr, Ce, Hf) metal-organic frameworks for efficient solketal synthesis from glycerol acetalization, Dalton Trans. 48 (2019) 843–847.
[26] L. Valenzano, B. Civalleri, S. Chavan, S. Bordiga, M.H. Nilsen, S. Jakobsen, K. P. Lillerud, C. Lamberti, Chem. Mater. 23 (2011) 1700–1718.
[27] J.H. Cavka, S. Jakobsen, U. Olsbye, N. Guillou, C. Lamberti, S. Bordiga, K. P. Lillerud, A new zirconium inorganic building brick forming metal organic frameworks with exceptional stability, J. Am. Chem. Soc. 130 (2008) 13850–13851.
[28] J.B. Decoste, G.W. Peterson, H. Jasuja, T.G. Glover, Y.G. Huang, K.S. Walton, Stability and degradation mechanisms of metal-organic frameworks containing the $Zr_6O_4(OH)_4$ secondary building unit, J. Mater. Chem. A 1 (2013) 5642–5650.
[29] G.C. Shearer, S. Chavan, J. Ethiraj, J.G. Vitillo, S. Svelle, U. Olsbye, C. Lamberti, S. Bordiga, K.P. Lillerud, Tuned to perfection: ironing out the defects in metal-organic framework UiO-66, Chem. Mater. 26 (2014) 4068–4071.
[30] D.B. Dwyer, D.T. Lee, S. Boyer, W.E. Bernier, G.N. Parsons, W.E. Jones Jr., Toxic organophosphate hydrolysis using nanofiber-templated UiO-66-NH_2 metal-organic framework polycrystalline cylinders, ACS Appl. Mater. Interfaces 10 (2018) 25794–25803.
[31] J. Ethiraj, E. Albanese, B. Civalleri, J.G. Vitillo, F. Bonino, S. Chavan, G.C. Shearer, K.P. Lillerud, S. Bordiga, Carbon dioxide adsorption in amine-functionalized mixed-ligand metal-organic frameworks of UiO-66 topology, ChemSusChem 7 (2014) 3382–3388.
[32] M.R. Ryder, L. Donà, J.G. Vitillo, B. Civalleri, Understanding and controlling the dielectric response of metal-organic frameworks, ChemPlusChem 83 (2018) 308–316.
[33] F. Kremer, A. Schönhals, Broadband Dielectric Spectroscopy, Springer-Verlag, 2003, pp. 87–91.
[34] X. Xia, Z. Zhong, G.J. Weng, Maxwell-Wagner-Sillars mechanism in the frequency dependence of electrical conductivity and dielectric permittivity of graphene-polymer nanocomposites, Mech. Mater. 109 (2017) 42–50.
[35] H. Lu, X. Zhang, H. Zhang, Influence of the relacation of Maxwel-Wagner-Sillars polarization and dc conductivity on the dielectric behaviors of nylon 1010, J. Appl. Phys. 100 (2006) 054104.
[36] H. Molavi, A. Eskandari, A. Shojaei, S.A. Mousavi, Enhancing CO_2/N_2 adsorption selectivity via post-synthetic modification of NH_2-UiO-66(Zr), Microporous Mesoporous Mater. 257 (2018) 193–201.
[37] G.E. Cmarik, M. Kim, S.M. Cohen, K.S. Walton, Tuning the adsorption properties of UiO-66 via ligand functionalization, Langmuir 28 (2012) 15606–15613.

7

8 Conclusion

8.1 Summary

The aim of this thesis was the synthesis, modification and evaluation of promising MOFs and the initial attempt of their subsequent incorporation into sensors for the detection of various hazardous gas species. Therefore, three main tasks were accomplished within the duration of this thesis. In a first step, the search of MOF materials which are suitable for the incorporation into gas sensing devices was achieved. This task was followed up by fundamental studies of the adsorption properties of the materials in order to gain a deeper understanding of the particular MOFs. In a last step, suitable concepts to perform resistive gas sensing investigations utilizing the most promising MOFs were realized.

The two materials presented within this thesis, UiO-66 and MOF-74, were considered to be appropriate candidates for the previously described task of developing MOF-based sensors. The three dimensional Co-MOF-74, with its honeycomb topology and large, one-dimensional channels with a diameter of 11 Å, seems to be a suitable framework due to its open metal sites which are oriented into the channels and are therefore easily accessible for guest molecules such as various gas species. By means of a general Vis/NIR and Raman study concerning the interaction between guest molecules and Co-MOF-74, it could be proved that the positions of the characteristic absorbance maxima in Vis/NIR spectra, as well as the positions of the characteristic stretching modes are strongly dependent on the surrounding atmosphere and its interaction with the framework. Carbon dioxide, propene, propane, methanol and water were used as guest molecules and compared to the Co-MOF-74 under argon atmosphere. Each species influences the characteristic spectra of the MOF due to specific interactions with the open metal sites and could thereby be distinguished from each other. Especially striking is the sensors ability to distinguish between the very similar gases propene and propane. In the presence of propene π-backbonding occurs, while in the presence of propane no functionalities can interact with the MOF and therefore the interaction is at best low. Besides the examination of Co-MOF-74 regarding a potential incorporation into chemical sensing devices, general spectral investigations brought to light an anisotropic adsorption behaviour of the material when illuminated with polarized light, which might be advantageous within optical applications, such as display technology or optical imaging where the control of the polarization matters.

These investigations were followed up by the synthesis of a conducting Co-MOF-74 composite material and the development of a MOF-based capacitive gas sensor. Since Vis/NIR and Raman investigations verified the potential of Co-MOF-74 concerning gas sensing applications, the following task was to create an electrical conductive material,

which changes its current depending on the surrounding atmosphere. While the successful infiltration of Co-MOF-74 with the organic semiconductor TTF was proved by various methods such as TGA, XPS, IR and Raman spectroscopy, its resistive gas sensing properties were tested via electrical measurements. Although the uptake of gaseous guest species was reduced due to the infiltration to TTF into the pores, it was possible to distinguish various gas atmospheres such as CO_2, CH_4, N_2 and air.

The second investigated framework-type, UiO-66, was chosen due the fact that its amino-functionalized derivate UiO-66-NH_2 is known to undergo strong adsorptive interactions with CO_2. In addition to that, these zirconium-based MOFs are known to possess an extremely high chemical and thermal stability compared to other MOFs. Here again, general investigations on the adsorption behaviour of the UiO-66 and UiO-66-NH_2 MOFs were performed by using the probe molecules carbon monoxide, nitrogen and acetonitrile in order to study the evolution of the acid and basic sites of the frameworks via FTIR measurements. With the enhanced understanding regarding the acidic and basic properties, the materials were examined regarding their incorporation into gas sensing devices. For that aim, carbon dioxide dependent FTIR measurements were performed, indicating a superior sensing capability of UiO-66-NH_2 over UiO-66 at low gas concentrations. FTIR investigations also revealed that the co-existence of water molecules during measurements featuring a low CO_2 concentration further enhances the sensing performance. The amount of adsorbed CO_2 correlates with the intensity of the μ_3-OH band in the FTIR spectra, indicating hydroxyl groups as active sites for CO_2 adsorption.

In addition to that, dielectric investigations with high CO_2 concentrations were performed, which confirmed the FTIR results and substantiate UiO-66-NH_2 to be a suitable material to be incorporated into future MOF-based sensors. Here, the adsorption of CO_2 causes a significant decrease of the capacity at low frequencies, which is based on occurring Maxwell-Wagner-Sillars polarization and can easily be taken advantage of for sensing.

8.2 Discussion and outlook

Within this thesis, two promising MOFs have been tested due to their possible incorporation into applications in the field of sensors. On the one hand, two studies concerning Co-MOF-74 were presented, showing selective changes when various guest molecules are used as surrounding atmospheres. Unfortunately, some difficulties need to be overcome for a successful implementation of Co-MOF-74 and the TTF-MOF-74 composite into industrial applications. First of all, Co-MOF-74 and its functionality is very vulnerable against water, since it occupies the open metal sites within the pores. Therefore, all detection processes need to be performed in water-free environments or otherwise include demanding

regeneration steps. Remedies like the infiltration of TTF result in a smaller amount of water diffusing into the pores, but still, this problem needs to be addressed. Secondly, further research should survey the sensitivity of Co-MOF-74 and the TTF-MOF-74 composite regarding lower concentrations of the applied gases. In case of still high sensitivities towards different gases, there might be a great potential for this MOF-class because the ability to distinguish between very similar gases like propene and propane makes this a promising platform for future sensor materials.

On the other hand, the presented UiO-66 and UiO-66-NH$_2$ studies show that the latter MOF could also be a promising material for sensor devices. The main advantage of UiO-66-NH$_2$ over Co-MOF-74 is its high stability, even in humid air. Via CO_2 and water co-adsorption studies we could even evidence an improvement of the sensitivity due to the interaction between the adsorbed CO_2 and hydroxyl groups, which are built into UiO-66-NH$_2$ in the presence of water. Nevertheless, also here some challenges need to be overcome for the incorporation into sensors: Further research should examine the cross-sensitivity, provided that they should be used beyond the CO_2/N_2 system, which is for example used for industrial food packaging. Also alternative detection methods should be taken into account, since the used FTIR construction used within the UiO-66 studies is too complex and unwieldy to be realized as a sensor, the principle behind the dielectric studies is rather complicated and the best sensitivity towards CO_2 is only achieved at extremely low frequencies.

In conclusion, two MOFs were presented, which show promising results within the chosen model systems under the used conditions. Beyond that, these MOFs probably need to be further improved to be useful for the incorporation into chemical sensor devices. Further research on this topic should be executed to ensure that these materials are advantageous over other MOFs or other sensor materials when introduced into industrial applications.

Also currently used (non-MOF-) sensors often lack sensitivity, selectivity or stability. Already implemented materials, like metal oxides, indeed possess higher responses (in resistance) compared to others, but show handicaps like low selectivity and often require high operating temperatures up to 500 °C. Even though, carbon-based materials operate at room temperature, their drawbacks, such as low response, selectivity and reproducibility, are numerous.

Theoretically, MOFs should be advantageous over the named examples, since the response of a sensor is dependent on its surface reaction or adsorption of the analytes and MOFs possess both, large surface areas and high reactivities. Moreover, they should show a superior selectivity due to their structural tuneability leading to unique surface reactions in the presence of specific analytes. In practice, MOFs and MOF-based/derived composites

often suffer from similar disadvantages as common sensors: Low sensitivity, low selectivity, low reproducibility, low response and poor stability. Nevertheless, among the tens of thousands of MOFs, there are candidates, which are able to compete with present sensors.[159] Looking at recent hot topics like acetone or NO_x sensing, suitable MOFs are not only theoretically superior to common materials, but also in practice.[159] In order to sense the acetone concentration in the breath of diabetes patients, the sensors need to possess a sensitivity in the range of parts per billion.[171] Recent MOF-involving studies were able to reach this value with low cross-sensitivities (e.g. for ethanol) at temperatures below 400 °C. [159,172] Also regarding NO_x sensing, existing studies confirm a superior behaviour of MOFs over present materials. Conventional NO_x sensors, for example, operate at high temperatures and are difficult to produce, while MOFs (e.g. $Me_3(HHTP)_3$, Me=Cu, Co, Fe) are able to operate at room temperature. [159,173]

Unfortunately examples for outstanding sensor concepts which include MOFs as integral parts are hard to find. In the majority of cases, expensive MOFs are used as templates in order to create isolated active metal-sites. This approach might lead to sensors with a slightly enhanced sensitivity, but with a much higher price tag.

In my view, the focus should return to use the MOFs itself rather than calcination products. In order for that to work, a general rethinking of the MOF community needs to take place, since these frameworks are studied for over two decades and only a handful industrial applications were realized until now. After decades of fundamental research, the focus should be set more on the implementation of the existing MOFs into industrial devices than on additional fundamental research studies. In addition to that, the laboratory production costs of MOFs need to be significantly reduced to reach an industrially relevant scale. Therefore, researchers need to team up with industrial companies to develop and evaluate cheap, scalable MOFs via green synthesis methods, since their successful implementation into real world applications strongly depends on financial profit.

9 Appendix

9.1 List of publications

Articles

2020   **UiO-66 and UiO-66-NH$_2$ based sensors: Dielectric and FTIR investigations on the effect of CO$_2$ adsorption**. I.Strauss, K. Chakarova, A. Mundstock, M. Mihaylov, K. Hadjiivanov, N. Guschanski, J. Caro, Microporous Mesoporous Mat., 2020, 302, 110227.

2020   ***In situ* FTIR Spectroscopy as a Tool for Investigation of Gas/Solid Interaction: Water-Enhanced CO$_2$ Adsorption in UiO-66 Metal-Organic Framework**. N.L. Drenchev, K.K. Chakarova, O.V. Lagunov, M.Y. Mihaylov, E.Z. Ivanova, I. Strauss, K. Hadjiivanov, J. Vis. Exp., 2020, 156.

2019   **Metal-Organic Framework Co-MOF-74 Based Host-Guest Composites for Resistive Gas Sensing**. I. Strauss, A. Mundstock, M. Treger, K. Lange, S. Hwang, C. Chmelik, P. Rusch, N. C. Bigall, T. Pichler, H. Shiozawa, J. Caro, ACS Appl. Mater. Interfaces, 2019, 11 (15), 14175-14181.

2019   **Evolution of acid and basic sites in UiO-66 and UiO-66-NH$_2$ metal-organic frameworks: FTIR study by probe molecules.** K. Chakarova, I.Strauss, M. Mihaylov, N. Drenchev, K. Hadjiivanov, Microporous Mesoporous Mat., 2019, 281, 110-122.

2019   **Impact of border traps in ultrathin metal-organic frameworks Cu$_3$(BTC)$_2$ based capacitors.** L. M. Montanez, I. Strauß, J. Caro, H. J. Osten, Microporous Mesoporous Mat. 2019, 277, 136-141.

2018   **Polymer-Stabilized Percolation Membranes Based on Nanosized Zeolitic Imidazolate Frameworks for H$_2$/CO$_2$ Separation.** J. Sánchez-Laínez, S. Friebe, B. Zornoza, A. Mundstock, I. Strauß, C. Téllez, J. Caro, J. Coronas, ChemNanoMat 2018, 4, 698-703.

2018   **Vis/NIR- und Raman-Untersuchung der Wechselwirkung von Gastmolekülen und Co-MOF-74.** I. Strauss, A. Mundstock,

D. Hinrichs, R. Himstedt, A. Knebel, C. Reinhardt, D. Dorfs, J. Caro, Angew. Chem. 2018, 130, 7556-7561.

2018   **Frontispiz: Vis/NIR- und Raman-Untersuchung der Wechselwirkung von Gastmolekülen und Co-MOF-74.** <u>I. Strauss</u>, A. Mundstock, D. Hinrichs, R. Himstedt, A. Knebel, C. Reinhardt, D. Dorfs, J. Caro, Angew. Chem. 2018, 130, 7556.

2018   **The Interaction of Guest Molecules with Co-MOF-74: A Vis/NIR and Raman Approach.** <u>I. Strauss</u>, A. Mundstock, D. Hinrichs, R. Himstedt, A. Knebel, C. Reinhardt, D. Dorfs, J. Caro, Angew. Chem. Int. Ed. 2018, 57, 7434-7439.

2018   **Frontispiece: The Interaction of Guest Molecules with Co-MOF-74: A Vis/NIR and Raman Approach.** <u>I. Strauss</u>, A. Mundstock, D. Hinrichs, R. Himstedt, A. Knebel, C. Reinhardt, D. Dorfs, J. Caro, Angew. Chem. Int. Ed., 57, 7434.

2018   **Hierarchical Nanostructures of Metal-Organic Frameworks Applied in Gas Separating ZIF-8-on-ZIF-67 Membranes.** A. Knebel, P. Wulfert-Holzmann, S. Friebe, J. Pavel, <u>I. Strauß</u>, A Mundstock, F. Steinbach, J. Caro, Chem. Eur. J. 2018, 24, 5728-5733.

2018   **Cover Feature: Hierarchical Nanostructures of Metal-Organic Frameworks Applied in Gas Separating ZIF-8-on-ZIF-67 Membranes.** A. Knebel, P. Wulfert-Holzmann, S. Friebe, J. Pavel, <u>I. Strauß</u>, A Mundstock, F. Steinbach, J. Caro, Chem. Eur. J. 2018, 24, 5728.

2017   **Azobenzene Guest Molecules as Light-Switchable CO_2 Valves in an Ultrathin UiO-67 Membrane.** A. Knebel, L. Sundermann, A. Mohmeyer, <u>I. Strauß</u>, S. Friebe, P. Behrens, J. Caro, Chemistry of Materials 2017, 29 (7), 3111-3117.

Poster

2019   **Tetrathiafulvalene Doped Cobalt containing Metal-Organic Framework for Resistive Gas Sensing.** <u>I. Strauss</u>, A. Mundstock, H. Shiozawa, M. Treger, K. Lange, S. Hwang, C. Chmelik, P. Rusch, N. Bigall, T. Pichler, J. Caro, EuroMOFParis 2019, Maison de la chimie.

2019   **Tetrathiafulvalene Doped Cobalt containing Metal-Organic Framework for Gas Detection Applications.** <u>I. Strauss</u>,

A. Mundstock, H. Shiozawac, M. Treger, K. Lange, S. Hwang, C. Chmelik, P. Rusch, N. Bigall, T. Pichler, J. Caro, DZT 2019, TU Dresden.

2018   **On the interaction of guest molecules with Co-MOF-74.** I. Strauß, A. Mundstock, D. Hinrichs, R. Himstedt, A. Knebel, C. Reinhardt, D. Dorfs, J. Caro, Bunsentagung 2018, Leibniz Universität Hannover.

2017   **Investigations of guest interaction with Co-MOF-74.** I. Strauß, A. Mundstock, D. Hinrichs, R. Himstedt, A. Knebel, C. Reinhardt, D. Dorfs, J. Caro, EuroMOF2017, TU Delft.

9.2 Curriculum vitae

Ina Carina Strauß

Date of birth   16.02.1992

Place of birth   Gelsenkirchen

Nationality   German

Education

2016-2020	Dissertation at the Institute of Physical Chemistry and Electrochemistry, Leibniz University Hannover in the group of Prof. Dr. Jürgen Caro.
	Title: "Metal-organic frameworks for gas- and vapour-sensing applications".
2014-2016	Master of Science at the Institute of Physical Chemistry and Electrochemistry, Leibniz University Hannover in the group of Prof. Dr. Armin Feldhoff.
	Title: "Ruddlesden-Popper type oxygen-transporting membranes with cationic substoichiometry".
2011-2014	Bachelor of Science at the Institute of Inorganic Chemistry, Ruhr University Bochum in the group of Prof. Dr. Anja-Verena Mudring.
	Title: "Synthesis of antimony telluride nanoparticles in ionic liquids".
2011	Abitur at the Max-Planck Gymnasium Gelsenkirchen-Buer, with advanced courses in mathematics and chemistry.